DESIGN, CONSTRUCTION, AND VALIDATION OF

A PLANAR BIAXIAL DEVICE FOR

MECHANICAL TESTING OF SOFT TISSUES

AN ABSTRACT

SUBMITTED ON THE FIFTEENTH DAY OF APRIL 2017

TO THE DEPARTMENT OF BIOMEDICAL ENGINEERING

IN PARTIAL FULFILLMENT OF THE REQUIREMENTS

OF THE SCHOOL OF SCIENCE AND ENGINEERING

OF TULANE UNIVERSITY

FOR THE DEGREES

OF

MASTER OF SCIENCE AND BACHELOR OF SCIENCE IN ENGINEERING

BY

Jonathan Nguyen

APPROVED:

Kristin S. Miller, Ph.D.
Director

Ronald C. Anderson, Ph.D.

Katherine K. Raymond, Ph.D.

ABSTRACT

Soft tissue mechanics attempts to describe biological tissues such as skin, tendon, and the reproductive organs using concepts found in mechanical engineering. By approaching soft tissues using this framework, the complex biomechanical response of such tissues, which have been implicated in the development of disease and injury, can be ascertained and quantified. Robust mechanical tests, in which tissue stress-strain behavior is characterized, are needed in order to inform constitutive models of healthy and diseased tissue. The overall objective of this thesis was to design, construct, program, and validate a planar biaxial device capable of testing soft tissues. Improvements and redesigns were made to the device to better suit the nature of testing required for soft tissue. Custom grips, modules, and software were developed and fabricated to facilitate accurate biaxial mechanical tests. Optimized for testing of small soft tissues, the biaxial device is an evolution of the standard approach towards mechanical testing. The overall device and the individual systems were validated internally and externally. Pilot studies were conducted on murine skin, compared to existing data from literature, and observed to correspond with known stress-strain and load-displacement properties. Further, experimental protocols were developed to evaluate the biaxial behavior of soft tissues, including cervical, uterine, vaginal, and uterosacral ligament tissue. Studies were described in which experimental data could be used to establish structure-function relationships describing reproductive tissue. Results from these studies could be used to elucidate the underlying mechanical etiologies of preterm birth and pelvic organ prolapse.

DESIGN, CONSTRUCTION, AND VALIDATION OF

A PLANAR BIAXIAL DEVICE FOR

MECHANICAL TESTING OF SOFT TISSUES

A THESIS

SUBMITTED ON THE FIFTEENTH DAY OF APRIL 2017

TO THE DEPARTMENT OF BIOMEDICAL ENGINEERING

IN PARTIAL FULFILLMENT OF THE REQUIREMENTS

OF THE SCHOOL OF SCIENCE AND ENGINEERING

OF TULANE UNIVERSITY

FOR THE DEGREES

OF

MASTER OF SCIENCE AND BACHELOR OF SCIENCE IN ENGINEERING

BY

Jonathan Nguyen

APPROVED:

Kristin S. Miller, Ph.D.
Director

Ronald C. Anderson, Ph.D.

Katherine Raymond, Ph.D.

Acknowledgements

It seems like the acknowledgements section might be the only place that academic researchers are able to reveal that they, in fact, do have hearts—hearts that are eternally grateful to everyone who has helped them get to where they are today. I am no exception, so I am going to take a few lines to thank a most auspicious group of people. First, I would like to thank Dr. Kristin Miller for being a seemingly infinite source of biomedical knowledge. A lab could not be complete without its graduate and undergraduate researchers, however. I have to look no further than the chair to my left to see Taylor McCrady and know I could not have asked for a better friend and lab partner for the biaxial device and beyond. Her Herculean efforts have made the biaxial device feasible, not just for us but for future researchers in the lab. To Cody O'Cain, I am grateful for his vast knowledge of all things related to making things. I also thank Ben O'Donnel, in his brief time in the G&R lab, offered countless thoughtful insights. I am additionally thankful for the sagacity and meticulous record keeping of Jason Schuster and the puns and advice of Cassie Conway. I extend thanks to David Simon, whose designs are the foundation of our biaxial device.

On the non-lab side, I must of course thank my parents, Oanh and Hon Nguyen, who have supported my craziness since forever. It's a good thing they encouraged me to go into biomedical engineering, and it's a good thing they told me to work hard and do my best.

I must also thank the Newcomb-Tulane Dean's Grant program for providing additional funding for the biaxial device and lab work and the Oschner Translation Medicine Research Initiative (OTMRI), with which our lab is a collaborator.

Lastly, I would like to thank the other members of my thesis committee, Dr. Ronald Anderson and Dr. Katherine Raymond, for their help and valuable time.

Table of Contents

List of Tables

List of Figures

Chapter 1. Introduction

A. INTRODUCTION

Biomechanics, as defined by Y.C. Fung in his book *Biomechanics: Mechanical Properties of Living Tissues,* is defined as the application of mechanics, a traditional field of engineering, to biology (Fung, 1993). J.D. Humphrey expands this definition: biomechanics includes, in addition to its application, the development and extension of mechanics to better understand the pathology and treatment of injuries or diseases (Humphrey, 2003). By extending the principles of continuum mechanics (i.e. stress and strain) to biological components like cells, mechanobiological interactions can be determined and quantified. How cells respond can be understood through the lens of growth and remodeling. The central hypothesis of this field, that cells seek to establish, maintain, and restore a preferred homeostatic state of stress, is reliant upon mechanical principles (Humphrey and Rajagopal, 2002). In response to a mechanical stimulus, cells can change phenotypes or change the composition of their extracellular surroundings to achieve a preferred stress state in a phenomenon known as remodeling. Remodeling can restore homeostasis, or, in the case of maladaptive remodeling, lead to a failure of the biological system to perform as required.

Understanding what leads to successful or maladaptive remodeling is therefore of paramount importance. Successful remodeling can be understood as the restoration of a preferred stress state within biological tissue. Maladaptive remodeling can be understood as failure to restore from or even an acceleration towards a detrimental mechanical

environment. It is then necessary to understand how the individual constituents within the extracellular matrix determine the mechanical environment and response of the cell. During growth or remodeling, these constituents could be augmented, diminished, or reoriented in relation to each other. This in turn can drastically alter the mechanical response of the tissue. By relating individual biological components to overall tissue-level mechanical stress and strain, structure-function relationships that quantitatively describe remodeling within tissue can be identified.

It follows that, to deduce these structure-function relationships, tissue mechanical behavior must be measured and modeled alongside the properties, geometry, and contributions of the individual extracellular constituents, which act as structural, load-bearing components (Sacks, 2000). To this end, mechanical testing can be used to measure tissue response to mechanical loads. Mechanical testing, which creates stress-strain curves, was not traditionally applied to biomedical engineering. These methods were most often used to test the mechanical properties, such as stiffness and yield stress, of inorganic materials (i.e. metals, rubbers, and artificial polymers). The testing of biological tissue produces results that are often substantially more complex than synthetic materials, with tissues exhibiting nonlinear, anisotropic, pseudoelastic behavior (Fung, 1993).

In addition to experimental mechanical testing methods, mathematical approaches have also been employed. In fact, the end goal of mechanical testing is to create constitutive models that are able to describe existing data and even predict tissue mechanical behavior as a function of its constituents. Due to the complex behavior of biological tissue, these models are complicated and often computationally intensive. The most biologically relevant but also complex of these models attempt to correlate stress with strain by means

of several material parameters that describe constituents' mechanical properties, structure, and presence. The main advantage of a constitutive model for any tissue, however, lies with its predictive power. With such a model, clinically relevant changes in tissue can be directly derived from changes in material parameters within the model. Utilizing mathematical models to observe (patho)physiological changes in tissue properties is significantly more efficient than systematically analyzing tissue samples via experimental methods. With a sufficiently complete computational model, which requires rigorous experimentation and data input from many mechanical tests, a new paradigm for clinical treatment of tissue could be incorporated. Such a paradigm could include highly customized treatments based on a patient's specific tissue properties.

B. BACKGROUND

B1. MECHANICAL TESTING

Mechanical testing of tissue involves cutting a sample of the tissue of interest, often into an optimal shape to minimize boundary artifacts intrinsic to mechanical testing, gripping the sample, and then pulling it in tension and returning to reference in a prescribed protocol. Force due to testing is measured, and strain within the tissue is recorded through non-contact optical tracking. Mechanical testing can be broken into two main types: uniaxial and biaxial testing. Uniaxial testing is the simpler of the two, involving only one test axis. The data that comes from a uniaxial test can be valuable and is often a good starting point for testing tissues that have not yet been rigorously defined biomechanically. It cannot, however, be used to fully quantify the constitutive equations for many soft tissues which have anisotropic properties. To this end biaxial testing, which has two testing axes, allows for the formation of more complex, physiologically relevant model and loading conditions that consider tissue anisotropy (Sacks 2000). Tissue in the body is rarely loaded

in one direction and often experiences stresses along multiple axes; biaxial mechanical testing devices could thus better simulate the stress state of tissue *in vivo* and provide more physiologically relevant data. Additionally, uniaxial tests could artificially inflate stiffness by allowing constituent fibers to realign in the single direction of loading since the test constrains tissue in only one direction (Mauri, 2013; Cooney, 2016). Lanir and Fung were the first to utilize biaxial testing for soft tissue (Lanir and Fung, 1974); biaxial testing has since been used to quantify many tissues, including tendons (Szczesny, 2012), vasculature (Bell, 2013; Sommer, 2010), pericardium (Waldman and Lee, 2002), ureter (Rassoli, 2014), and skin (Muñoz, 2008). Despite the undeniable usefulness of biaxial testing, experiments must be carefully conducted and tend to be more complex than uniaxial tests. Of great importance is the design and interpretation of boundary conditions on a biaxially loaded specimen that is constrained in two directions. As will be discussed in later chapters, an accurate biaxial test and analysis requires a multifactorial approach that accounts for grips, specimen shape and size, specimen behavior, and deformation tracking.

Biaxial tests can run in either tension- or strain-controlled modes. Strain-controlled protocols run tests based on feedback from tissue deformation and allow the incorporation of in-plane shear to the study, but limits the possible loading configurations compared to stress-controlled protocols (Sun, 2003). Two main loading protocols can be used to mechanically test tissue: equibiaxial testing or constant-force or -stretch tests. Equibiaxial testing maintains both loading axes at

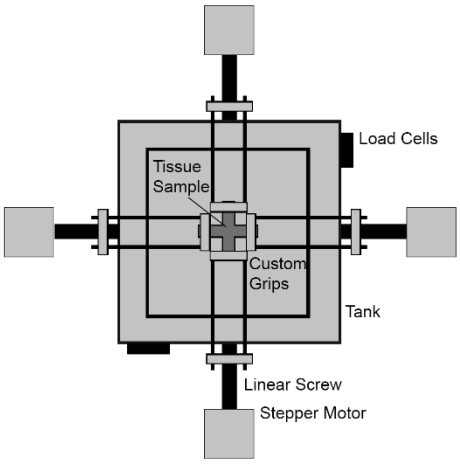

Figure 1: Overhead illustration of planar biaxial device

equal strains or stresses during cyclic loading; constant-force or constant-stretch tests keeps one axis constant while another axis is stretched (Humphrey, 1987; Bai, 2014). The latter test can also be modified to keep tissue stretch at a prescribed ratio (Lanir and Fung, 1974).

B2. MICROSTRUCTURAL CONSTITUENTS OF SOFT TISSUE

The three main load-bearing constituents which form the majority of the passive mechanical response of tissue are collagen, elastin, and glycosaminoglycans (GAGs) (Humphrey, 2014). Collagen is the primary load-bearing constituent, which is, for instance, responsible for the high tensile strength and stiffness of tendon. Elastin provides a spring-like component tissue, allowing tissue to be both highly distensible and elastic. GAGs are negatively charged molecules often found bound to protein cores in high molecular weight complexes called proteoglycans. Their polar nature attracts water molecules into a "gel" that allows cartilaginous tissue to absorb compressive shock and recover. These constituents are secreted by cells, notably fibroblasts, into the extracellular matrix (ECM), which provides structure, stability, and support to cells.

The collective effect of the collagen and elastic fibers, their orientations, and their organization gives tissues anisotropic, highly nonlinear, heterogeneous behavior. This leads to the need for complex constitutive relations to describe them. Changes to collagen and elastin in the microstructure of a tissue, due to age, trauma, disease, stress profile, or remodeling, often lead to dramatic changes in the mechanical properties of that tissue. Previous studies have shown that ECM constituents undergo continuous turnover and remodeling. Collagen and elastin appear to be deposited and aligned in relation to loading direction, subsequently changing cell mechanical environment (Sander, 2011). Regarding age, elastic fibers are present and organized in the body in a relatively fixed amount before maturity and thus can only decrease in number with age. Thus, damage to these fibers could

cause irreversible changes at the tissue level (Humphrey, 2014). Due to early presence, elastic fibers contribute to pre-stress, known as residual stress for arteries, that can be observed through opening angle experiments. The residual stress and opening angle can vary with location, tissue size, and remodeling (Fung, 1993). Computational models based on mechanical tests on abdominal aortic arteries have shown that with increasing age, the contribution from elastic fibers becomes superseded by collagen fibers, leading to stiffer, more anisotropic arterial tissue with a diminished toe region in the stress-strain curve (Ferruzzi, 2011). Diseases such as hypertension could also affect the ratio of elastic fibers to collagen fibers, leading to similar stiffening behavior (Eberth, 2011). Collagen itself is subject to degradation by enzymes called metalloproteases, with evidence showing that physical strain could preferentially preserve collagen oriented along the strained axis (Flynn, 2010).

Collagen exhibits well-known crimping behavior when unloaded. Microscopy has revealed that collagen fibers in tendons are organized in coplanar waves oriented along the axis of loading and, upon stress application, straighten out in a reversible manner (Nicholls, 1983). Age can also affect collagen crimping, with increasing age decreasing the angle of crimping and thus the overall amount

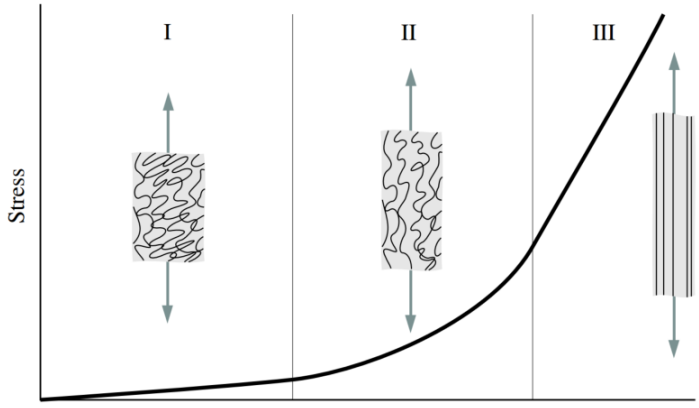

Figure 2: Representative stress-strain diagram for collagen. Region I is the low-strain toe region in which fibers are crimped. Fibers transition through region II to become fully engaged in region III, increasing stiffness at higher strains. (Holzapfel, 2000)

of elastic deformation before plastic deformations occurs (Legerlotz, 2014). Crimping can be observed in mechanical stress-strain graphs by the presence of three different regions. The toe region demonstrates a curve of relatively high compliance in which the collagen fibrils are straightening followed by increasing stiffness to a linear region in which most of the fibrils have straightened. During mechanical testing of tissues, it is necessary to precondition the tissue by repeated cyclic loading and unloading. During this period tissue structure changes until it converges to a stable behavior appropriate for the designated testing conditions (Fung, 1993).

Multiple subtypes of collagen exist, but the two main subtypes are fiber forming: collagen type I and collagen type III. Type I collagen forms fiber networks of thick bundles while collagen type III forms thinner fiber networks. Both of these collagen types are present in most soft tissues and together modulate the fibrous network formed (Lapiere, 1976). The base unit of collagen is a triple helix of α protein chains that form fibrils. Fibrils are in turn composed of staggered collagen molecules covalently bonded by lysyl oxidase-induced crosslinking, which are further grouped together to form fibers, forming a self-assembling hierarchical structure (Hulmes, 2008). When under load, fibrils show lower local strain than the overall tissue strain, signifying that cross-link slippage and realignment may be significant contributors to collagen stress-strain behavior (Screen, 2003). The extent and type of crosslinking between collagen molecules appears to determine collagen mechanical

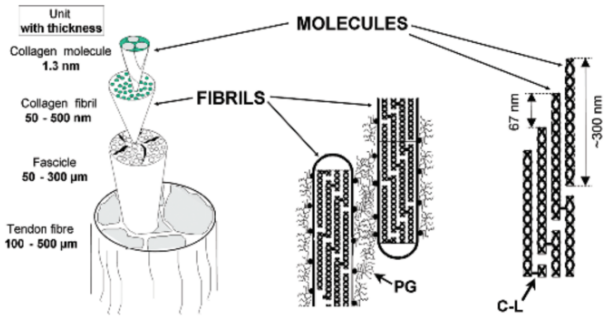

Figure 3: Hierarchical organization of collagen from macromolecule to fibril to whole tissue (Fratzl, 2008)

behavior under load at an elementary level; the arrangement of collagen fibers further modulates mechanical properties (Avery and Bailey, 2008). Hence tissues can exhibit drastically different mechanical properties despite similar constituents. Skin and tendon, for example, have significantly different levels of compliance and stiffness due to structural differences in their respective oriented collagen networks.

Tissues can be arranged in complexity of structure, ranging from the simplest, tendon, to skin, and finally to the most complex, blood vessels and the female reproductive tract. In the female reproductive system, smooth muscle composes 30-40% of the uterus and 10% of the cervix in addition to structural fibers; changes in the ratio of ground substance to structural fibers has been linked to changes observed during pregnancy, further complicating quantification of such tissue (Fung, 1993).

B3. CONSTITUTIVE MODELING

In order to determine the underlying factors of tissue mechanical behavior, constitutive relations must be informed by mechanical tests conducted over a range of physiological values. Ideally, changes to material parameters in these constitutive equations would reflect mechanobiological changes within tissue, allowing the equations to predict mechanical behavior and the contributions of different components of the tissue. The goodness of fit to experimental data determines the validity of the model and its applicability to that particular set of conditions or constraints; the complex environment and behavior of tissue precludes the ability of any single one model to determine multiscale tissue behavior. Constitutive equations, however, remain among the most versatile and informative methods of biomechanically quantifying a wide variety of tissues. Many biomechanical studies of soft tissues incorporate constitutive modeling to better describe results from mechanical tests in terms of material parameters such as elastic modulus and

fiber orientation. These models have been included with experiments on the ureter (Sokolis, 2017), thoracic ducts (Caulk, 2015), annulus fibrosis (O'Connell, 2009; Bass, 2004), carotid arteries (Eberth, 2011), and linea alba (Cooney, 2015; Cooney 2016), among a multitude of other studies. Descriptions of material properties can further be incorporated into finite element models of tissue that allow simulation of tissue behavior under different loading conditions and deformations. Results from these theoretical analyses can then be used as feedback to design better physical experiments that optimize variables such as clamping pressure, sample size and shape, and region of interest.

Humphrey describes five general steps to the formation of a constitutive relation, which are colloquially abbreviated by the mnemonic DEICE: "delineation of the general characteristics of interest," "establishing an appropriate theoretical framework," "identification of specific functional forms," "calculation of the values of associated material parameters," and "evaluation of the predictive capability of the final relation." Characteristics of tissue behavior include nonlinearity, pseudo- or viscoelasticity, and anisotropy. The theoretical framework includes the establishment of independent and dependent variables. A constitutive functional form is the mathematical formulation used to the describe the mechanical behavior as a function of material parameters. Lastly, the material parameters must be calculated and the model verified for its ability to fit experimental data. With modern computing power, it is possible to calculate many unique best-fit material parameters for a constitutive relation through a technique known as nonlinear regression, allowing for the formulation of more comprehensive and physiologically relevant mathematical models.

One of the most important concepts belying constitutive relations is the use of the hyperelastic strain-energy function *W* to relate stress and strain, proven to be applicable to soft tissue by Y.C. Fung. Briefly, strain energy is the energy stored in tissue when it undergoes strain and is seen in the following relation (Fung, 1993):

$$S_{ij} = \frac{\partial(p_o W)}{\partial E_{ij}}$$

S is the stress component, *E* is the strain component, *W* is the strain energy function, and p_o is density. The first constitutive model for biaxial data was developed for rabbit skin and used an exponential functional form as the mathematical foundation for calculating strain energy (Tong and Fung, 1976). It has subsequently remained the most popular constitutive model for biomechanical studies, due to is relative simplicity and goodness of fit.

Despite the usefulness of the Fung-type strain energy relation as a first step, as a phenomenological model, the parameters calculated for the model do not directly correspond to material parameters. It may therefore be more desirable to use a microstructurally motivated model such as the two-fiber family model (Holzapfel and Gasser, 2001), which contains material parameters that correlate with material parameters such as modulus and orientation. A four-fiber family constitutive model has also been proposed (Baek, 2007) and applied successfully to modeling of vasculature (Gleason, 2008; Lee, 2013).

B4. THE NEED FOR TESTING OF REPRODUCTIVE TISSUE

Mechanical testing has been performed to great success for many varieties of tissue. The field of women's reproduction, however, especially with regards to planar biaxial data describing the mechanical properties of reproductive tissue, remains largely unexplored.

During pregnancy and labor, the female reproductive organs are placed under immense mechanical loads, necessitating significant remodeling of reproductive tissue to accommodate the growing fetus and, during labor and parturition, the expulsion of the infant. Ideally remodeling during pregnancy increases the distensibility of the tissue and afterward restores the reproductive organs to their original non-pregnant state, but this has not proven to be the case. Pregnancy and parturition often produce long-term effects in reproductive tissue that remodeling does not seem to adequately negate. In addition, maladaptive remodeling during pregnancy can lead to complications during birth, including the growing problem of preterm birth. The causes of these syndromes are still relatively unknown and have yet been adequately elucidated. Finally, many women experience non-life-threatening but greatly discomforting pelvic disorders, such as pelvic organ prolapse, of which the etiologies are still relatively unknown. In short, identifying treatments for pelvic floor disorders could greatly increase quality of life for patients as well as decrease infant mortality and disability.

Treatments for these conditions may be found in computational models that take a microstructurally-inspired approach to tissue biomechanics. Reproductive organs undergo dramatic changes in their mechanical environment and exhibit, as discussed previously, complex mechanical behavior. Changing mechanical properties of reproductive tissue may contribute to complications that arise during and after parturition; these mechanical properties can be attributed to microstructural components such as collagen and elastin. Other components like smooth muscle cells may also play a role in the complex biomechanical environment latent in these tissues. Creating comprehensive, predictive models that correlate mechanical properties with constituent components could allow for

the design of informed clinical studies, more quantitative diagnoses of these disorders, and the development of more effective treatments and reassessment of the efficacy of existing treatments.

To this end planar biaxial testing of tissue from reproductive organs, such as the cervix, vagina, and uterus, may help shed light on the mechanical behavior of these tissues. Although uniaxial tests have been performed, biaxial tests are needed for fitting full constitutive models that can then be used to inform in the clinical environment. As discussed, biaxial tests better replicate the *in vivo* loading environment of tissue as well as account for anisotropy in the tissue. Hence biaxial testing could be a powerful tool to apply towards the quantitative description of female reproductive organs.

C. OBJECTIVES

With regards to the biaxial mechanical testing of female reproductive tissue, the objectives of this thesis were as follows:

1. The first objective was to design, construct, and program a planar biaxial mechanical testing device to test a variety of soft tissue, including reproductive tissue. Descriptions of the building and programming are provided herein. Components and software modules are examined for their efficacy, robustness, accuracy, and fit with the specimens to be tested. Such components of vital importance include the custom grips that are used to hold the sample.
2. The second objective was to validate the constructed biaxial testing device using murine skin, which has been mechanically tested in previous studies. To test the skin biaxially required the development of protocol to dissect, grip, and finally run mechanical experiments on the tissue. The results were compared with those found in literature.

3. The third objective was to develop experimental protocols for studies on reproductive tissues to examine their mechanical properties and the implications such properties have for describing the mechanical state of preterm birth and pelvic organ prolapse. Concerning preterm birth, we hypothesize that the uterus and cervix may exhibit different mechanical properties and therefore perhaps different mechanical etiologies for preterm labor. Concerning pelvic organ prolapse, we hypothesize that elastin degradation contributes to mechanical dysfunction of the vaginal and uterosacral ligament.

These objectives will be further explored individually in the following chapters. In common with the experimental objectives, the end goal is to create comprehensive structure-function relationships that describe the mechanical properties of these tissues as a function of the constituents that compose their extracellular matrix. Changes in constituent balance and geometry may be observed via histology and used to inform constitutive models

Chapter 2. Construction and Programming of a Planar Biaxial Testing Device

A. INTRODUCTION

A planar biaxial mechanical test provides data on the response of a material to two directions of stress. Soft tissue like skin, blood vessels, or reproductive tissue is the material of interest in the case of soft tissue biomechanics. The tissues must often be prepared for testing by dissection and gripping of small, representative samples. For quantifying these tissues biaxially, a quasi-static test is desirable in which forces experienced by the specimen due to acceleration from the motor system are negligible. A planar biaxial device contains the sensors and actuators capable of running a biaxial test.

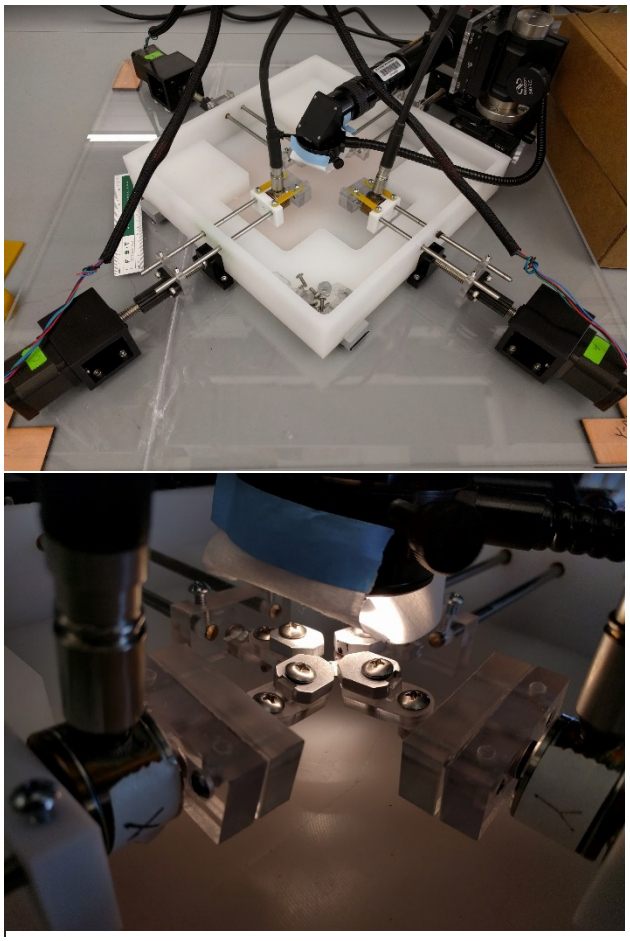

Figure 4: (Top) Overview picture of planar biaxial testing device (Bottom) Closer look at gripping system of device that holds tissue

Uniaxial tests considering only one axis have been more commonly used in previous studies of tissue due to ease of preparation and testing protocol; however, biaxial tests are required to characterize tissue anisotropy and create 3D constitutive models (Sacks and Wei Sun, 2003). Although individual uniaxial tests can be conducted

using orthogonal tissue strips to delineate anisotropy, comparison studies between uniaxial and biaxial tissue tests found significant differences in experimental results such as stiffness (Röhrnbauer, 2013; Mauri, 2013; Gregory and Callaghan, 2011; Lally, 2004). Because most tissues experience complex, multi-axial loading *in vivo*, there is a need to mechanically test tissues in biaxial configurations to attain more physiologically relevant conditions.

Many previous studies have utilized commercial uniaxial devices to test tissue. Commercial testing devices are often made for more robust materials, such as rubber and wood, which are also available in larger sizes. Such devices are comprised of components that are optimal for the testing of such materials. Tissue, especially human tissue from biopsies, can often only be harvested as small samples, necessitating a mechanical testing device that has been specifically optimized for the testing of such tissues to improve accuracy of results and ensure physiologically relevant conditions. To this end, this thesis describes the construction and programing of a custom-designed biaxial device for the purposes of testing soft tissues. The device reported herein provides testing conditions and loading closer to *in vivo* and can record small localized tissue changes throughout testing.

To accurately record data and minimize artifacts, a properly designed planar biaxial device must be more complex than a uniaxial one and meet certain criteria, as outlined by Sacks (Sacks, 2000):

- The device must control boundary conditions in both axes of testing, ideally allowing free lateral expansion of tissue.
- The region of interest, where strain is analyzed, should be in a state of uniform stress and strain.

- The region of interest should be appropriate distant from the grips that boundary effects present at the grips are minimized in the area of analysis.
- The measurement of strain should be done in a way that minimizes tissue interference; non-contact methods such as optical strain tracking are recommended.

In addition to the general requirements outlined by Sacks, the constructed biaxial device follows lab-specific requirements:

- The device is capable of testing tissue with a region of analysis as small as 5mm x 5mm and tendon in the millimeter range. This is a requirement due to the scale of many soft tissue samples.
- The device allows the sample to be placed into a bioreactor to maintain physiological conditions such as temperature and humidity.

The basic modules of the constructed biaxial device are based on designs from David Simon (Yale, New Haven, CT). In the following chapter, the construction and programming of such a biaxial device will be described. Further, this report will delineate novel improvements and optimizations that have been made in comparison to previous designs and commercially available products.

B. MODULES OF THE DEVICE

The planar biaxial device can be broken into five main modules:

B1. MOTOR SYSTEM

Many commercially available devices used in previous studies fix the material sample at one end and then apply linear displacement at the other end, but this configuration only applies load at one end of the sample. In the body, tissues are loaded multi-axially, hence the current biaxial device utilizes four stepper motors (Advanced Micro Systems, Liberty Hill, Texas), with two on each orthogonal axis. In this way, tensile loading is

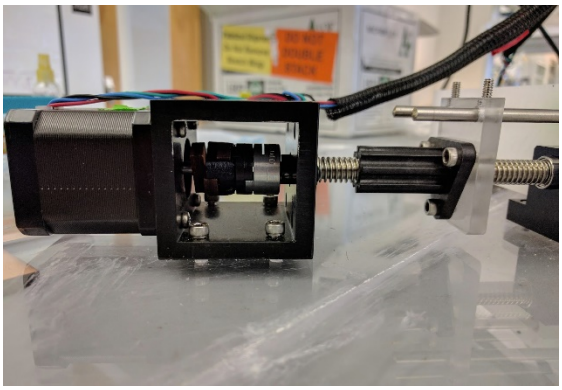

Figure 5: The motor system converts rotational motion into linear motion and runs at micrometer precision.

applied on four sides of the tissue, more closely mimicking loading *in vivo*. The motors are connected to linear screws that move the grips, allowing linear movement along both axes. Each motor is connected to its own independent controller (Advanced Micro Systems), which allows independent control via software interface. Independent control allows feedback to tune each motor for optimal control of displacement during experimental protocol. Multiple improvements were incorporated into software control to track real-time position of the motors through feedback from the controllers.

For the testing of small soft tissue samples, the motors and the backend system satisfy the following design criteria:

- Each motor should be able to move precisely enough that small strains in the order of micrometers are observable. The device runs the motors at 3200 steps per revolution, allowing increments of 0.1125 degrees and a linear translation within a tolerance of 5 micrometers in optical strain without severely limiting strain rate.
- Acceleration should be slow enough that quasi-static testing conditions are achieved. In the current configuration, data is only recorded when the motors are not moving, eliminating accelerative forces. Additionally, strain rate is limited by software to prevent tissue damage from high speeds.
- The motor system should be able to keep track of each motor's step location relative to an origin. Unlike traditional DC motors, stepper motors move in discrete "steps"

that are able to be precisely recorded. Motor and grip location, commonly used in simpler grip-to-grip deformation calculations, can be easily determined.

B2. LOAD CELLS

Two high-precision load cells (Honeywell, Morris Plains, New Jersey) are located one per axis on the loading arms of the device. When an experimental test is run, they record forces due to the stretch applied by the motors. These forces can later be converted to stresses in the principal axes.

Commercial devices use high-range load cells in the hundreds or thousands of pounds for testing of stiff materials. When applied to soft tissues, measured loads only lie in the lowest loading regime of the sensor. Because maximum voltage output from load cells are limited by their small excitation voltage, very small loads only cause sub-millivolt readings, possibly below the noise floor of the sensor. The maximum loading that can be applied on the transducer should be above the maximum forces the tested tissue will experience to prevent damage to the load cell, but the load cell loading range should be closer to the physiological loading range of the tested tissue so that loading data can span the entire voltage range of the sensor for best precision.

The current load cells in the device were determined to be adequate to account for the variety of tissues that may be tested in the device, from more compliant uterine tissue to stiffer tendon tissue. The first load cell selected had a maximum load of 50 grams, based on the original design. This loading range has been applied successfully in mechanical testing experiments, such as for rat thoracic ducts (Caulk, 2015), and a similar load cell of 60 grams was used for rabbit skin tests (Lanir and Fung, 1974). It was found during preliminary validation of the device that the grips, two of which are supported by the load cells, placed a moment on the loading axis of the sensors, causing force normal to the

loading direction. For 50 g load cells, this moment force was over half the maximum load that could be applied, severely limiting the stress testing range of the device and limiting the range of data that could be measured. Mechanical tests on tissues like tendon could easily surmount the maximum loading range. The construction of the load cells also necessitated complex adapters to secure to grips without significant grip rotation.

Load cell range varies from study to study but usually possesses a significantly higher loading limit than the testing range requires, which could cause the measurements of the lowest loads applied to tissue to be inaccurate. Experiments on rat cerebral arteries used 20 N load cells, equivalent to about 2,000 g (Becker and Vita, 2015). A 4,500 g load cell was used in studies of ovine dura matter (Shetya, 2014). Studies on human arteries used a 1,000 g load cell (Azadani, 2013), and uterine tissue experiments used both 1,000 g load cells (Omari, 2015) and 500 g load cells (Mondragon, 2017). A 50 lbf. or ~22,500 g load cell was used to successfully mechanically test murine cervix (Barone, 2012). Manoogian et al. have performed dynamic mechanical tests of pregnant uterus using both 10 lbf. or ~4,500 g load cells for uniaxial studies on human uteri (Manoogian, 2012) and 100 lbf. or ~45,000 g load cells for biaxial studies on porcine uteri (Manoogian, 2008). Rubod et al. used 1000 N or ~100 kg. load cells to run successful uniaxial tests on vaginal tissue (Rubod, 2007).

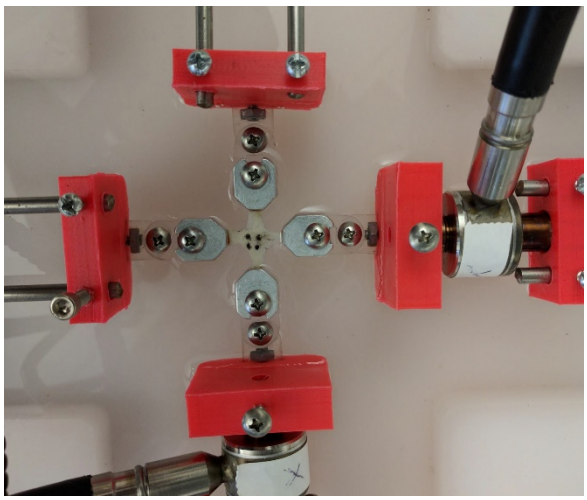

Figure 6: Overhead view of device showing configuration of load cells on each axis. Skin sample has been loaded into device.

Because the biaxial device was designed to test and characterize small samples of soft tissue with focus on reproductive tissue, and because it was desirable to preserve precision, new 5 lbf. or ~2300 g load cells were selected for the device. The range allows for multiple disparate tissues to be tested, where maximum loading differs between tissues. These load cells also feature overload protection and, unlike the first load cells, have asymmetric mounts to prevent grip rotation during testing, an important feature that maintains tissue plane.

The selected load cells satisfy the following requirements:

- The load cells should have a high precision capable of measuring the differences between small forces.
- The load cells and their cables should be submersible should the need arise to test tissue in a bioreactor system that maintains physiological conditions such as body temperature.
- The maximum load rating of the load cells should be high enough that a mechanical test can be completely run without damaging the sensors.

B3. CAMERA SYSTEM

A large advantage the present device has compared to other mechanical testing devices is the ability to image and compute tissue deformation in real time. Other studies often record deformation to be processed separately from testing device data, but the imaging system discussed herein provides real-time feedback to inform running experimental protocol. To this end, a high-resolution grayscale camera (Allied Vision, Burnaby, BC Canada) and macro lens system (Navitar Inc., Rochester, New York) was placed above the testing site. For recording deformations, discrete dark markers can be placed on the specimen to allow for four-particle tracking to take place. Alternatively, the

sample can be speckle-coated to increase texture contrast and deformation-tracked by using digital image correlation (DIC) techniques, allowing full-field strain visualization.

The camera in the original biaxial design only imaged at 656x494 resolution. The current camera runs at a much higher resolution of 2048x2048. This resolution allows for imaging to occur at lower magnifications, if high strain is expected, or for more precise sub-pixel strain calculations at higher magnification. The improvement in imaging resolution yielded an improvement in maximum strain tracking precision by a factor of 3.

New components were added to the controlling software that allowed manipulation of camera properties and visualization of the image in real-time. This allowed the user to optimize the image before running mechanical tests to ensure that strain tracking was reliable. Additionally, the ability to see incoming data from the device is important for improving experimental protocol and to aid the experimenter in checking device accuracy, hence the software was improved to allow visualization of real-time video feed from the camera with overlaid tracking boxes.

The camera system and backend software satisfied the following criteria:

- The camera should be capable of recording high resolution imagery, necessary for most precise particle tracking, that can be visualized in real time. Gray scale is adequate for luma analysis of particles and texture and given the monochromatic nature of most isolated tissues. Monochrome sensors also tend to be sharper since there is no need for a bayer filter to separate color channels.
- The camera should record images at a high enough speed during mechanical tests. The current camera records images at 30 frames per second, more than enough to keep up with quasi-static tests. It should be noted that in the case of dynamic tests,

where tissue is pulled at high accelerations and velocities, a high-speed camera recording thousands of frames per second may become necessary.

- Lighting and exposure should be user controllable. The current camera and programming system allow changes to gain and exposure time to keep the image at a quality suitable for strain tracking. Exposure time should be quick enough that it doesn't cause motion blur or a delay between the image feed and the experimental protocol. Additionally, gain should be limited due to the noise introduced into the image at higher gains, which could interfere with tracking.

B4. TANK

The mechanical devices used in previous studies often are vertically oriented, necessitating that tissue be loaded in a suspended configuration. When loaded in this manner, however, tissue may become dehydrated and exhibit changed material properties. In the discussed biaxial device, this issue was solved by using a horizontally-oriented design to allow tissue to be tested in a custom tank. The sample is held in a physiologically balanced solution to maintain tissue hydration and material properties during a test. The total time that a tissue can remain loaded in the device is improved, and more experiments can be run on individual tissue samples before they need to be replaced, expanding the data that can be gathered. Tank and specimen can also be placed into a bioreactor chamber that maintains physiological conditions while testing occurs.

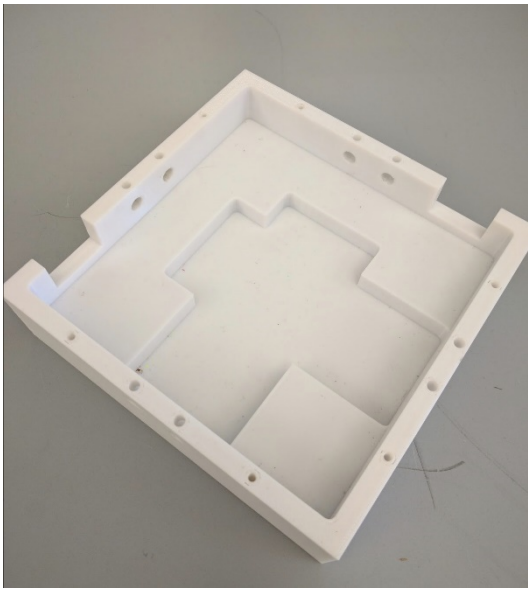

Figure 7: A tank is necessary to immerse tissue samples to prevent dehydration and changing material properties during testing

During the design phase, the tank was optimized and enlarged. In the original biaxial design, the tank was 7.5 in. x 7.5 in. Commercial 3D printing processes were utilized, making a dense and nonporous tank that was not possible using consumer 3D printers available in the university makerspace. During construction and testing, however, it was realized that the tank was too small for the grip, adapter, and specimen structure combined, limiting linear travel.

Improving upon the original tank, a second tank was designed and created using a CNC machine from low density polyethylene. The newly designed tank is 12 in. x 12 in. in width and length, with a similar height. Because it was milled from a single block of plastic, the new tank is also watertight and nonporous. The new tank fit the entire grip assembly and allowed ample linear travel for each motor. The final design of the tank will be fabricated from glass-filled polycarbonate, which can withstand autoclave temperatures and so can be sterilized and placed in an incubator for possible future studies.

The tank satisfied the following requirements:

- The tank should be waterproof to contain the saline bath. The current tank was milled using a CNC machine from a single piece of low density polyethylene and has no orifices or cracks that allow leakage.
- The tank should be large enough to fully hold and test the specimen of interest. The current tank measures one foot by one foot and provides ample space to test samples.
- The material of the tank should not contaminate the solution bath or the sample, possibly affecting material properties due to degradation of the tissue. The final tank will be made from polycarbonate, a plastic often used in medical applications.

B5. GRIPS

Properly designed grips are of vital importance for proper functioning of a planar biaxial device. In the context of this thesis, the topics of grips will include both the physical component holding the tissue specimen and the shape of the tissue specimen. Substantial improvements were made to the grips used in the original device design and in commercially available devices and will be further detailed in the next sections.

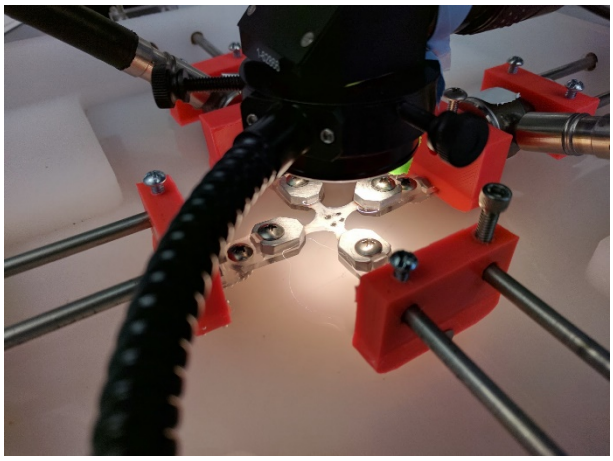

Figure 8: Skin sample, immersed in physiological solution, being held by grips. Tissue is pulled in two principal axes.

Briefly, grips should satisfy the following requirements:

- Grips should minimize boundary conditions for the measure of accurate data that represents the sample rather than the sample and the grip.
- Tissue should be held in place firmly and without any slippage.
- The grips should be capable of holding samples with analysis regions as small as 5mm x 5mm.
- Samples should be aligned as much as possible with the axes of the grips so rigid body motion, shearing, and fiber reorientation issues are minimized.
- Tissue plane should be parallel to camera plane.

C. TISSUE GRIPS

Custom-made grips were used throughout the construction and validation of the biaxial device. Because it is often not feasible to extract large tissue samples, it was important to design grips that would be able to adequately hold small samples without

slippage. They also had to be designed so that all four grips when pushed together could contain a region as small as 5mm x 5mm.

In designing grips, several factors must be considered: the gripping method, the sample shape, and the manufacturability of the grip, each of which will now be examined.

C1. TYPES OF GRIPS

With mechanical tests of tissue, most discussion centers around two grips: clamping grips and suture grips. Clamping grips were first used with testing of non-biological material. Their advantage lies with the ease of setting and securing a sample and continuous force distribution along the tissue. Uniaxial tests, for instance, often use custom clamping grips in the testing devices. For holding tissue securely, sandpaper and adhesives are often used in conjunction with the grips. Suture, or tether, grips instead use suturing thread to hold a sample to the loading axes. Most often, several threads are placed in each side of the sample, while still allowing free lateral expansion of the sample. Suture grips were used during the first biaxial tests (Lanir and Fung, 1974) and remain a popular method of gripping tissue. Four sutures per side is generally sufficient to create the desired stress field in the region of analysis (Sun, 2005). Suture grips, however, create forces that can lead to failure at points in the tissue and may not necessarily reflect optimal physiological loading conditions experienced *in vivo* since the suture points do not engage all tissue fibers under loading.

C2. FACTORS AFFECTING ACCURACY

Studies on clamping grips, using finite element analysis, have discovered that clamps introduce boundary conditions at the clamp-tissue interface that can lead to artificially inflated stiffness in the mechanical response curve (Waldman and Lee, 2005). Although it may seem more physiologically relevant to have a continuous force distribution

along the tissue sample rather than point loads due to suturing, the clamps introduce stress-shielding effects that limit transfer of force to the region of analysis while increasing stress in sample corners (Sun, 2005). This effect may be contributed to the inability of tissue to laterally expand when clamped; suture grips have no such constraints on the tissue. Since tissue behaves in a complex nonlinear, anisotropic manner, such artifacts are a significant confounding factor in achieving accurate results, which generally require involved correcting functions and inverse finite-element-based methods to compute (Nolan and McGarry, 2016).

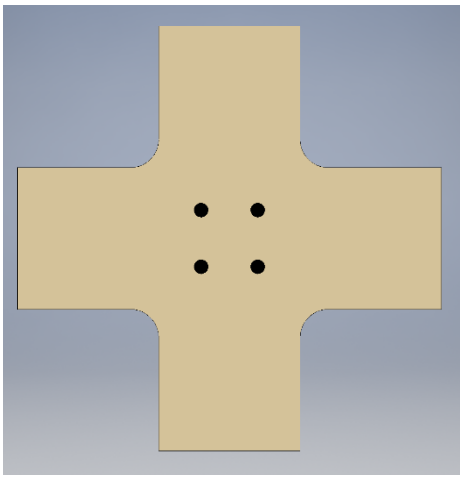

Figure 9: Cruciform sample design with 1mm corner fillets and optical strain tracking markers

Several methods can be used to increase accuracy in mechanical tests. Sample shape can play a key role in the transfer of grip stresses to the region of analysis. Square-shaped samples, due to stress-shielding, have been found to allow only 37% stress transfer, while cruciform-shaped samples can transfer 73% of the applied stress to the central region because there is tissue directly between the grips and less stress concentration (Jacobs, 2013). Finite element simulations and physical experiments for optimized redesigns of cruciform specimens, incorporating multiple slotted arms, allow almost all grip stress to be transferred to the central region and have a reported error that could be lower than 0.5% (Zhao, 2014). The use of fillets in the sample corners can also affect results, with “cut-in” fillets appearing to decrease the effective arm length needed to create a uniform strain field (Hu, 2014). With standard cruciform specimens, minimization of the corner radius

increases stress transfer to the inner region but also increases stress concentration, possibly causing early failure; a small fillet of 1mm may still maintain stress transfer while minimizing deleterious concentration (Bell, 2012).

Another factor that affects accuracy is the size of the region of analysis versus the overall sample size. Due to St. Venant's principle, the region of analysis should be sufficiently distant from the local stresses of the tissue-grip interface so that resultant strain is of a negligible magnitude and the stress distribution is uniform (Love, 1920). Thus, using a cruciform specimen with longer arms, and thus a decreased aspect ratio, or a larger square specimen could decrease artifacts that lead to inaccuracies.

Finally, a last factor that could influence accuracy is initial tissue fiber alignment and engagement. It can be seen that if fibers were initially aligned between two adjacent grips in a biaxial test, most of the stress would be concentrated in those fibers rather than be transferred to the central region (Fan and Sacks, 2014). The overall effect of misaligned fibers is increased stress concentrations and less stress transfer to the region of analysis (Jacobs, 2013). Even slight misalignment between the testing axes and the preferred fiber orientations of anisotropic tissue creates shear stress that leads to inaccuracies in measured axial stresses and rigid body rotation (Zhang, 2015). Evidence shows that the greater the degree of alignment between collagen fibers and the axes of loading, the more grip stress is transferred to the central region (Sun, 2005). It should be noted that collagen fibers will reorient to the direction of loading regardless of gripping method; however, the two main gripping methods each have disadvantages that lead to different results. Suture grips do not adequately engage all fibers and result in discontinuous loading; clamps transfer most

stress to orthogonally-gripped fibers, which become engaged before central fibers (Waldman, 2002).

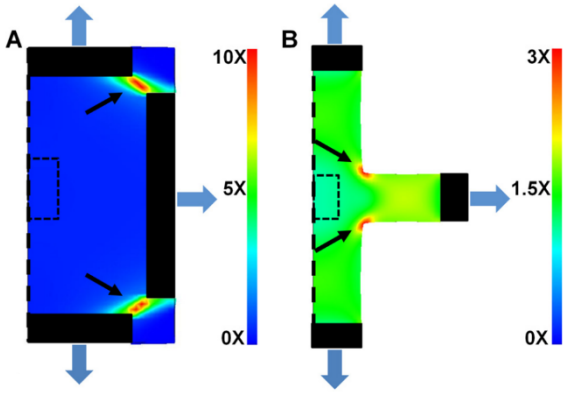

Figure 10: Finite element model deomonstrating the stress shielding effect of clamping a square sample versus a cruciform sample (Jacobs, 2013).

A more practical aspect of accuracy to consider is whether the tissue is exactly parallel to the camera lens. The acceptable focal plane of the lens at high magnifications is small enough that slight misalignments can cause some tissue tracking dots to become out of focus. Changes in perspective that cannot be accounted for using a two-dimensional camera system can also affect accuracy. It is therefore important to keep the tissue plane as parallel to the focal plane as possible, a feat that can be accomplished through grip design. Another practical factor to consider is securing the sample to the grips. The sample must be tightly held in place throughout testing or artificial displacement could be observed in results. When a tissue fails, however, it must be observed whether it failed in the central region, indicating the ultimate tensile strength of the tissue, or at the grips, indicating an artifact of gripping.

C3. METHODS OF GRIP MANUFACTURE

Multiple methods were explored to create custom-designed grips for the device. Novel use of filament-based 3D printers, such as the Ultimaker 2 (Ultimaker, Cambridge, MA) and the Lulzbot TAZ 5 (Aleph Objects, Loveland, CO), allowed for rapid prototyping and one-piece grips, but efforts were stymied by imprecisions in the technology and available filament material. PLA is a safe biodegradable plastic that is popular for use with 3D printers, but a sturdier, more robust material was desired for the final grips. 3D printers

work by extruding layers onto a bed to build up a final three-dimensional object, a process that can take a significant amount of time if many complicated parts are involved. The nature of this method leads to visible layer lines in parts and misalignments between layers, especially prevalent with small-scale prints, required for the grips. Finally, the method causes the component to be structurally weak if shearing stress is applied. Nonetheless, during initial design 3D printing was advantageous due to ease of fabrication and use.

Later grips were fabricated using a Helix 50W laser cutter (Epilog, Golden, CO), which has the ability to cut relevant materials such as acrylic. While laser cutters were eventually used to create larger, less precise parts to the device like the base and various adapters, they proved insufficient to create grips. The main advantage of this technology, as with 3D printing, is ease of use. Designs can be directly printed at high speed, allowing rapid yet precise prototyping. The main disadvantage is that laser cutters work in two-dimensional space, necessitating complex component remodeling and fitting to ensure a 3D part can be assembled. Due to the size constraints of the grips, the compromises needed to create the final parts proved untenable.

CNC machining, though requiring more time, skill, and cost, was eventually used to create the final grips. With this method, it was possible to create small parts that were still strong and stable since materials like aluminum were available. CNC machining has near the three-dimensional capabilities of 3D printers along with the precision of laser cutters, thus allowing the grips to be created with few compromises. Unfortunately, the skill required to machine parts using this method is much higher and required outsourcing of the fabrication to a company, while the first two methods could be done in the university makerspace.

Finally, Ember 3D printers (Autodesk, Mill Valley, CA), which use resin-based 3D printing technology, were utilized to create supporting adapters to connect the grips to the load cells and rod support system. The printers cure a proprietary solution in layers to create an object, allowing great precision and almost no striations in the final product. The cost of solution is high, however, and printing beds are limited to objects of only about three inches in width or length. Due to the proprietary nature of the solution, it is also difficult to know whether contamination of the test setting would occur. It should be noted that the formulation has recently been made open-source. Resin-based 3D printing was not explored until late in the build process of the biaxial device; its possibilities should be explored in later design iterations, including grip design.

C4. GRIP ITERATIONS AND VARIATIONS

Initial grip designs were created using 3D printers and laser cutters and designed with modularity in mind. Different tissues may have different optimal gripping methods. For example, suture grips on tendon would cause early failure due to fiber alignment parallel to loading. Initial grip designs were printed as a single piece with wide clamps or suture points. Initial suture grips combined rake and suture methods to ease the suturing process and minimize space taken up by threads. When 3D printing yielded structurally unstable grips, the 2D laser cutter was used to cut grips out in several pieces for assembly. These initial designs, especially the multi-part grips, proved too large for small tissue testing; the grips interfered with each other. Future iterations decreased grip size considerably.

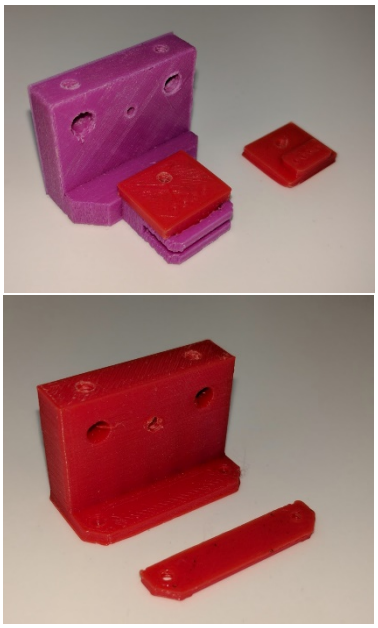

Figure 11: Initial 3D printed grip design for sutures (top) and clamps (bottom)

Simple suture grips were constructed by wrapping sutures around a screw in the loading area and passing the sutures through tissue. A custom MatLab script was written to calculate required thread length for number of suture points. Using sutures and hooks can damage tissue, however, so new clamps were redesigned to be as small as possible. Clamps have the additional advantage of streamlining the gripping process to one clamp per side instead of multiple suture points.

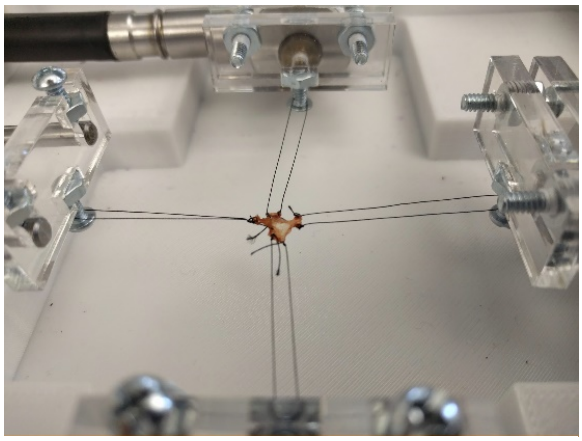

Figure 12: Suture grip design using vertical screws as pulleys prior to alignment

C5. FINAL GRIP DESIGN

The final grips were custom-fabricated by a machine shop and were designed using CAD software. The final materials used were aluminum and polycarbonate, which are easy to clean and also rigid enough for mechanically testing tissue. It was decided that, for ease of gripping and the size scale involved, clamps would be used to hold tissue, with their undesirable boundary conditions offset using cruciform-shaped samples as described in the previous section. Prototype suture grips were created, using a bottom mounted screw to allow free pulley-like movement, but were eventually superseded by clamp grips. Detailed drawings of the grips can be found in Appendix D.

The grips used in the first biaxial design were two blocks which were pressed together on rods to hold the sample in place. Although this method could securely hold larger samples of tissue or tissue constructs, it was not capable of gripping small tissue

samples. Additionally, the blocks bent sample arms vertically in the grips, which introduces substantial boundary effects and is not physiologically accurate. Commercially available devices also utilize grips that are often much larger than tissue sample and not designed with gripping tissue in mind. In biaxial testing of small samples, previous grips would interfere with each other.

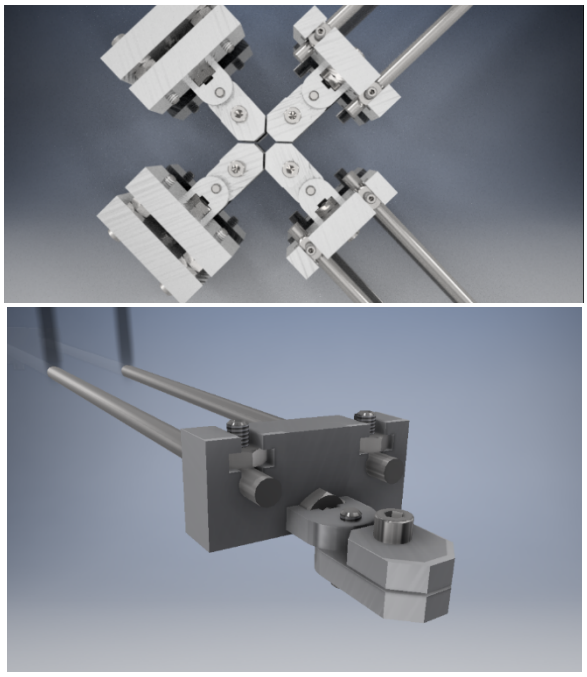

Figure 13: (top) CAD renderings of final grip design assembled in biaxial testing configuration. Grips without rods are attached to load cells. (bottom) View of individual grip assembly

In the improved grip design, the clamps are coplanar to the tissue sample and feature chamfered corners that allow for holding of a sample with a region of analysis of as small as 5mm x 5mm despite the larger dimensions of the clamp. Because the grips are coplanar, there are no boundary conditions induced by tissue bending. The grips are much smaller than previously used designs and are more applicable to holding small samples. When loaded into the device, the ease of determining whether samples are aligned and adjusting the samples are improved.

Unlike in previous grip designs, which require two or more screws to secure a sample, it was determined that only one screw is needed to hold the clamp jaws together, with an elevation in the bottom grip preventing the top grip from freely rotating. Friction between sample and clamp is increased by use of low-grit sandpaper, folded end-over-end.

Sandpaper has been used in previous mechanical tests to securely grip tissue (Lyons, 2014; Manoogian, 2012; Szczesny, 2012; Röhrnbauer, 2013).

The clamps are composed of several smaller components. The clamp to tissue interface is composed of two "jaws" that screw into each other. This jaw superstructure is held by another single screw to a rod-to-grip adapter that allows the grips to be held by the existing biaxial rods. The use of a single screw at this juncture allows the jaws to be tightened with an angular offset or even pivot freely. Load cell grips are offset in height to remain level with the other grips to keep tissue coplanar with the camera.

In addition to maintaining co-planarity to tissue, other substantial improvements were also made to the interfaces between the samples, grips, and the linear motor system. The previous design integrated the two systems together, while the new design allows the grips to be easily mounted and unmounted using a single screw. The screw interface also allows adjustments to be made to grip angle to improve alignment of the sample. With this redesign of the interface, the entire grip system can be removed to allow gripping of the sample and then mounted back into the device for testing. The system is also highly modular; different tissue-specific grips can be easily placed into the device. The construction of the grips themselves also allow for different top and bottom jaws that have been optimized for specific tissues.

A grip assisting tool was created using a 3D printer that allows the four grips to be aligned during sample gripping. Within this tool, the grips and mounted sample can then be easily transferred and secured to the biaxial testing area. Stamping tools are used to cut the samples to predefined shapes to ensure uniformity between samples. With the

improvements made to gripping method and process, a tissue sample can be more accurately and securely gripped in a manner closer to physiological conditions.

D6. TENDON GRIPS

Most tendons are predominantly loaded in one direction *in vivo* and are transversely orthotropic. They are stiff in the direction of loading while being compliant orthogonally to that axis. Another grip was designed to facilitate uniaxial testing of tendon, such as murine supraspinatus tendon. Clamping-style grips in a uniaxial configuration have been previously used to mechanically test tendon (Connizzo, 2014; Screen, 2003; Legerlotz, 2014; Stäubli, 1999). The final design, based on the work of Lin (Lin, 2004), used a modified version of the previously described final grip design and is indicative of the versatility of the improved grip design.

A tapered channel was cut into the top grip, while bone compaction mixtures was used for the opposite grip. Dissected tendons were still attached to bone: the patella and femur. The patella fits into the channel but, due to the taper, is not able to slide out. The femur is crushed with polymethylmethacrylate and compacted to form a mixture that able to be held by the existing sandpaper gripping method. During mechanical testing, the aspect ratio should be sufficiently high to satisfy St. Venant's principle, with a testing length of greater than eight diameters appearing to satisfy the criterion (Jimenez, 1989).

D7. GRIPPING PROTOCOL

Prior to testing, a sample is stamped into a cruciform shape, which as previously described minimizes boundary conditions. The region of analysis must be at least 5mm x 5mm. Increasing arm length up to twice the central region length will improve the stress field of the central region. Some of the arm will be contained by the sandpaper and thus will not be part of the effective arm length.

Next, the biaxial device should be configured to accept the sample. The adapters should be moved in until the grip holes fit over the adapter holes. The camera is mounted on a magnetic platform and can be easily moved to the side to allow free access to the motion system.

Folded sandpaper is adhered to the top and bottom of each arm using cyanoacrylate. The bottom grips are then placed into the grip aligner assistant followed by the cruciform sample, with each sandpaper tab aligned with a grip. The top grips are then aligned for each bottom grip and screwed in place tightly. The entire grip complex, including the assistant, is then transferred to the biaxial tank. The grips can then be screwed in at the same time into the device. Care should be taken to prevent lateral forces on the load cells while tightening the screws. After the sample and grips are secured, the assistant device can be removed.

E. SOFTWARE DEVELOPMENT

Software was developed to interface with and run experiments on the biaxial testing device and also to analyze the resulting data. Two main pieces of code are available: a LabView interface for controlling the device and MatLab (MathWorks, Natick, MA) code to perform more extensive analysis and display data. Software development took a significant portion of design and build time. This custom software builds upon biaxial program routines and was written specifically to facilitate tissue testing and is capable to applying and analyzing small strains and loads. As will be detailed, a number of significant innovations have been made compared to mechanical testing control software used in previous devices.

During the software planning stage, it was determined that LabView was to be used to control the device due to robust built-in high-level hardware interfacing tools and

parallel-tasking-centric language. During mechanical testing, several subsystems must run in tandem to ensure each data point and image is matched to a time point. The diagram style of LabView allows for multiple simultaneous threads to be easily created and visualized.

MatLab is a popular high-level programming language that can be used to process large amounts of data. It features informative debugging messages and many built-in functions that greatly ease the process of developing a script. In addition, it features highly functional image processing and statistics toolsets. Processes that did not need to run in real time could be made in MatLab, where more intense data processing could occur that may be less feasible to implement in LabView, including full-field displacement of tissue.

E1. LABVIEW

The LabView program is composed of multiple subprograms, known as "virtual instruments." The program takes inputs from the camera and two load cells and feedback from four motor drivers. It outputs a deformation gradient based on four points in the region of interest, assuming the central field deforms homogenously; force data converted to Newtons; raw pixel coordinates of point displacement; and images taken during mechanical testing. The motion aspect of the program is capable of running mechanical tests with user-defined parameters. A detailed description of how to use the LabView program can be found in Appendix M. Description of VIs may be found in Appendix P.

E1.1. MOTION

The motion subsystem utilizes serial data transfer protocol built into LabView to send commands to the motor drivers. The motor drivers are daisy-chained together and handled by an additional controller that is able to parse incoming data streams to each individual controller. All motors can thus be individually addressed but can also move

simultaneously through sending a single line of code. Motor parameters that can be controlled include initial and slew velocity and step size. The distance each motor moves per command is in the units of steps; the program converts millimeter displacements into steps, considering step size. The motion subsystem also tracks feedback from the motor controllers, allowing precise determination of the step location of each motor.

E1.2. FORCE DATA

The load cells run in a bridged configuration where voltage varies in proportion to load. A LabView calibration tool is used to properly map load in grams to volts. During calibration, the load cell is aligned towards the floor and precise, successively increasing test weights are hung to create the loading curve. When absolute load is calibrated, the load cells can be further relatively calibrated by zeroing within the data acquisition subsystem.

E1.3. IMAGE ANALYSIS AND TRACKING

A significant advantage the present custom biaxial device has over other devices is the use of strain-controlled experimental protocol. Most mechanical testing devices run stress-controlled tests and measure grip-to-grip deformation, which is the distance between grips, whereas the present device optically tracks local tissue strain in the region of analysis. Grip-to-grip tracking is simple to process, but fails to describe actual local tissue deformation. It is a function of tissue deformation, shearing, boundary effects, and grips, and so does not adequately isolate tissue strain. Additionally, since the device tracks local tissue strain in real-time, it has the additional advantage of being able to provide feedback when running testing protocols to ensure all experimental parameters on each axis are reached. Experiments which utilize separate video recording can process local strain data but are not capable of providing real-time feedback to testing protocols. The use of optical

strain tracking also allows more complex experimental protocols to run, including testing shearing deformation, although they are beyond the scope of this thesis. The creation of an optical tracking system, however, is complex and difficult. A significant portion of software, hardware, and protocol development time was spent ensuring real-time optical strain tracking could occur.

The first software component, accurate image tracking, is of paramount importance when running mechanical tests. In four-point tracking, the tissue being tested must contrast as highly as possible with the tracking markers, which can range from India ink or activated charcoal to poppy seeds or vanilla bean flakes. It was found during validation of the system that overhead light should be bright yet diffused to prevent track-breaking specular reflections in the tissue and tracking markers. These reflections, of high luminance values, often had the effect of causing the image analysis algorithm to break a single particle into multiple pieces. Finally, imperfections and crimps in the tissue can also cause artifacts in the program.

Several settings and processing methods were incorporated into the software to improve tracking accuracy. Low level settings on the camera, not previously accessible, were made into user-adjustable parameters and were visualized in real-time. During preliminary testing, it was found that the starting image was vital for image analysis. Contributing most to image quality in tests were two settings: exposure time and gain, two parts of the "exposure triangle" that adapts to any lighting situation. Since the camera is fixed-aperture system, any exposure adjustments must be accomplished through software. Exposure time allows the cleanest increase in exposure, but may lead to motion artifacts or image-capture delay if the exposure time is too long. Hence gain is used as a secondary

factor to adjust exposure. Gain changes the amount of digital amplification applied to the camera sensor, which can increase image noise, which may adversely affect tracking. During tests, it was found that a gain of 10, an exposure time of 15,000, and maximum brightness on the light source with diffusion was sufficient to expose the sample. It was additionally found that immersing the sample in solution increased contrast and diffused light. The combination of adjustment software, controlled lighting, and immersion substantially advances optical strain tracking reliability compared to other devices, which often rely on ambient lighting or separate camera equipment.

The imaging subsystem allows all available camera settings to be adjusted. The waveform of the image, which displays distribution of luminance values, can be invaluable in determining proper exposure. In an ideal exposure, the dark tracking dots should cause a spike in the low end of the waveform while the rest of the image causes bunching of the waveform towards the high end. This waveform represents a high contrast image that has the highest chance of being tracked accurately.

The second step of image processing involves thresholding the image properly. The LabView and MatLab programs determines tracking markers by locating particles within the image; thresholding attempts to separate particles from background by forcing values below or above a certain threshold to become pure black or pure white respectively. This step is accomplished through user input to isolate the particles and select the markers to track. It should be noted that the thresholding algorithm is a general processing step that can also amplify artifacts. Before thresholding, applied grayscale morphological transformations function effectively as low-pass filters to dampen high-frequency artifacting.

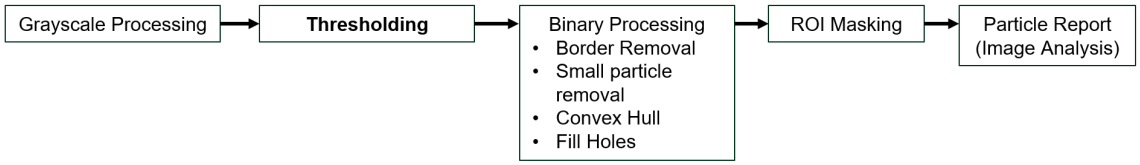

Figure 14: Flow chart describing image processing and analysis steps for particle tracking

The third step incorporates built-in LabView image processing sub-VIs to extract particles from the image. The program rejects borders and searches for particles using a linking algorithm that combines neighboring white points in a 3x3 pixel grid. Often, many particles emerge from this processing; additional algorithms limit particles to a certain size and shape (low pass filtering which removes small particles) and conform each particle to a simplified shape (convex hull, fill holes).

The final step once again involves user input. Four tracking markers must be selected in a processed image. Despite processing, erroneous stray particles may still be present, which are masked out when the four markers are selected. Although the stray particles are still present, the program will only heed to the selected marker.

Tracking occurs using a particle reporting VI that detects individual particles and generates a list of their subpixel locations. Using this method, a high degree of accuracy can be achieved. The VI additionally determines a bounding box that encompasses each particle, but the existing implementation did not allow room for whole particle movement or expansion, hence the calculated centroid might not be the actual centroid of the tracking marker. A search region and recovery module was added that allowed the program to adapt to marker geometry change and whole marker movement that greatly improved strain tracking. If tracking is temporarily lost, the program will adaptively adjust the bounding box to attempt to relocate the particle, minimizing disruption to an experiment. This

system was a key feature in facilitating real-time optical strain tracking. Tissue markers may deform with tissue under load and requires a system that can adapt during testing.

During a test, tracking occurs via a simple implementation of the nearest neighbor algorithm, in which the deformed particle location nearest to the reference particle location is assumed to be that particle. Although more complex algorithms could account for adverse situations and possibly increase tracking accuracy, the simple approach is robust enough for most mechanical tests, where tracking markers are unlikely to cross or change size significantly.

E1.4. DEFORMATION GRADIENT CALCULATION

The deformation gradient is calculated by the LabView and MatLab programs using principles described by Sacks (Sacks, 2000) and finite element theories. The deformation gradient **F** is defined as:

$$\boldsymbol{F} = \frac{\partial \boldsymbol{u}}{\partial \boldsymbol{X}} + \boldsymbol{I} \quad (1)$$

where **u** is the displacement vector, with respect to the original configuration **X**, and **I** is the identity matrix. Within the deformed four points, from a reference configuration, it is possible to calculate the deformation at any point within the quadrilateral by using bilinear interpolation. A simple method for determining any point deformation is to weigh the influence of each of the four corner points on the point of interest and then simply to average the results from the four points. Because the shape of the four points may not necessarily align with the global x- and y-axis, isoparametric shape functions are used to interpolate the points' locations and deformations to aligned axes, labeled *r* and *s*.

Sacks writes these transformations mathematically:

$$\boldsymbol{u}(r,s) = \sum_{n=1}^{m} f_n(r,s)\boldsymbol{u}_n \quad (2)$$

where $\boldsymbol{u}_n$ is the vector displacement of tracking marker *n*, f_n is the described shape function, and *r, s* are the equivalent coordinates in the transformed system. Equally weighing the four points through linear interpolation, equation (2) can be rewritten:

$$\boldsymbol{u}(r,s) = \frac{1}{4}\sum_{n=1}^{4}(1+(-1)^n r)\left(1+(-1)^{\left\lfloor\frac{n+1}{2}\right\rfloor} s\right)\boldsymbol{u}_n \quad (3)$$

The goal, however, is to describe the deformations with respect to the original axes. Because of the use of isoparametric functions, the original configuration **X** can also be written with respect to the aligned axes and the matrix inverted to write the aligned axes with respect to the original axes (Humphrey, 1987). Thus, defining *u* as horizontal displacement and *v* as vertical displacement, **F** can be written as:

$$\boldsymbol{F} = \boldsymbol{I} + \begin{bmatrix} \frac{\partial u}{\partial X} & \frac{\partial u}{\partial Y} \\ \frac{\partial v}{\partial X} & \frac{\partial v}{\partial y} \end{bmatrix} = \boldsymbol{I} + \begin{bmatrix} \frac{\partial u}{\partial r} & \frac{\partial u}{\partial s} \\ \frac{\partial v}{\partial r} & \frac{\partial v}{\partial s} \end{bmatrix} \begin{bmatrix} \frac{\partial X}{\partial r} & \frac{\partial X}{\partial s} \\ \frac{\partial Y}{\partial r} & \frac{\partial Y}{\partial s} \end{bmatrix}^{-1} \quad (4)$$

In the deformation gradient subVI, the eight individual matrix components are calculated from tracked data. Since the device only tests principal stresses, ideally with oriented tissue shear stresses should remain negligible during experiments. Derivatives with respect to *r* and *s* can be computed easily from equation (3).

E1.5. TROUBLESHOOTING

LabView's wiring-diagram programming structure unfortunately rendered bugs difficult to diagnose. To debug the program, use of the probe tool proved instrumental to finding errors; the probe displayed data in real-time as it was manipulated, allowing problem routines that outputted erroneous values to be repaired.

Most issues focused on the tracking and image processing modules of the program. It was found that testing a rubber glove supplanted testing a real tissue sample during the

debugging stage. When testing the skin sample, it was difficult to decipher whether results were due to human error, sample variation, or programming issues. Gloves, cut into cruciform shapes with scissors, provided a uniform, repeatable specimen that allowed isolation of most programming issues. It should be noted that stress concentrations within the sharp cruciform corners tended to make the glove samples tear more easily than skin. The purpose of using glove samples, however, was not to evaluate mechanical testing results but to develop and debug program modules, hence sample mechanical differences were not deemed significant.

E2. MATLAB

A custom MatLab program was developed to augment and expand the capabilities of the basic LabView software interface. More complex image correlation techniques and tracking methods were written to process raw data from the device. Additionally, in-lab constitutive model fitting scripts were developed in MatLab that could be used to determine material parameters for biaxial data. Regarding image processing and tracking, any MatLab script does not need to heed real-time requirements and thus more intense computation can occur, such as full-field displacement. A detailed description of program usage can be found in Appendix N and O. The MatLab component extends the features of the device beyond the original design.

The MatLab code also performs additional calculations to convert the deformation gradient into the Green strain tensor:

$$\boldsymbol{E} = \frac{1}{2}(\boldsymbol{F}^T\boldsymbol{F} - \boldsymbol{I})$$

Where $\boldsymbol{F}$ is the deformation gradient. Left and right Cauchy-Green strain tensors can also thus be calculated:

$$\boldsymbol{C = F^T F; B = F F^T}$$

Both tensors are independent of rigid body rotation. For Green strain, the strain in the principal directions can be simplified to:

$$E_{11} = \frac{1}{2}(\lambda_1^2 - 1)$$

$$E_{22} = \frac{1}{2}(\lambda_2^2 - 1)$$

Where λ_i is the measured strain from the deformation gradient along the stretched axes of a biaxial test.

Force is also converted into Cauchy stress by calculation of the theoretical cross-sectional area of an incompressible material. The data can then be used as the base to parameterize a constitutive model.

E2.1. IMAGE IMPORT

The device stores camera feed in a *.tiff image sequence, which does not suffer the compression or smearing that may be present on devices which utilize separate video cameras. A subfunction was written to import sequences of images in the *.tiff format. The sequence must be stored in its own folder, but the file names do not need to obey any specific rules. A sorting algorithm ensures that each successive image is placed correctly in the sequence. To save memory, images are loaded only as needed.

Once the image is imported, it displays a preview in the user interface. Users can scroll through the sequence intuitively using a scroll bar or by inputting the specific frame number. Image processing occurs as each image is loaded.

E2.2. IMAGE PROCESSING

Preliminary image processing occurs in three steps. The first step involves basic contrast adjustments to increase overall contrast and separate light from dark values. The

second step inverts the image to bring out tracking particles as light against a dark background. The final preliminary step applies a threshold to the image, like in the LabView interface. The threshold is again changed by the experimenter. Decreasing the threshold value may cause elements that are not particles to be located by the algorithm due to similar luminance values; increasing the threshold may fail to isolate particles that are not light enough.

Built-in MatLab particle reporting functions were used to isolate and report pixel values of particles. For other tracking methods, the user must select the particles manually. Particles are automatically sorted into individual quadrants within the global axes to simplify particle selection and analysis. In addition, tools were created to visualize the centroid of each search particle and tracking search regions.

E2.3. TRACKING METHODS

The user must select a search region to begin tracking. The larger the search region, the greater the displacement rate of the particle can be maintained before tracking is lost; however, greater computational time is required and errant particles may be interpreted as the reference particle.

Particle correlation methods utilize the subfunction SimpleTracker (Tinavez, 2011, MatLab Central). More complex algorithms are used in the MatLab code, compared to the LabView software, that can fill and interpolate gaps in

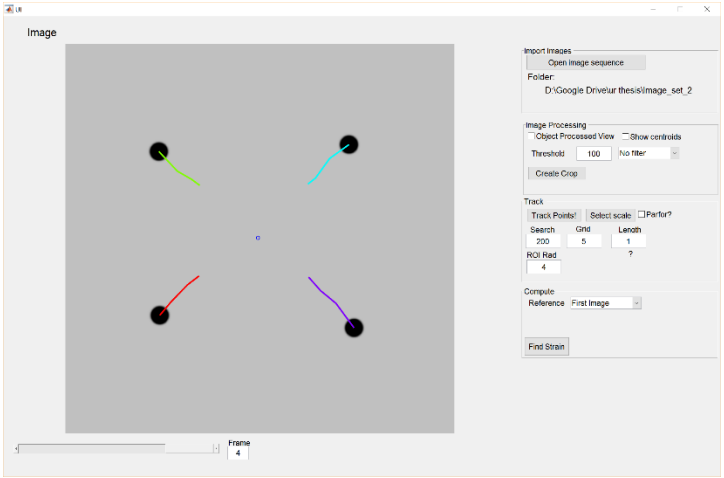

Figure 15: User interface designed in MatLab. Tracking trajectories are shown after successful tracking has occurred. Program options are arranged on the right side of the UI to allow real-time adjustments of parameters.

tracking. The first is the use of the Hungarian algorithm during initial tracking to minimize the distance between each particle's reference and deformed configuration but also to minimize overall distances between all particles. During this phase, particles may fail to be detected in the next image and are left blank in the tracking array. During the second phase of tracking, after initial tracking has occurred, the nearest-neighbor algorithm is used to close gaps where a particle was not detected. The tracking can thus fail across frames without inhibiting the ability of the program to perform a sufficient track of the particles. This double-checking approach would be difficult to apply in real-time to LabView because a full dataset of displacements is needed to re-link broken tracks.

E2.4. CORRELATION METHODS

a. FOUR-POINT TEXTURE CORRELATION

In other mechanical testing software packages, often only one tracking method is provided. Besides particle analysis, two extra subfunctions were written, with the goal that different functions incorporating different correlation methods may account for image sequence where only one method may not work. These methods utilized a computational rather than analytical approach to arriving at marker locations. Four-point texture correlation was the name given to the function that bridged the gap between digital image correlation (DIC) and particle detection. While DIC is capable of full-field displacements, particle detection is better suited to known numbers of particles. With particle detection, each particle is found based on linking algorithms. In cases where particles are not visible enough or do not contrast enough for the background, it can prove more useful to match, or correlate, small image sub-regions. A generalized tracking method that utilizes texture matching is given in the Figure 10. Unlike particle tracking, this method cannot

spontaneously lose particles and can adapt to changes in marker shape or lighting conditions.

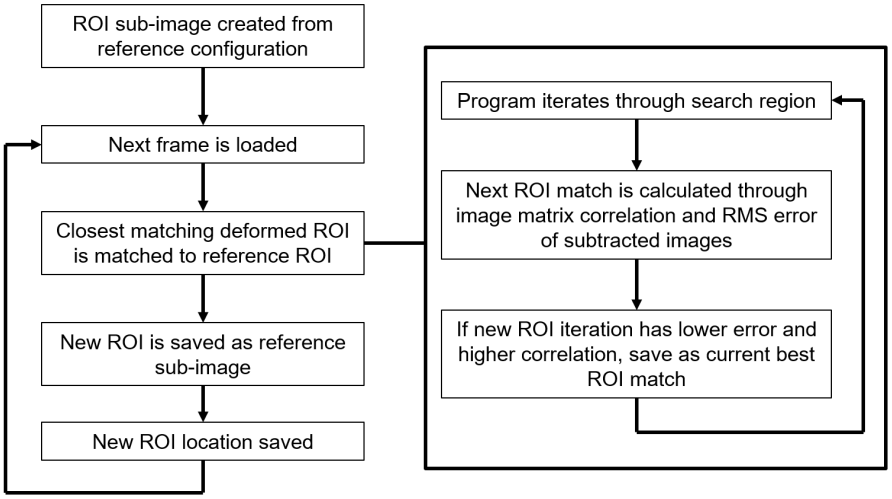

Figure 16: Flow chart describing a generalized method for tracking via texture matching

In some cases, a simplified model of deformation that assumes a homogenous strain field is desired. Where particle detection fails, texture correlation of the four points can possibly be used. A reference region is first selected by the experimenter. The next frame is then loaded and a search window used to look near the reference particle and find its deformed location. A modified version of the Pearson correlation coefficient was used to match the texture of the sub-region in the reference and deformed states. The deformed region with the highest correlation coefficient is selected as the probable area where the particle has moved.

Image subtraction is also used in tandem with the correlation coefficient. Two identical images, when their luminance values are arithmetically subtracted, will return a pure black image. This principle was used to find similar deformed regions to the reference region, with the lowest root-mean-square (RMS) error from an all-black image being the determining factor in choosing a region. Unfortunately, image subtraction and RMS error

proved to be computationally intensive and, in its current implementation, not suitable for real-time use.

b. DIC METHOD WITH TEXTURE CORRELATION

Previous iterations of mechanical testing devices either do not use optical strain tracking or only use simplified four-point tracking. Full-field DIC tracks all local deformations within the region of analysis, fully describing the strain field during a test, and is the most accurate but computationally intense method of measuring strain. A preliminary version of full-field DIC was implemented in the MatLab program to lay the foundations for full-field experiments. It generates a grid of points within a user-selected region. Each individual grid point is then tracked, and an individual deformation gradient can then be calculated for each set of four points.

For this method, it is better to speckle-coat a sample to produce local contrasts within the sample, enhancing texture, rather than place four particles. Image correlation and subtraction is again used to match regions between images. The built-in function *corr2,* which utilizes the Pearson correlation algorithm, returns a correlation coefficient. A high value indicates good correlation between the reference and deformed sub-image matrices. Image subtraction arithmetically subtracts pixel values between the reference and deformed sub-images. If the two images are closely matched, the resulting difference will look like a black image. Deviances from pure black are calculated as RMS error. The program weighs the two values and chooses the deformed sub-image that averages the lowest RMS error and highest correlation coefficient.

F. LIMITATIONS

Planar biaxial testing, while a good starting point to developing descriptive models of tissue behavior, can only fully describe isotropic materials; for transversely isotropic

materials, as many tissues are characterized, additional methods are required. Holzapfel and Ogden describe four constitutive strain-energy functions for a general transversely isotropic specimen; however, a planar biaxial test only can control for three unique components in two dimensions, thus rendering a full description of these materials impossible. These three components are seen in the left Cauchy-Green tensor **B** below:

$$\boldsymbol{F} = \begin{pmatrix} F_{11} & F_{12} \\ F_{21} & F_{22} \end{pmatrix}; \boldsymbol{B} = \begin{pmatrix} B_{11} & B_{12} \\ B_{12} & B_{22} \end{pmatrix}$$

Further, they propose the addition of in-plane shear or a through-thickness shear test to obtain the fourth independent variable (Holzapfel and Ogden, 2009).

Additionally, when calculating Cauchy stress, it is assumed the cross-sectional area undergoes homogenous normal stress and the biaxial stress ratio remains constant, but finite element simulations show evidence that these assumptions are overly simplistic (Nolan and McGarry, 2016).

Lastly, the camera and recorded images operate in 8-bit monochrome color space; each pixel can be described by only 255 shades of gray, from 0 for pure black to 255 for pure white. Color imaging or a high bit-depth could increase tracking accuracy by allowing more nuance in shading and texture correlation. The existing pattern matching algorithm in the MatLab code also does not perform subpixel sampling, limiting precision to within one pixel.

Chapter 3. Validation of Planar Biaxial Device Using Murine Skin

A. INTRODUCTION

After the construction and programming of the planar biaxial mechanical testing device, it was necessary to validate its results by running a pilot study on a sample tissue and comparing results from the device to those found in literature. If calculated mechanical properties and stress-strain data were statistically comparable to those found from previous experiments, future data from the biaxial device would be validated with at least previously established mechanical testing methodologies. If results were significantly different from previous results, without validation, it would be impossible to prove whether novel results were indicative of a new scientific discovery or device inaccuracy.

Murine skin was chosen as the test sample for device validation due to its wide availability within the research lab and its well-characterized mechanical properties (Groves, 2013; Muñoz, 2008; Karimi, 2015; Del Prete, 2004). Additionally, many non-murine skin models from previous studies can also be found in literature, including for cat skin (Veronda and Westmann, 1970) and rabbit skin (Lanir and Fung, 1974). Murine tissue can serve as an analog to human tissue, which is a more ideal specimen but harder to obtain; murine skin exhibits similar morphology and anisotropic, viscoelastic properties to human skin (Groves, 2013), and can thus be used to provide insights into human skin structure-function relationships.

As Holzapfel argues, skin can serve as a simplified representative sample of soft tissue in general, mirroring many characteristics of these tissue (Holzapfel, 2000). The

main structural constituent of skin is collagen fibers, followed by elastin, both of which are arranged in a three-dimension fiber network, like in other soft tissues. In an undeformed state, skin exhibits isotropic behavior; collagen can be observed to be randomly organized and crimped while elastin serves as the main load-bearing component (Holzapfel, 2000). As load is applied, the collagen fibers become uncrimped and, as the fibers gradually align to the direction of load, the tissue gradually stiffens to a linear region (Holzapfel, 2000). This behavior is also observable in other collagen-containing soft tissues. The objective of this chapter is to validate functionality of the planar biaxial device through internal and external validation of individual components and biaxial testing of murine skin and, further, to develop generalized protocol for biaxial gripping and testing of soft tissue.

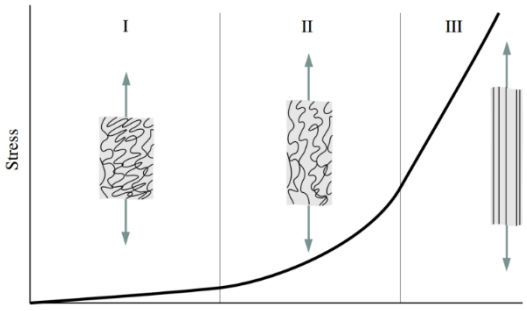

Figure 2: Nonlinear stress-strain behavior of soft tissue due to collagen crimping (Holzapfel, 2000)

B. BACKGROUND

Skin is the largest organ in the human body and aids the body in regulation of homeostasis through heat regulation. Skin additionally forms a tight barrier between the body viscera and the outside world and is the first layer of the immune system (Moore, 2015). The skin can be divided into two layers: the dermis and epidermis. The epidermis is the thinner, superficial layer of the skin and is composed of keratinized epithelial cells; the dermis is the deeper, thicker layer. The dermis is primarily composed of densely arranged collagen and elastin, the constituents which make skin strong and tough (Moore, 2015). The dermis can be further split into the papillary dermis, below the basal lamina of the epithelium cells, and the reticular dermis (Silver, 2006). Deeper to the dermis lies

subcutaneous tissue such as fat, which is often dissected along with and must be removed from skin samples to ensure only the mechanical properties of skin are represented during testing.

In murine aging studies of skin, it was found that collagen type I and type III, which are the main structural collagen components of skin and many other tissues, decreased with age, where collagen type III decreased most significantly (Mays, 1988). Collagen type I is the most common type of collagen and can be found in skin, bone, and tendon, while collagen type III is found more commonly in elastic tissues such as vasculature (Hulmes, 2008). Within the dermis, type I collagen is the main constituent in the reticular layer composing 80-90% of all collagen content while type III collagen is found in higher quantities in the papillary layer (Silver, 2006). Reticular collagen forms a random, undulating network of thick fibers, while papillary collagen forms a denser but still randomly oriented network of thin fibers (Silver, 2006). Unoriented fiber networks lend skin its high compliance (Avery and Bailey, 2008). Elastic fibers are present in a continuous three-dimension network throughout the entire dermis, but it is collagen that is primarily responsible for mechanotransduction within the extracellular matrix (Silver, 2006). Skin viscoelastic behavior may be attributed to both elastic fibers, readily stretchable at low strain, and collagen fibers, stiffer but engaged at high strain (Silver and Landis, 2008).

As for mechanical properties, skin is generally considered to be anisotropic, presenting greater compliance in one direction (Lanir and Fung, 1974). Investigations using a skin expansion device using a porcine model determined that skin was isotropically pre-stretched *in vivo* by 1.21 on average; however, skin deformation and growth occurred

in an anisotropic manner when expansion was applied (Tepole, 2015). Thus, there is a need to load skin biaxially to elucidate more physiologically relevant mechanical properties, although difficulties may still be encountered when attempting to correlate such properties with collagen content (Del Prete, 2004).

During remodeling, as seen with wound healing, the extracellular matrix is often poorly regenerated, leading to fibrosis. The collagen network, which is normally configured in a network structure, is reconfigured with dense fibers lying parallel to each other (Martin, 1997). Mechanical tests run on scar tissue compared to normal skin suggested that scar tissue was much stiffer and less extensible than normal skin (Clark, 1996). Although not of focus in this thesis, biaxial investigations of skin to quantify material parameters in poorly remodeled skin and normal skin could suggest intriguing solutions towards describing structural changes required for improved remodeling of wounded tissue.

C. METHODS

C1. VALIDATION OF HARDWARE

The hardware of the device was tested to ensure linear translation, optical strain tracking, and load cells were accurate and consistent. Each motor was zeroed at a reference displacement, then moved 25.4 mm in tension and back to reference. The resulting linear motion was measured using digital calipers with 0.01 mm precision. Optical strain tracking was validated by loading a skin sample in the device and then applying 0.5 mm grip-to-grip tension followed by 0.5 mm return to reference. Load cells were externally validated through calibration of voltage output and creation of a load-voltage fit. Briefly, the load cells were placed in a custom-built calibration tool and loaded in tension with successively

increasing weights from 0 – 2000 g. Voltage values were compared to calibration data provided by the manufacturer, Honeywell, to externally ensure load cells were accurate.

C2. SKIN SAMPLE DISSECTION AND GRIPPING

Skin samples (n = 3) were obtained from previously sacrificed and frozen C57BL/6-strain mice (IACUC approved, Tulane University). A full description of the dissection and gripping protocol may be found in Appendix J and L. Briefly, when available, abdominal skin was dissected from thawed mice. If such skin was not available, thoracic or hind leg skin was instead dissected from the mice. As much as possible, skin sample dimensions were kept above 15 mm x 15 mm. After dissection, skin samples underwent treatment with a commercial mixture of sodium hydroxide and calcium hydroxide to depilate the tissue samples. Samples were harvested and refrozen for future testing. Evidence has been shown that frozen tissues did not show changed mechanical properties from freshly dissected samples (Armentano, 2006).

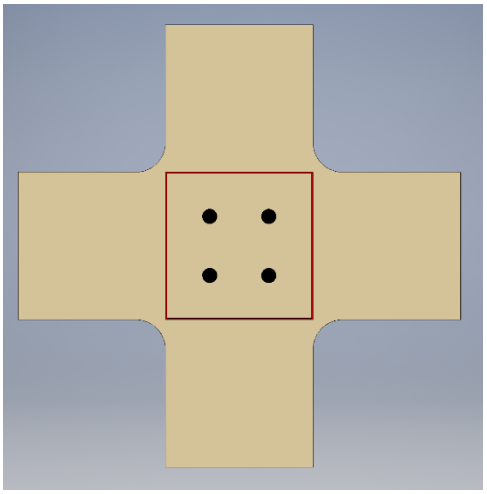

Figure 17: Illustration of the central region of analysis in a cruciform sample

Before gripping, samples were dethawed and cut using scalpels into a cruciform shape with a central region of 5 mm x 5 mm and arms of length 5 mm for a region of interest of 11.1%, within the biaxial dimensions seen in other studies (Vande Geest, 2006; Humphrey, 1987; Waldman and Lee, 2002) where only the central 4 – 20% of a region was considered. Tissue hydration was maintained with Hank's Balanced Salt Solution (HBSS). Double-sided sandpaper was adhered to each side of the cruciform arms using cyanoacrylate. After alignment with the lower grip using a grip assisting device, the arms were clamped and secured in the biaxial testing device.

Initial tissue thickness was measured using digital calipers with 0.01 mm. Four dots were placed in a square configuration in the central region using activated charcoal for optical strain tracking. The tissue was then immersed in HBSS. From that point, all adjustments could be controlled by software.

C2. EXPERIMENTAL PROTOCOL

The reference state of each skin sample was set to a small tare load where the sample lay flat to the imaging plane. The origin and reference configuration was set via the software interface. Preconditioning cycles differed in literature for skin, from four (Muñoz, 2008) and ten cycles (Karimi, 2015); biaxial experiments of other tissues ranged from four (Lee, 2013), nine cycles (Vande Geest, 2006) to fifteen cycles (Sacks and Chuong, 1998). During experimental tests, six cycles were determined sufficient to ensure that results converged for each testing protocol. Although data from all cycles were recorded, only data from the last loading/unloading cycle was used. The skin samples were tested using an equibiaxial protocol, in which the stretch ratio F_{11}:F_{22} was kept at 1:1, and constant stretch protocols using the X-axis as control and then the Y-axis as control. Each cycle ran two equibiaxial tests, one for each control axis. Details of the protocol may be found in Appendix M. Sample strain was optically tracked in real-time assuming a homogenous strain field in the central region. Samples were stretched at a rate of 0.2%/second to a maximum stretch of 2-4 mm grip displacement to ensure tissue did not tear and with a maximum force of 2000 g.

D. RESULTS

D1. VALIDATION OF DEVICE HARDWARE

The motion system was validated by individually and collectively moving the motors and then measuring physical displacement compared to expected software displacement. Mean error for motor linear motion was acceptably low at 0.56% in outward

movement and 0.75% in inward movement. Since the device utilizes optical strain tracking, it is possible to compensate for motor error through tracking feedback.

Optical strain tracking was validated by comparing a reference configuration to a tension-deformed configuration and then a return to the original reference. Paired t-tests ($p < 0.05$) were used to compare reference distances between the four tracking points to both tensile and return to reference deformation. Tissue tensile deformation was significantly different from reference values while returning to reference values were not significantly different from the original reference. This indicated that the optical strain tracking system was accurately tracking and measuring particle distances.

Reference (px)	Tension (px)	Return* (px)
618.2	724.7	630.28
754.38	833.22	755.65
616.57	689.63	625.1
648.8	700.87	624.74

*To reference

Significance	Tension	Return
P (<0.05)	0.006	0.95

Table 1: Paired t-tests were used to evaluate differences between reference-deformed and reference-return to reference tissue deformation. $P < 0.05$ was considered significant.

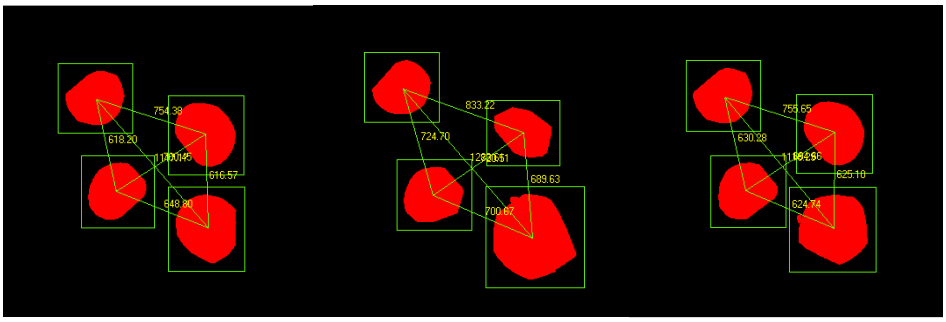

Figure 18: Output images after particle analysis showing distances between tracking markers

The load cells output an mV/V_{ex} reading proportional to the amount of load applied. The load cells were calibrated by Honeywell and were re-verified in lab to ensure voltage was consistent with calibrated values. A loading line was then created for the LabView interface to convert voltage to load in grams. The loading characteristic of both load cells were highly linear with line fits having $R^2 = 1$. These results indicated the load cells were

accurate and voltage could be directly converted to load. Calibration data for the load cells may be found in Appendix R.

D2. MURINE BIAXIAL PILOT TESTS

Biaxial data were compared to murine uniaxial data, which to our knowledge is the only data available from previous studies. Observed experimental results showed mechanical behavior indicative of soft tissues, including preconditioning and hysteresis. Raw data was processed into load-displacement curves and fitted using nonlinear least-squares regression with the Levenberg-Marquardt algorithm and LAR robust fitting. Best fit curves were found to be exponential. Experimental data was compared to murine skin studies performed by Groves et al. (Groves, 2013). Using their data, a standard deviation between samples was calculated of ±0.7234 mm displacement in the circumferential direction and ±0.6945 mm displacement in the axial direction. Respective load-displacement curves from the present biaxial tests in the transverse and axial directions were observed to be within two standard deviations of their data. All final load-displacement curves may be found in Appendix T.

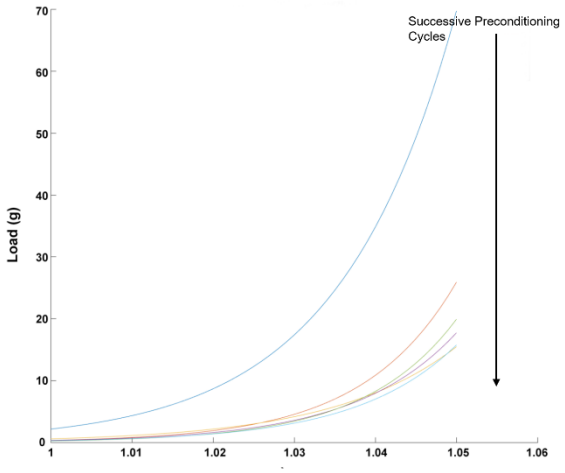

Figure 19: Six successive loading and unloading cycles were used to precondition the samples to achieve converging results for loading and deformation.

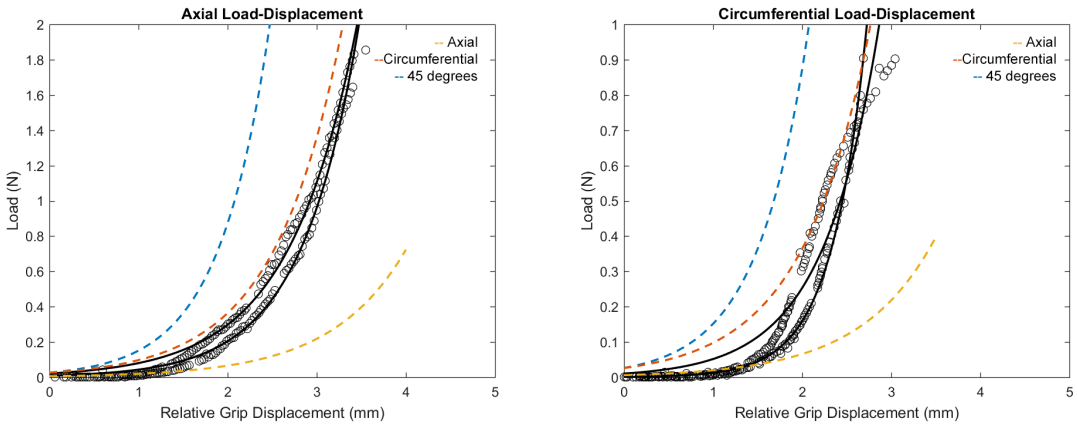

Figure 20: Representative load-displacement loading and unloading data (black) compared to representative data from Groves et al. (blue, red, and yellow)

Raw data was additionally converted into stress-strain curves and compared to murine data from Muñoz et al. (Muñoz, 2008), although only axial data was available. Young's modulus was calculated from their data by fitting a tangent line to the linear region of the last loading cycle in their uniaxial tests. Young's modulus was calculated for the present experimental stress-strain data in the same manner. All calculated Young's moduli may be found in Table 2. Anisotropy was observed for all samples with an increased stiffness in the axial direction compared to the transverse direction, which was also observed by Karimi et al. (Karimi et al. 2015).

		Sample 1		**Sample 2**		**Sample 3**	
	Munoz et al. (2008)	**Axial**	**Transverse**	**Axial**	**Transverse**	**Axial**	**Transverse**
Young's Modulus (MPa)	8.1	7.89	5.62	9.99	8.48	4.58	3.61

Table 2: Calculated Young's modulus for each stress-strain curve

Finally, grip-to-grip strain was evaluated against optical strain tracking. A linear fit was applied with an $R^2 > 0.9$. Local optical strain was lower than grip-to-grip strain for all tissue samples, ranging from 12% to 25% when comparing maximum grip strain to maximum optical strain.

E. DISCUSSION

All components of the biaxial device were individually validated internally and externally and found to be accurate across the testing range. The load cells were found to have a highly linear voltage-load relationship that corresponded to manufacturer calibration. Optical tracking was able to discern small deformations between tissue deformed and reference configuration. Finally, the motion system was able to accurately convert revolutions of the motors into linear translation.

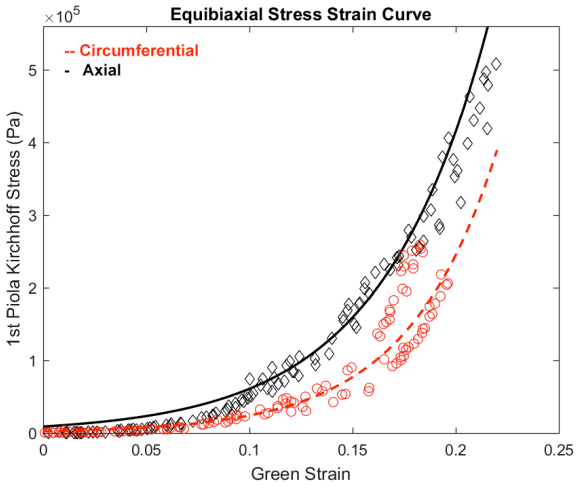

Figure 21: Representative stress-strain curve for axial and transverse directions in biaxial test. The axial direction was found to be stiffer than the transverse direction.

External validation through biaxial tests on murine skin was proven through qualitative and quantitative means. Results from the pilot study on murine skin follow trends in previous studies, although previous studies were limited by uniaxial testing configuration and use of grip-to-grip measurements. Experimental results matched closely with data from Groves et al., demonstrating a compliant toe region with gradual stiffening and anisotropy between the transverse and axial directions. Stiffness in general was qualitatively found to be within range of previous studies, including observations that the transverse direction was less stiff than the axial direction. The stress-strain behavior of murine skin was best described by exponential fits, similar to what has been described by Fung (Fung, 1993). Overall, the device was successfully able to measure the viscoelastic, anisotropic, nonlinear behavior of soft tissue.

Though the present data correspond with data from previous studies, observed discrepancies can be explained by biological variations and differences in testing configuration. In this pilot study, skin samples were dissected from female mice abdomen, while previous studies used skin from mice backs (Groves, 2013) or male mice (Karimi, 2015). Skin could have region- and sex-specific properties which could affect skin mechanical properties. Previous studies have also observed wide variations among individual skin samples.

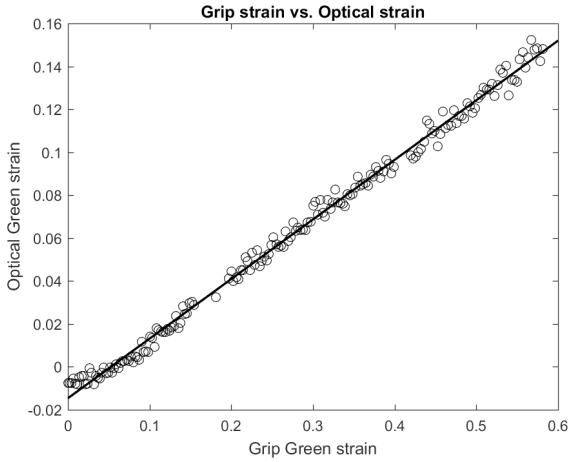

Figure 22: Optical strain followed a linear relationship with grip-to-grip strain. Local strain was less than grip-to-grip in all samples.

Some stress-strain data, notably for the second sample, flattened to a sigmoidal shape at the high strain regime, deviating from expected exponential behavior. This effect could be explained by decreased resilience compared to other skin samples, due to which the sample began to exhibit a plastic rather than elastic response at higher strains, perhaps attributable to fiber restructuring or reorganization. Additionally, at low loading rates, viscoelastic stress relaxation may have affected the skin samples and manifested in stresses that were lower than expected at higher strains.

Additionally, results from biaxial tests differ from uniaxial tests due to axial coupling. Biaxial stress-strain results tend to be stiffer than uniaxial tests because the orthogonal axis is also pulling on the sample, decreasing strain in the measured direction. A uniaxial test that tests tissue in both directions allows free contraction and expansion of

the orthogonal direction, which does not mimic the *in vivo* loading environment and may possibly exaggerate anisotropy.

Optical strain tracking of local deformation was less than applied grip-to-grip deformation. Local strain appeared to follow a linear relationship with grip-to-grip strain. Experimental results are in line with results from Butler et al. (Butler, 1984), which demonstrated that only 25 to 30% of grip-to-grip deformation was observed in the local region of analysis. Because the performed tests were biaxial, less local strain is expected due to the opposing tensile load of the orthogonal axis.

Overall, it was proven that the biaxial device could accurately apply stretch and record resulting deformation and load. The device was used in pilot studies in murine skin to validate the data recorded from the device. Experimental results corresponded to results from previous studies and prove that the planar biaxial testing device is capable of testing soft tissues.

Chapter 4. Future Directions: Mechanical testing of reproductive tissue

4.1. MECHANICAL TESTING OF UTERINE AND CERVICAL TISSUE

A. INTRODUCTION

Preterm birth is a serious medical problem and one of the leading causes of infant mortality. As of 2010, preterm birth had a worldwide rate of 9.6% of all births. The highest incidence of preterm birth (12.5%) occurs in the least developed countries where infants born before 32 weeks have little chance of survival (Beck, 2010). Additionally, children born preterm have higher incidences of developmental disability (Marlow, 2005) as well as vision and hearing disabilities (Moster, 2008).

Despite its grave effect and cost, little is definitively known about the underlying causes of preterm birth. There are also no real preventative measures that can be taken. A large percentage of preterm birth (45%) occurs "spontaneously" without any obvious signs or warning and could have several causes ranging from infection to stress (Goldenberg, 2008). There is therefore a pressing need to create more effective ways to diagnose and treat women susceptible to giving birth prematurely.

Concerning pregnancy, large changes in uterine and cervical tissue must occur before giving birth. The reproductive tract must be able to distend remarkably in order to accommodate the growing infant; it must then also be able to return back to its normal non-birthing state. It is possible that maladaptive remodeling may be occurring in the uterus causing its constituents to prematurely change to a form that is like that of a uterus at term. Premature shortening and ripening of the cervix, such that it can no longer contain the loads of pregnancy, may also likewise arise in part from such remodeling.

Shorter intervals between successive pregnancies have been correlated with an increased chance of preterm labor (Goldenberg, 2008), indicative of inadequately remodeled tissue. In the field of biomechanics, it is understood that the mechanical properties of tissue, such as stiffness and yield stress, are generally related to the composition of the tissue. Differences in major structural components of the extracellular matrix, including collagen and elastic fibers, and their interactions, including crosslinking, arrangement, and fiber ratios, affect overall mechanical behavior. We can deduce these differences by evaluating uterine and cervical structure-function relationships via measuring changes in tissue mechanical behavior and quantitative histology.

Precise mechanical testing using specialized testing devices is used to determine the properties of tissue. A planar biaxial device allows stress-strain characteristics to be derived, and, eventually, constitutive models to be created. Compared to a simpler uniaxial device, which can only stretch tissue on one axis, a planar biaxial device allows for the creation of a more complex, physiologically relevant model that considers tissue anisotropy (Sacks 2000). We hypothesize that for preterm birth to occur smooth muscle phenotype and ECM constituent change due to the influence of the uterine distension. We additionally hypothesize that incomplete repair or disrupted homeostasis of collagen and elastin turnover may occur in the cervix that cause premature dilation. Before such complex, multifactorial conditions can be tested and modeled, baseline tissue stress-strain behavior must be established. We hypothesize that the cervix and uterus may respond differently to mechanobiological stimulation which may elicit different underlying mechanical etiologies of preterm birth. The objective of this study is to develop protocols to extract and compare

biaxial data from healthy uterine and cervical tissue, heretofore unknown to the field of reproductive biomechanics, through planar biaxial testing.

Data from mechanical testing and histology can be used to inform descriptive and predictive constitutive models for reproductive tissue. With such a model, clinically relevant changes in tissue can be directly derived from changes in tissue parameters in the model. Modifying a model to observe changes is significantly more efficient than systematically analyzing tissue samples. Eventually, by mathematically quantifying the changes that occur in the cervix and uterus before, during, and after pregnancy, the difficulty of creating precise, effective diagnoses and treatments is eased. These diagnostic tools and treatment options could decrease infant mortality worldwide.

B. BACKGROUND

B1. PRETERM BIRTH

Preterm birth is characterized as parturition that occurs before term (37 weeks). It is a serious problem, associated with 75% of infant mortality, and a growing one, with incidences having increased 20% from 1981 to 2003 (Iams, 2003). The causes of preterm birth are myriad and complex, including infection, inflammation, mechanical distension, and stress (Goldenberg, 2008). The exact mechanisms by which preterm birth occur are still however poorly quantified, and birth often seems to occur "spontaneously," without apparent signs. It remains difficult to detect premature labor in its early stages.

B2. BIOMECHANICS OF THE UTERUS

B2.1. UTERINE ANATOMY AND CONSTITUENTS

The uterus is a pear-shaped organ which functions to hold the fetus during pregnancy. It is composed of three major layers: the endometrium, myometrium, and perimetrium. The endometrium can be further divided into the functionalis, which is composed of columnar epithelia, and the basalis (Silver, 2006). The myometrium can be

divided into the junctional zone and outer myometrium (Brosens, 1998). The principal active component of the uterus is smooth muscle cell (SMC) bundles, encompassed by connective tissue, arranged in a complex, interwoven network, especially in the myometrium, which is involved in the process of labor (Ramsey, 1994). In the junctional zone, smooth muscle is longitudinally oriented and follows an increasing density gradient with depth while the main myometrium possesses unoriented woven smooth muscle; in the perimetrium, smooth muscle orientation is circumferentially oriented (Brown, 1991). Other constituents include elastin and collagen. Elastin is present in relatively low abundance in the myometrium, decreasing in a gradient from the outer myometrium to the inner myometrium (Metaxa-Mariatou, 2002). Collagen fibers, predominantly type I and type III, are present as a continuous network between the endometrium and myometrium; the superficial layers have no preferred fiber orientation while the deep layers connected to the myometrium contain many parallel lamellae (Goranova, 1996). Biomechanically, the uterus exhibits

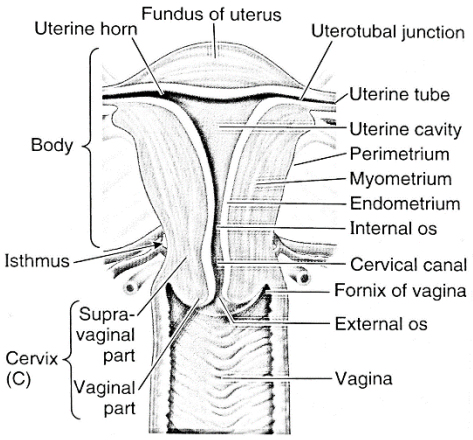

Figure 23: Illustration of female reproductive tract (Moore, 2015)

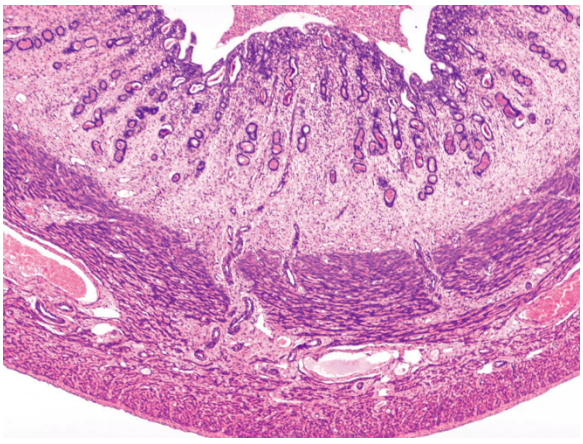

Figure 24: Cross section of uterine wall, courtesy of Histology@Yale

anisotropic behavior and is composed of two intramural circular structures with aligned layers and an outer circular layer with random fiber orientation (Weiss, 2006). Degree of anisotropy increases from nearly isotropic with onset and duration of labor and engagement of fibers (Mizrahi, 1980). Anisotropic materials have direction-dependent material properties.

The greatest muscle content is found at the fundus of the uterus, decreasing eventually from overall 30-40% (Fung, 1993) and 70% in the *corpus uteri* (Mahmoud, 2013) to be continuous with cervical muscle content, about 10% (Ramsey, 1994). Additionally, the uterus is stabilized by several ligaments, the most important of which are the cardinal ligaments, which connect the uterus to the pelvic wall, and the uterosacral ligaments (Ramsey, 1994; Baah-Dwomoh, 2016).

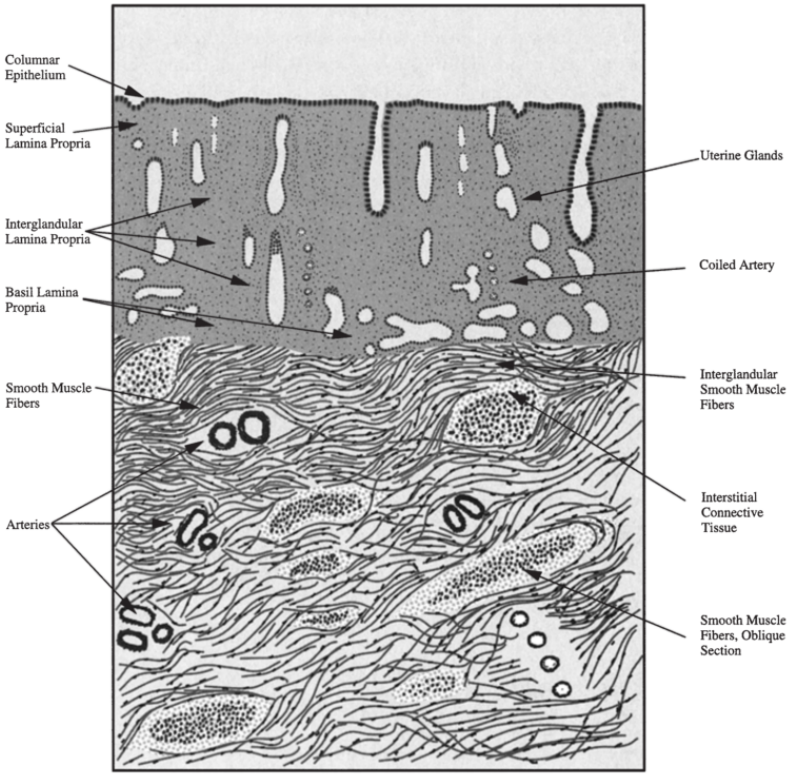

Figure 25: Cross sectional diagram of the uterus (Silver, 2006)

B2.2. UTERINE REMODELING

During pregnancy, the uterus undergoes substantial remodeling to accommodate and eventually deliver the growing fetus. Within the myometrium, the junctional zone eventually dominates and myometrial layers become continuous (Willms, 1995). In the first trimester, myometrial SMCs proliferate and enlarge; SMC hypertrophy occurs until mid-gestation. From this point, mechanical stretch determines uterine growth (Ramsey, 1994). Goranova found evidence that spatial remodeling of the collagen network occurs during pregnancy, due to distension of the uterus and an increase in estrogen. In the endometrium, collagen fibers become more compacted; epithelial proliferation was also observed (Goranova, 1996). Further, investigations in collagen content change during pregnancy and parturition showed dramatic collagen increase in the uterus and to a lesser extent in the cervix during pregnancy and rapidly falling collagen levels after parturition (Harkness and Harkness, 1954). A later more in-depth study found that collagen type I and III levels increased in late gestation but decreased before full term; collagen type IV, fibronectin, and laminin increased on the day of parturition; and elastin expression increased and was maintained at an increased level from mid-gestation (Shynlova, 2004).

Shynlova has proposed that both fetal hormonal endocrine cascades and tension induced by fetal growth in the uterus cause changes in the biomechanical properties of uterine tissue. In particular, the two pathways

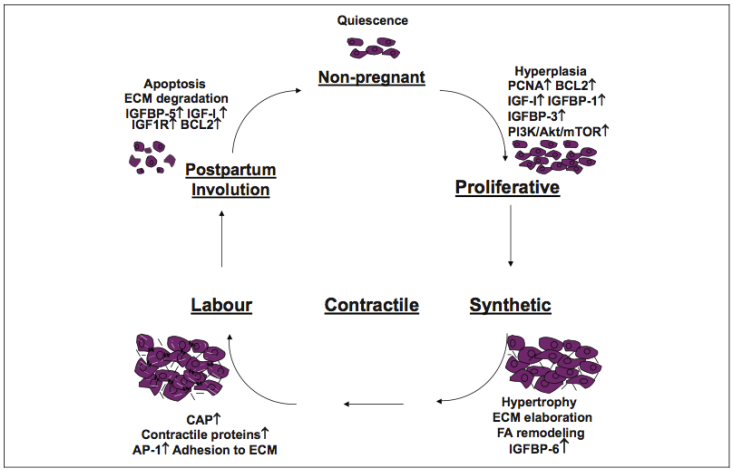

Figure 26: SMC Phenotype through phases of pregnancy (Shynlova, 2013)

are believed to cause substantial changes in smooth muscle cell phenotype from a proliferative to a synthetic (hypertrophic) and finally to a contractile phenotype, which leads to a highly active stage that induces labor (Shynlova, 2009). The stiffness of the extracellular matrix, composed of elastin and collagen fibers, may play a role in remodeling by influencing SMC phenotype (Humphrey, 2014).

Evidence exists that mechanical stretch due to the growing fetus is the primary cause of SMC hypertrophy in the gravid uterine horn (Shynlova, 2010; Csapo, 1965). In Shynlova's rat studies, SMC hypertrophy occurred most prolifically from day 14 to 19 and stabilized at term (day 22). Notably, chronic, non-fetal obstructions also had a similar effect (Lindnér, 1988). The role of SMCs may also change between different phases. Besides labor, SMCs may also play a role in uterine inflammation by excreting chemokines in response to mechanical stretch (Shynlova, 2013). Removal of tension from the gravid uterine horn, such as by giving birth or by surgery, has also been correlated with a decrease in weight and collagen content in that horn. When paired with an ovariectomy, thus removing hormonal influences, the effects are even more pronounced, causing more decrease in mass, suggesting that both hormones and local stress factors play a role in uterine growth (Wray, 1982).

It has been proposed that local uterine and cervical inflammation contributes to labor onset, during which uterine tissue assumes a contractile state, partly as a result of mechanical stress and uterine distension instigating myometrial secretion of proinflammatory factors and permitting immune cell access (Shynlova, 2013). It is possible that premature inflammation from, for example, bacterial infection may trigger uterine phenotype change and initiate labor-related processes that render late-stage

treatments ineffectual (Shynlova, 2013). In late gestation near term, pro-inflammatory Ccl-2 expression was found to have increased greater than twenty-fold in the myometrium and Ccl-2 proteins were found in both longitudinally- and circumferentially-oriented myometrial SMCs; progesterone was found to lower Ccl-2 expression, suggesting a role in maintaining pregnancy, while stretch was found to increase Ccl-2 expression in the absence of progesterone (Shynlova, 2008). Broad Spectrum Chemokine Inhibitors were successfully used to prevent infection-induced preterm birth in mice by decreasing inflammatory chemokine presence (Shynlova, 2014). Inflammatory cytokines have been associated with the release of proteolytic enzymes that digest ECM constituents (Shynlova, 2013).

Although a multitude of factors play a role in initiation of labor in the uterus, uterine distension may play a prominent role in the initiation of signaling cascades, inflammatory chemokine release, smooth muscle phenotype change, and extracellular matrix remodeling. We hypothesize that uterine overdistension may play a role in maladaptive tissue remodeling of structural constituents leading to changed mechanical properties and preterm labor. There is a need to deduce these structure-function relationships to establish the mechanobiological causes of preterm birth.

B3. BIOMECHANICS OF THE CERVIX

B3.1. CERVICAL ANATOMY AND CONSTITUENTS

The cylindrical cervix is considered a part of the lower uterus that serves to keep the fetus within the uterus until term (Ludmir and Sehdev, 2000). Like the uterus, the cervix is supported by the pelvic ligaments. The vaginal facing, inferior aspect is known as the external os; the internal aspect continuous with the uterus is known as the internal os. The cervix can be further split into two layers: an epithelial section and the cervical

stroma. Although smooth muscle and elastin are present in the stroma, it is composed mainly of fibrous collagenous tissue (Moore, 2015), which are responsible for most mechanical behavior (Myers, 2015). Smooth muscle cells and fibroblasts are densest in the inner stroma while extracellular space increases towards the outer stroma (deSouza, 1994). Elastic fibers are found only in a band throughout the cervix, tapering off at the internal os (Leppert, 1986). In the nonpathological cervix, elastic fibers run parallel with dense collagen fibers, which assume a ratio of 70% collagen type I to 30% collagen type III (Ludmir and Sehdev, 2000). Fibril orientation has been quantified in previous studies showing preferred collagen orientation in the radial direction for the inner stroma-epithelial region and in the circumferential direction for the outer stroma, although measuring difficulties were noted for the inner region (Yao, 2016). X-ray diffraction studies showed three distinct zones with different preferred fibril direction: an inner and outer zone with longitudinally aligned fibrils and a middle zone with circumferentially aligned fibrils (Aspden, 1988). It was proposed that circumferential fibrils controlled cervical dilation while longitudinal fibrils maintained uterocervical attachment (Aspden, 1988). Collagen fiber dispersion was also found to be significantly lower within the outer anterior and posterior stroma (Yao, 2016), elevating anisotropic characteristics. Another region-specific difference is evidenced by increased stiffness of the inner os compared to the external os (Yao, 2014). Finally, the cervix possesses substantial viscoelastic properties, including nonlinearity, hysteresis, and stress relaxation in stress-strain relations that are typical of soft tissues (Myers, 2008).

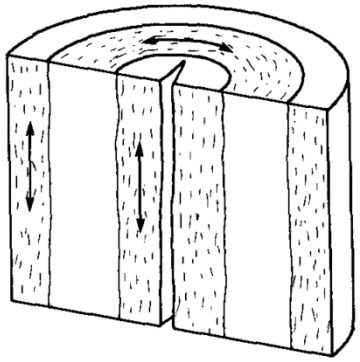

Figure 27: Drawing of preferred collagen alignment in the cervix (Aspden, 1988)

B3.2. CERVICAL REMODELING

To facilitate parturition, the cervix must become significantly less stiff and more distensible to allow for passage of the baby. Deviations from the changes that must occur can cause preterm birth, such as with cervical insufficiency, or post-term birth, where the cervix failed to soften adequately (Yoshida, 2014). During a normal pregnancy, the cervix undergoes four successive phases: softening, ripening, dilation, and repair. During the softening phase, tissue compliance increases gradually. The ripening phase, generally occurring at late term pregnancy causes rapid increase in compliance and decreased tissue competence. Finally, the cervix dilates readily and to great strains to allow parturition. The cervix must then be restored back to its original nulliparous state. These phases are regulated through a complex interplay of endocrinal and immunological systems (Timmons, 2010). Post-pregnancy remodeling may fail to restore the cervix back to its original non-pregnant state as seen in murine tissue (Barone, 2012). Post-pregnancy incomplete remodeling may corroborate observations of a positive correlation between closely spaced pregnancies and increased probability of preterm birth (Goldenberg, 2008).

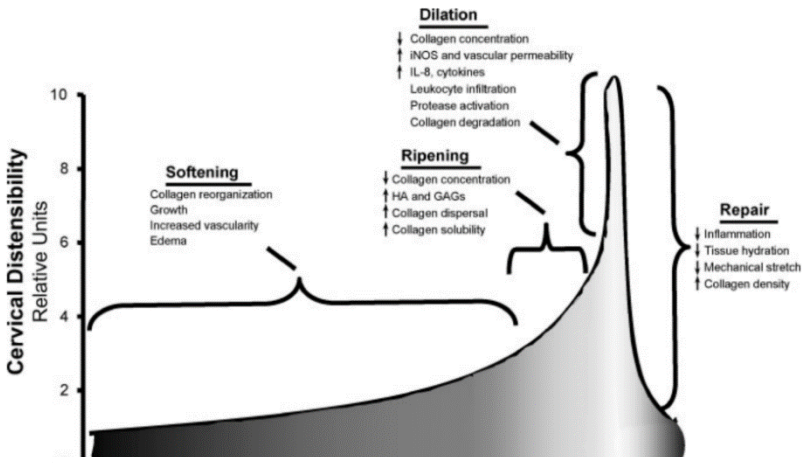

Figure 28: Representative graph detailing stages of cervical remodeling during and after pregnancy (Word, 2007)

During a normal pregnancy, a small proteoglycan called decorin that bonds to collagen upsurges in the cervix, causing collagen fibers to become dispersed and unoriented (Ludmir and Sehdev, 2000; Akins, 2011). Within collagen networks,

decreasing collagen crosslink density (Yoshida, 2014) due to high turnover of mature collagen with new collagen (Akins, 2011) appears to be a key factor in progressive cervical softening. In contradictory studies, collagen type I content has been found to remain similar or increase from nonpregnant to pregnant cervix (Akins, 2011) as well as to decrease by degradation or turnover (Iwahashi, 2003). Taken together, these results indicate collagen crosslinking may play a large role in cervix mechanical behavior through pregnancy. The orientation of the elastic fiber band may also play a role in cervical mechanics by allowing for recoverable high strain during labor (Leppert, 1986). The biochemical causes behind cervical softening remain poorly quantified, although thromobospondin-2 deficiency has been implicated in premature softening of the cervix in murine models (Kokenyesi, 2004). Prostaglandins and antiprogestins like RU486 were found to inducing symptoms of cervical ripening in rats, including increased strength, extensibility, and plasticity (Buhimschi, 2004)

Mechanical tests have verified that pregnant cervical tissue is more compliant and possesses a less connected collagen network (Myers, 2008). Interestingly, another study using a murine model found that cervical elastic stiffness unexpectedly increased through pregnancy, possibly to adapt to increasing stress from the fetus or due to reduced fluid movement in the tissue (Barone, 2012). Similar to pregnancy-related mechanisms behind increasing uterine compliance, collagen degradation through MMP-9 and immune-mediated inflammatory response may contribute to cervical remodeling; such systems may be prematurely activated and instigate preterm birth (Gonzalez, 2011). Collegenase content was seen to increase alongside possible neutrophil infiltration during labor and cervical ripening, further supporting the hypothesis of immune-mediated cervical

remodeling (Rechberger, 1993). Specifically, Interleukin-8 has been demonstrated to be significantly elevated in the cervix after parturition and throughout pregnancy (Word, 2007).

Premature cervical remodeling may increase the likelihood of preterm labor but is poorly understood. It is hypothesized that a weakened cervix may fail to hold the fetus to full term. Interestingly, uniaxial tests indicate cervical insufficiency may not be due to decreased collagen content or weaker fibers (Oxlund, 2010). Measurements of non-pregnant women with diagnosed cervical insufficiency revealed abnormal decreased cross-linked collagen content, such that might occur during pregnancy with cervical softening (Schlembach, 2009). There remains a need to delineate structure-function relationships within cervical tissue to deduce the extent to which cervical insufficiency is governed by remodeling of structural constituents.

B4. RELEVANCE OF BIAXIAL TESTING

The passive mechanical properties of the uterus are not well understood, but are integral to understanding the stretch-mediated response in gravid uterine horns. Although constituent composition and changes have been well-characterized by histology and PCR analysis, their effect on uterine mechanical properties have not yet been robustly established. Similarly, although indentation (Yao, 2014; Myers, 2008; Barone, 2012) and uniaxial mechanical tests (Oxlund, 2010; Myers, 2008; Yoshida, 2014; Petersen, 1991; Kokenyesi, 2004; Buhimschi, 2004) have been performed on the cervix, cervix mechanical behavior has likewise yet to be vigorously quantified, making the exact biomechanical causes of cervical insufficiency and cervix-related preterm birth unclear. Uniaxial tests on the cervix have suggested region specific differences where the internal os is more compliant than the external os (Myers, 2008).

To elucidate these properties, biaxial testing can be used in physiologically relevant experimental protocols. By measuring along two axes, the material can be represented as a three-dimensional entity in constitutive relations. Anisotropy and axial coupling can also be accounted for since tension can be induced in multiple directions. In the field of biomechanics, both uniaxial and biaxial testing has been successfully applied to other tissues, such as skin, tendon (Stäubli, 1999), pericardium (Waldman and Lee, 2002), vasculature (Vande Geest, 2006), and myocardial tissue (Gupta, 1994). Uniaxial testing of cervical tissue has been described in previous sections of this chapter. Manoogian performed a dynamic biaxial study on porcine uteri but with forces replicating those seen in a car crash, reporting failure stresses and evidence of nonlinear behavior (Manoogian, 2012). Quasi-static uniaxial tests showed uterine tissue to have significant viscoelastic properties, exhibiting hysteresis during cyclic loading (Omari, 2015). Further, uniaxial mechanical tests showed that pregnant uterine tissue is significantly less stiff than nonpregnant tissue (Conrad, 1966). Additionally, later quasi-static uniaxial tests found evidence that the outer myometrium was stiffer than the inner myometrium under tensile loading, possibly attributable to variation in fiber or muscle orientation (Pearsall and Roberts, 1978). Recent uniaxial tests comparing uterine tissue between Antxr2 -/- mice, which have increased collagen levels, and control Antxr2 +/+ mice revealed poorly remodeled, collagen-rich uterine tissue is significantly stiffer and less distensible than normal tissue, which could interfere with normal parturition (Mondragon, 2017). Compression testing has previously also been chosen due to ease of preparation and running of experiments, but tension testing, especially planar biaxial testing, may provide more physiologically relevant results (Mahmoud, 2013). To date, however, quasi-static

biaxial tests of uterine tissue at physiological loading and strain ranges have not yet been undertaken; such tests are needed to quantify passive uterine mechanical properties and response to mechanical stimuli.

C. METHODS DEVELOPMENT

C1. MECHANICAL TESTING

The internal os, external os, and uterus will be removed from sacrificed C57BL/6/F mice (IACUC approved, Tulane University) per the protocol detailed in Appendix K. An axial cut will be made along the ventral aspect of the tubular cervix and uterus and the organs will be "unrolled" into a planar configuration. If testing does not occur immediately, samples will be frozen in an HBSS soaked KimWipe (Kimberly-Clark, Irving, TX). The location at which the sample was taken, orientation of the tissue (circumferential and longitudinal), the side the samples were cut, and mouse information will be recorded. Prior to testing, tissue will be thawed to ambient temperature and undertake biaxial experimental protocol within nine hours; previously frozen and thawed reproductive tissue does not appear to affect mechanical properties (Rubod, 2007).

Sample dimensions including thickness will be measured with digital calipers with 0.01 mm precision. If samples are too thick, they will be frozen and then sectioned into thinner slices (Myers, 2008). Samples will then be stamped into a cruciform shape and gripped as described in Chapter 3 for skin samples. Briefly, the samples will be aligned so that circumferential and longitudinal fiber directions align with the principal orthogonal testing axes, cut into the cruciform shape to ensure optimal load transfer to the region of analysis, and gripped with sandpaper and clamps. To satisfy St. Venant's principle, only 1 mm of each arm will be glued to each sandpaper tab, which was previously found to be enough for gripping (Szczesny, 2012). For tracking markers, poppy seeds will be placed

at each corner on the central region, assuming a homogeneous strain field. A syringe exerting a small amount of suction will be used to precisely place the poppy seeds. Tissues will bathe in HBSS solution throughout testing at ambient temperature. Gripping protocol is fully described in Appendix L.

Unloaded reference configuration will be found experimentally through axial displacement until the tissue is parallel to the camera plane while minimizing tensile load. Previous tests on cervix and uterus have suggested 0.5 – 1 g is sufficient (Myers, 2008; Manoogian, 2012). To quantify anisotropy, constant stretch and equibiaxial tests will be performed with the following stretch ratios $E_{\theta\theta}$: E_{LL} = 1:1, 1:0.75, 1:0.75, 1:1, 1:0.5, 0.5:1, 1:1 (Vande Geest, 2006). The use of multiple stretch ratios ensures mechanical response over a wide strain domain is captured (Sun, 2003; Sacks and Chuong, 1998). Equibiaxial results will be compared to ensure tissue is not damaged during tests (Vande Geest, 2006). To ensure convergence of results, each sample will experience 10 cycles of preconditioning for each testing ratio as described in Chapter 3. Preconditioning cycles are only effective for their individual tension test, and samples must be newly preconditioned if the testing parameters change (Fung, 1993). Data from the tenth loading-unloading cycle will be used to describe experimental results. Displacement rate will be 0.2%/sec, comparable to previous uniaxial loading rates of human cervix (Myers, 2008) and uterus (Pearsall and Roberts, 1978). Failure properties will not be formally measured; thus, maximum strain will be kept relatively conservative between 10 – 15% (Myers, 2008; Mondragon, 2013).

C2. HISTOLOGY

Remaining tissue samples left from the stamping process will be embedded in paraffin and undergo histomorphometric analyses to quantify collagen, elastin, and smooth muscle content. Specifically, staining with Picrosirius red, Movat's Pentachrome, and

Verhoeff-van Gieson will make known collagen, smooth muscle, and elastin content respectively, which will be quantified with image processing and analysis. Custom scripts developed in MatLab will be used to quantify collagen and elastin network organization.

C3. STRUCTURE-FUNCTION RELATIONSHIPS

Using a custom MatLab script, the deformation gradient calculated during biaxial testing will be converted into Green strain and the right Cauchy-Green strain tensor. Tension loads measured by the orthogonal load cells will be converted into Cauchy principal stresses. Bilinear fitting will be used to create stress-strain curves describing uterine and cervical tissues and allowing calculation of linearized stiffness. Data will also be used to describe ultimate tensile strength of tissue. Although assumed negligible, shear stresses may present issues with accurate principal stress measurement and decrease model fits (Sun, 2003). As previously described, experimental stress and strain can be fit to a microstructurally-motivated constitutive model informed to known structural organization of collagen, elastin, and smooth muscle. A four-fiber family model will be used to fit stress-strain to material parameters, as proposed by Baek (2007) and utilized for vascular modeling (Gleason, 2008; Lee, 2013). The four-fiber family model is written:

$$W = \frac{c_1}{2}(I_1 - 3) + \sum_{k=1}^{4} \frac{c_2^k}{4c_3^k}\{\exp[c_3^k((\lambda^k)^2 - 1)^2 - 1\}$$

Where c_1, c_i^k are material parameters and I_1 is the first invariant of the right Cauchy-Green tensor (Sack and Sun, 2003):

$$I_1 = tr\boldsymbol{C} = \lambda_1^2 + \lambda_2^2 + \lambda_3^2$$

λ^k is the fourth invariant IV_c where:

$$IV_c^k = \lambda_1^2 \sin^2 \alpha^k + \lambda_2^2 \cos^2 \alpha^k$$

Where α^k is the orientation of each fiber family; hence the fourth invariant describes the overall strain oriented to each family. It should be noted that the *k* terms are not exponents but rather a notation that delineates the material parameter profile of the current fiber family. The first term in the strain energy function is the neo-Hookean meant to describe the linear isotropic elastin-dominated ground matrix (Holzapfel, 2000). The second describes the exponential strain energy function of each fiber family: circumferential, longitudinal, and two diagonal. The sum of the individual strain energy functions, including the neo-Hookean, is the overall strain energy function of the tissue. The Marquardt-Levenberg algorithm will be used to perform multivariate nonlinear regression to fit the model to experimental data. Goodness of fit, over- or under-parameterization, and correspondence with histological findings will be evaluated to determine the applicability of the model to uterine and cervical tissue.

C4. STATISTICS

ANOVA will be used to evaluate overall significant difference in output parameters corresponding to microstructure from the constitutive model of the inner os, outer os, and uterine wall. Tukey's post-hoc tests will be used to evaluate individual pair differences between experimental groups.

D. DISCUSSION

Experimental methodology was developed to biaxially test uterine and cervical tissue to quantify mechanical differences between both. Previous literature has shown that collagen fibers have preferred alignments in both the cervix and uterus and thus show pronounced anisotropy. Biaxial testing protocols were developed to measure the complex behavior of these tissues based on methods developed in Chapter 3. Pilot studies must be conducted to determine optimal testing parameters, such as maximum stretch, stretch rate,

and reference configuration. During pregnancy, dramatic remodeling occurs within the uterus and cervix that allow increased maximum distension and dilation to accommodate and deliver the fetus. In the uterus, it has been posited that changes in SMC phenotype and ECM remodeling is due to a combination of inflammatory, hormonal, and mechanical stimuli. In the cervix, similar EMC changes associated with remodeling of collagen and elastic fibers are thought to play a role in cervical softening, ripening, and dilation. The exact structure-function relationships in both uterine and cervical tissue, however, remain unclear as does how mechanical dysfunction in each relates to preterm birth. Histological data can be used to quantify constituent presence in uterine and cervical tissue and inform structure-function relationships that describe mechanical response. Constitutive modeling was explored as a method to derive the contributions of individual constituents to tissue mechanical properties, which may be different between the cervix and uterus. The four-fiber family model has been proven to robustly describe the behavior of arteries and may fit data from the tubular components of the genital tract. R^2 values could be used to determine the goodness of fit to experimental data, although it should be noted that with an unlimited number of terms, any experimental data can be fit. Hence it is important to not overparameterize a model to maintain maximum relevancy to physiology. It remains to be elucidated what the ideal model for uterine and cervical tissue is. Eventually, modeling and experimental data could be used to deduce microstructural differences between healthy and diseased tissue, how mechanical stretch affects each, and, finally, how preterm birth may occur from a biomechanical perspective.

4.2. FUTURE DIRECTIONS: MECHANICAL TESTING OF UTEROSACRAL LIGAMENT AND VAGINAL TISSUE

A. INTRODUCTION

Pelvic organ (urogenital) prolapse (abbreviated POP) is a common medical condition that causes the pelvic viscera, such as the bladder or uterus, to descend. The vagina and uterus can protrude from the body as a result, which can cause a variety of uncomfortable symptoms affecting the lower body. About 41% of women from ages 50-79 have some symptoms of prolapse, although prolapse can often be asymptomatic. Many women elect to have surgery to correct the prolapse; in the United Kingdom, 20% of gynecological surgeries are for pelvic prolapse (Jelovsek, 2007). In the United States, a woman has a significant 11% probability of having surgery for prolapse or urinary incontinence, representing an extreme case where prolapse is considered severe enough to merit surgical intervention (Weber and Richter, 2005). Women suffering from prolapse exhibit from symptoms spanning pelvic pressure, urinary incontinence, urethral obstruction, difficulty with defecation, and sexual dysfunction (Weber and Richter, 2005). Transvaginal meshes are often used to treat POP, but serious complications from erosion and exposure can arise, necessitating reoperation (Margulies, 2008). Reoperation rate was found to be nearly 30%, with successive repairs decreasing the time between reoperations (Olsen, 1997).

Despite its widespread prevalence and obvious effect on women's quality of life, little is definitively known about the underlying causes of pelvic organ prolapse. There are also no real preventative measures that can be taken until end-stage surgery. Many risk factors may contribute to POP development, including obesity (Giri, 2017), age (Nygaard, 2004), ethnicity (Hendrix, 2002), family or work history (Chiaffarino, 1999), and parity

(Hendrix, 2002; Mant, 1997). First, vaginal birth is the largest contributor to POP etiology, with each subsequent birth further contributing to a lesser extent (Mant, 1997). This suggests permanent changes occur in vaginal tissue during pregnancy and labor. Diseases that negatively affect connective tissue, such as Marfan syndrome (elastin) or Ehlers-Danlos syndrome (collagen), have been known to contribute to developing symptoms (Word, 2009, Lammers, 2011, Carley and Schaffer, 2000), although pelvic connective tissue deficiency can still be locally manifested in otherwise healthy women (Epstein, 2007).

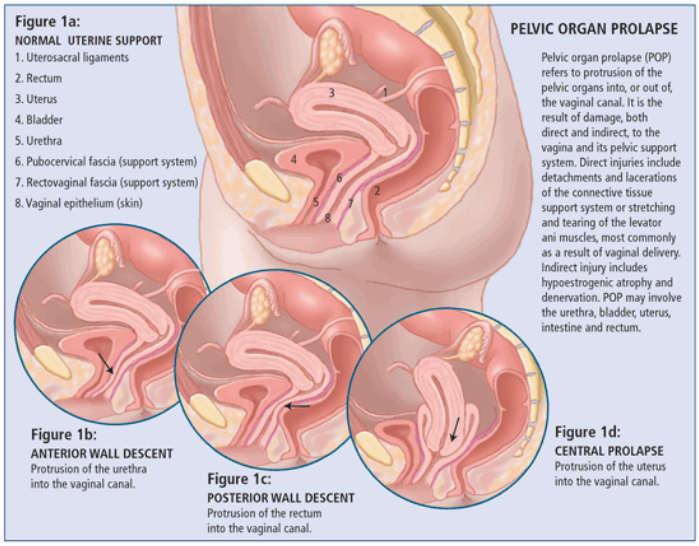

Figure 29: Overview of pelvic organ prolapse, courtesy of healthplexus.net

During pregnancy, the vagina undergoes significant remodeling. The vagina must be able to distend remarkably in order to accommodate the passage of the baby; it must then also be able to return back to its normal non-birthing state. Murine studies found that vaginal tissues in mice with pelvic prolapse were similar to those in pregnant mice (Rahn, 2008). Biomechanical test results from pregnant mice show greater deformation when subject to mechanical stress and also greater distension before failure (Rahn, 2008). Failure strain for both pregnant and prolapsed mice was twice the failure strain for non-pregnant mice (Rahn 2008).

In the field of biomechanics, it is understood that the mechanical properties of tissue are related to the composition of the tissue. Collagen, the main structural fiber of the body,

and elastin are present in both connective tissue and reproductive tissue. Although POP etiology is likely multifactorial, several risk factors seem to indicate that mechanical forces play a role in symptom manifestation. Parturition (Mant, 1997), obesity (Giri, 2017), and repetitive strenuous labor (Chiaffarino, 1999) are all known risk factors of POP development and place significant mechanical load and stretch on the pelvic region. There thus remains a need to delineate structure-function relationships in the vagina and its supporting uterosacral ligaments and, further, to correlate such relationships with known risk factors. We hypothesize that elastic fiber disruption is a contributor to POP induction and maladaptive remodeling of collagen and smooth muscle content in vaginal tissue. The overall effect is decreased integrity of the vaginal wall, leading to mechanical dysfunction. Through investigations of prolapsed and non-prolapsed tissue, we will deduce elastic fiber-oriented mechanobiological differences by evaluating vaginal structure-function relationships via mechanical testing and quantitative histology. Understanding vaginal material properties can facilitate the development of more effective treatments yielding less complications. The objective of this chapter is to develop an experimental protocol for determining elastin's contribution to vagina and USL function.

B. BACKGROUND

B1. VAGINAL ANATOMY AND CONSTITUENTS

The vagina is the most inferior aspect of the female reproductive tract. The external os of the uterine cervix opens into the vaginal fornix (Moore, 2015). The vagina is composed of four layers: the stratified squamous epithelium, subepithelium, muscularis, and adventitia, with the latter three layers often folded during POP intervention surgery (Moalli, 2005). The muscularis is composed of mainly smooth muscle and the adventitia of loose connective tissue. In the subepithelium, the layer that contributes most to vaginal

load-bearing structure (Abramowitch, 2009), collagen type III appears to be the predominant fibrillar collagen over collagen type I and the primary constituent, arranged in a whorled pattern (Moalli, 2005). In the muscularis, smooth muscle cells are arranged in circumferential and longitudinal directions coupled with dense collagen (Badiou, 2008). Elastin is also present in the vaginal wall as a network of long and straight fibers that bond the adventitia and levator ani (Drewes, 2007). Minor constituents include glycoproteins, hyaluronan, proteoglycans, and collagen type V (Ambramowitch, 2009). In pregnant murine models, maximum strain was found to increase to 24% from 14% and muscle contractility was found to decrease significantly (Feola, 2011), demonstrating that great distensibility is possible in vaginal tissue during labor. During pregnancy, the vagina undergoes substantial remodeling to accommodate the passage of the fetus. Notably, in parous mice, elastic fibers because more tortuous, possibly contributing to observed stiffness decrease (Downing, 2014). Additionally, multiparous mice exhibit more tortuous fibers after recovery compared to virgin mice, indicating long-term damage due to the trauma of pregnancy may have occurred (Downing, 2014).

B2. PELVIC SUPPORT LIGAMENTS

The uterus, cervix, and vagina are supported by the pelvic floor, a grouping of muscles and connective tissue, including the endopelvic fascia and the levator ani muscle (Ashton-Miller, 2001). The uterosacral ligament (USL), coupled with the cardinal ligament (CL), originates from the sacral vertebrae and terminates above the internal os and proximal vagina, providing support to the pelvic organs (Buller, 2001). The CL originates at the lateral pelvic wall and terminates at the fornix of the vagina and cervix (Moore, 2015). The main constituents of ligaments are collagen type I/III and elastin (Goh, 2003). In the CL, composition is mainly collagen type I fibers, densely and regularly

packed (Salman, 2010), coupled with elastin fibers (Ewies, 2003). The USL is thought to have significant SMC content (>20%) mixed with moderately aligned collagen (predominantly type III) fibers (Gabriel, 2005) and greater elastin fiber content than the CL (Tan, 2015). In swine CL and USL, collagen fibers are predominantly aligned axially, with CL bundles less densely arranged than USL bundles (Tan, 2015). Ligament support of the vagina is also known as Level I support, where Level II support is the arcus tendineous fasciae pelvis and Level III support is the perineal membrane (Abramowitch, 2009).

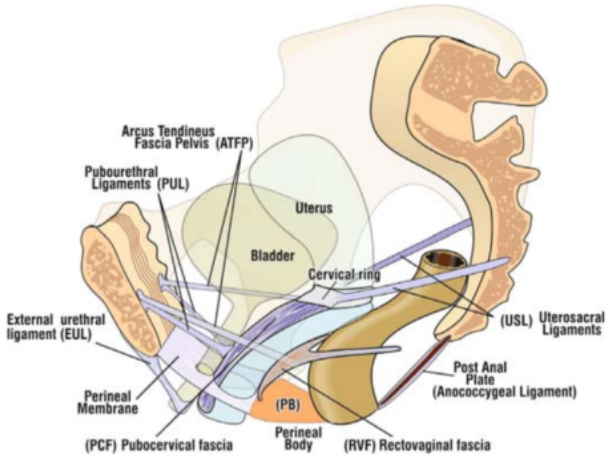

Figure 30: Illustration of pelvic organs and supporting connective tissue (Petros, 2007)

B3. STRUCTURE-FUNCTION CHANGES DUE TO PELVIC ORGAN PROLAPSE

Development of POP was found to correlate with a negative change in collagen type I:III ratio for the CL and lower elastin expression (Ewies, 2003). Additionally, qualitative light microscopy revealed collagen fibers to be larger and less dense than non-POP tissue (Salman, 2010). Immunohistochemistry assays found similarly elevated collagen type III content but relatively unchanged collagen type I content in the USL for women with POP, suggesting that collagen type changes lead to modified tissue extensibility and stiffness (Gabriel, 2005). The replacement of mature, strong collagen fibers with newly deposited collagen fibers has been postulated as the cause of decreased ligament (Word, 2009) and vaginal (Jackson, 1996) strength and integrity. A less invasive

POP surgical treatment has been developed than involves reinforcing the USL with a polypropylene sling to restore function (Petros, 2007).

Other studies, however, found that collagen type III content decreased (Zhou, 2012; Lin, 2005) while stiffness increased in the vaginal wall in POP subjects (Zhou, 2012), delineating behavior different from pelvic ligaments; but these findings contradict findings that collagen type III content increases in women with POP (Moalli, 2005), which correlates with ligament changes. In prolapsed cervical tissue, it was found that collagen type III content decreases (Iwahashi, 2010). Although results are somewhat contradictory, prolapsed vaginal tissue may follow this trend as well. Additionally, in post-menopausal women, fiber preferred direction appeared to change from one preferred direction to two (Ruiz-Zapata, 2016).

Fibulin-5 knockout mice (Fbln5-/-) lack the capacity to create fibulin-5, a protein required for elastic fiber synthesis, and were found to be highly susceptible to accelerated POP development due to a lack of integrity in vaginal tissue, level II support, and level I (USL) support (Drewes, 2007; Rahn, 2008). Elastase digestion of the posterior vaginal wall was found to induce POP comparable to Fbln5-/- mice (Drewes, 2007). It has been suggested that continuous elastin turnover, unique to the vagina, allows the dramatic remodeling that occurs during parturition; thus, disruption of elastin synthesis after pregnancy may cause a loss of vaginal integrity (Budatha, 2011; Drewes, 2007; Rahn, 2008). Fibulin-5 may also downregulate connective tissue degradation by MMP-9 and MMP-2 metalloproteases, which were observed to be upregulated in human POP subjects (Budatha, 2011; Moalli, 2005; Zong, 2010; Jackson, 1996). Human studies suggested that decreased elastin production with uninhibited turnover could lead to thinning and stiffening

of elastic fibers and induction of POP (Chen, 2004). Similarly, POP has also been associated with decreased smooth muscle fractional count, disorganization, and replacement with fibroblasts which synthesize abnormal collagen, changing vaginal wall mechanical properties (Badiou, 2008). Rapid elastin turnover may occur in POP partly due to the mechanical stresses associated with prolapse and the need to adapt to changes in the loading environment and hormonal influences (Zong, 2010).

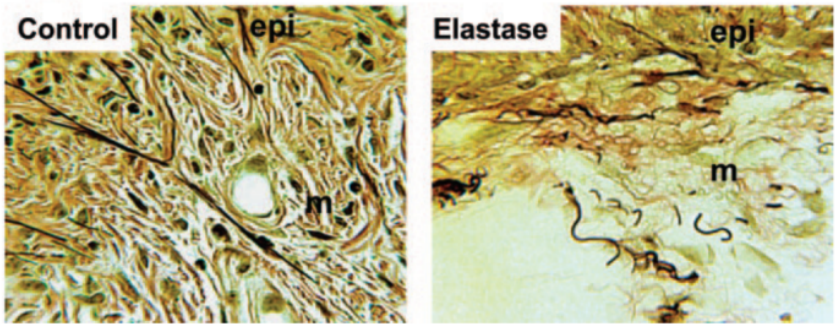

Figure 31: Mice vaginal walls subject to elastase showed disrupted elastin fibers and developed POP (Drewes, 2007)

B4. MECHANICAL TESTING

In previous studies, uniaxial tests performed on healthy USL and CL swine ligament observed greater stiffness in USL ligaments than in CL ligaments as well as nonlinear behavior (Tan, 2015). Uniaxial tests have also been performed on ewe vaginal tissue, showing decreased stiffness in parous tissue (Knight, 2016). With prolapsed vaginal tissue, however, uniaxial tests show apparent increase in stiffness compared to healthy tissue (Zhou, 2012; Lei, 2007), results which indentation tests have further reinforced (Ruiz-Zapata, 2016). Planar biaxial tests are needed to account for axial coupling and anisotropy in vaginal tissue (Abramowitch, 2009). Previous results from studies on vaginal elastic fiber structure and function indicate a need to couple mechanobiological changes in vaginal tissue with POP etiology.

Several studies have performed mechanical tests on vaginal tissue in uniaxial (Knight, 2016; Rubod, 2007; Rahn, 2008; Lei, 2007; Feola, 2011; Martins, 2010) and biaxial (Barone, 2015) testing configurations. The USL and CL have also been tested uniaxially (Tan, 2015) and biaxially (Becker and De Vita, 2015). Nevertheless, it is necessary to more robustly characterize the mechanical properties of vaginal tissue and USL/CL ligaments, especially in biaxial tests, and further to test human tissue and correlate changes in structure and function with POP development and predisposition.

C. METHODS DEVELOPMENT

C1. SAMPLE HARVESTING

Prolapsed and healthy vaginal and USL tissue have been obtained from routine hysterectomies from both healthy and prolapsed women over 18 years of age. No other information will be known during testing to ensure a blind study. Other relevant indices, including POP risk factors, will be processed by the Department of Epidemiology and the School of Public Health at Tulane University to later be correlated with biaxial data. Samples are cryoprotected in HBSS and stored at -80 ^{o}C at the Oschner BioBank (New Orleans, LA) and will be transported to the testing lab in a cooler. Care will be taken to ensure that samples thaw as little as possible during transportation. It has been previously shown that previous frozen samples do not exhibit significantly different mechanical properties (Rubod, 2007). The dimensions and orientation of each sample are recorded during extraction.

N	Group	Inclusion criteria	Exclusion criteria
22-23	Prolapse	Females, ≥ 18years old, symptomatic prolapse at least stage 2 in one compartment, undergoing hysterectomy	Male Cancerous tissue Connective tissue disorder < 18 years old Previous surgery for pelvic floor disorder
22-23	Control (Non Prolapse)	Females, ≥ 18years old, no symptoms or evidence of prolapse > stage 2 on exam, undergoing hysterectomy	Male Cancerous tissue Connective tissue disorder < 18 years old symptomatic prolapse at least stage 2 in one compartment Previous surgery for pelvic floor disorder

Table 3: Inclusion and exclusion criteria for patients

Sample	Weight (mg)	Length/*Diameter* (mm)	Width/*Thickness* (mm)
Left USL	400	8.5	8.5
Right USL	500	9.5	9.5
Vagina	390	20	6.5
Cervix	2390	*20.5*	*6.5*

Table 4: Representative sample of tissues extracted from hysterectomies

C2. MECHANICAL TESTING

Tissue specimens will be allowed to thaw to ambient temperature in HBSS before mechanical testing and remain in a HBSS bath throughout testing. Samples will be stamped into a cruciform shape with sample circumferential and longitudinal axes aligned with the cruciform arms, and tissue thickness will be measured with calipers. Remaining tissue after stamping will be reserved for histological studies. Sandpaper will be affixed to each arm using a small amount of cyanoacrylate, and the sandpaper-tissue composite will be clamped using custom-designed grips as described in Chapters 3 and 4. A full

description of the gripping protocol may be found in Appendix L. India ink or poppy seeds will be used to apply four black markers to be used for optical strain tracking.

Tissue reference configuration will be defined as the zero-strain configuration after which it is preloaded to lay flat to the camera plane per Chapter 4. After reference is set, samples will undergo 10 cycles of preconditioning for each testing protocol as described in Chapter 3 and 4. Data from the tenth loading-unloading cycle will be used to ensure results are repeatable. Samples will undergo a wide range of equibiaxial and constant stretch tests to fully characterize anisotropy. Samples will be tested with the following stretch ratios $E_{\theta\theta}$: E_{LL} = 1:1, 0.75:1, 1:0.75, 1:1, 0.5:1, 1:0.5, 1:1 (Vande Geest, 2006). In-plane loads and optical strain will be measured throughout testing. Equibiaxial tests are used at different testing points and results checked for consistency to ensure tissue is not damaged after constant stretch tests (Vande Geest, 2006). Loading rate will be 0.2%, similar to rates chosen in vaginal (Rubod, 2007) and USL (Becker and Vita, 2015) mechanical studies. To prevent tissue failure that may corrupt histological findings, maximum strain will be kept conservatively to 10 – 15%. Following mechanical testing, samples will be subject to elastase digestion and re-equilibrated in HBSS, as previously demonstrated in our lab (Morris, 2016; Robison, 2016). Samples will then be retested following the same protocols as the first stage to determine elastin contribution to vagina and USL mechanical behavior.

C3. HISTOLOGY

Reserved tissue from stamping and post-elastase tissue will be embedded in paraffin and undergo histological analysis at the Tulane Histology Core Facility. Picrosirius Red, Movat's Pentachrome, and Verhoeff-van Gieson will be used to visualize collagen type I and III, GAG/SMC, and elastin content respectively. Image analysis will

be used to quantify constituent presence in terms of area fraction (Udelsman, 2014; Bersi, 2012). Elastic tortuosity (Downing, 2014) and collagen fibril crimping and geometry (Miller, 2012) will be quantified using custom MatLab scripts and image processing.

C4. STRUCTURE-FUNCTION RELATIONSHIPS

Data processing and constitutive modeling was described in Chapter 4. Briefly, the developed MatLab script will convert raw data from the biaxial device to Green strain and the left Cauchy-Green tensor. The second Piola-Kirchhoff stress tensor and Cauchy stress will also be calculated. A bilinear curve fit will be used to find tissue stiffness in the toe and linear region of the stress-strain graph. The processed data will be used to fit a four-fiber family model, programmed using MatLab, in which microstructurally-motivated parameters are related to mechanical response. Multivariate nonlinear regression will be used to find best-fit parameters.

C5. STATISTICS

Differences in parameters, linearized stiffness, and strain energy pre- and post-elastase in prolapsed and healthy tissue will be evaluated through individual t-tests. These data will also be compared across known risk factors of POP, including parity, BMI, age, and sociodemographic factors such as race, using t-tests and ANOVA. The risk factor that contributes most strongly to tissue properties will be ascertained through multivariable linear modeling.

D. DISCUSSION

Experiment design, mechanical testing protocol, and histological methods were developed to test vaginal tissue and USL from prolapsed and healthy subjects. While similar experiments have taken place on animal models, the use of human subjects confers a great advantage in physiological applicability and accuracy. We hypothesize that elastin degradation plays a part in vaginal compliance and, further, that certain factors, including

strenuous, mechanically stressful activity, may accelerate degradation and increase POP risk. An experiment was designed to isolate the contribution of elastin to vaginal wall function through mechanical testing before and after elastase digestion. Samples were harvested and preserved; methods were developed to prepare the samples for testing in optimal, physiologically-relevant conditions. Mechanical testing protocol was based on methods developed in Chapter 3 for skin tissue, although pilot studies must be run to determine optimum testing parameters for vaginal tissue and USL. Histological methods were developed to characterize constituent fractional area and geometry in order to better inform constitutive models. The end goal of this study is to create structure-function relationships that describe and predict vaginal and USL behavior in prolapsed and healthy tissue. Of interest is the mechanobiological differences between prolapsed and healthy tissue and whether prolapsed tissue post-elastase will yield significantly different properties from pre-elastase results. If this is the case, disruption of elastin synthesis may indeed significantly contribute to vaginal mechanical dysfunction. Although our hypothesis may eventually prove incorrect, a well-informed constitutive model could still be created based on experimental data that can be used to predict tissue behavior based on ECM changes.

Chapter 5. Conclusions

A. INTRODUCTION

A custom planar biaxial device optimized for mechanical testing of small soft tissues was designed and constructed. In Chapter 2, the device was divided into core systems, including motion, measurement, grips, tank, and software, each of which was individually examined to improve device compatibility with tissue testing. Motion systems, imaging systems, and electronic interfaces were comprised of standard off-the-shelf parts while machining and fabrication techniques such as 3D printing and CNC milling were used to create custom parts. Notable custom parts included clamp grips, adapters, and a tank. The device interface was programmed using LabView, and additional processing was programmed through MatLab. The process of building and programming the device was reported. Device design was improved upon to better mimic the physiological environment by redesigning, among other modules, grips, tanks, and optical tracking systems.

Image processing techniques such as particle analysis were used to track four dots on tissue assuming a homogenous strain field. The LabView interface ran strain-controlled mechanical tests, measuring local tissue deformation to more accurately describe tissue behavior. The MatLab code could re-track images using additional techniques such as texture correlation and additionally had an implementation of full-field displacement tracking. Raw data from the LabView interface, such as the deformation gradient and measured forces, were imported into the MatLab program to return strain and stress, which could then be used to inform constitutive models of soft tissue. A significant amount of

time was devoted to developing and making novel additions to software to run tissue-specific protocols and track local deformations within tissue. Biaxial device grip-to-grip displacement was validated by measuring linear displacement, while strain-field displacement was validated experimentally using murine skin, as described in Chapter 3. Skin was dissected from mice and biaxial tests were successfully run. Experimental data were compared to results found in literature to validate the accuracy of the device.

The tissue of the female reproductive tract exhibit complex behavior and have not yet been robustly quantified, especially for human tissue. In Chapter 4, methods for ascertaining the mechanical properties of uterine, cervical, vaginal, and uterosacral ligament tissue using planar biaxial testing were developed. A combination of mechanical testing, histology, and modeling were incorporated in an effort to quantify anisotropic nonlinear behavior and form a baseline for elucidating the mechanical pathogenesis of preterm birth. For uterine and cervical tissue studies, the overall hypothesis is that, in cases of cervical insufficiency or uterine overdistension, poor remodeling of the uterus and cervix may cause early labor to occur under mechanical stress and strain. For vaginal and cervical tissue, the overall hypothesis is that elastin plays a significant role in vagina and USL mechanical behavior and that decrease in elastin integrity may contribute to POP pathogenesis.

B. LIMITATIONS

As has been described in previous chapters, the planar biaxial device has several limitations. It was limited to four-point optical strain tracking, which assumed the tissue deforms homogenously. Full-field displacement was not implemented in the interface code. Additionally, clamping grips introduced undesired boundary conditions that led to less accurate results than from suturing techniques, although the use of cruciform

specimens to preserve high aspect ratio alleviated this effect. Unfortunately, due to the small size of the tissue to be tested, cruciform arm length is limited, which may cause the stress field to be more heterogeneous. In software, particle tracking methods proved to be unreliable at times. Computed positions would differ slightly even when tissue was static, introducing a significant amount of noise into experimental data at small strains.

Although biaxial testing of human reproductive tissue is a good starting point for future experiments, more tests are needed to fully characterize mechanical properties and further to delineate differences between mechanically compromised and healthy tissue. Additional experiments will need to be designed correlate mechanical behavior with preterm birth or POP etiology.

C. CONCLUSION

In this thesis, an improved planar biaxial device was created and evaluated as a method to ascertain tissue mechanical behavior, changes to which have been implicated in the underlying pathogenesis of many disorders, including pelvic organ prolapse and preterm birth. In the field of women's reproduction, there is a pressing need for advancing the current understanding of the mechanics of these disorders. Preterm birth, for instance, is a leading cause of infant mortality and disability, while pelvic organ prolapse can significantly decrease a women's quality of life. To this end, a planar device capable of testing soft tissue, including reproductive tissue, was designed, constructed, programmed, and validated. The custom planar biaxial device offers a novel evolution over commercially available devices that are often used in mechanical studies of soft tissue. The constructed device better mimics physiological conditions and facilitates more accurate experimental data by substantially improving tissue gripping, strain measurement, and testing parameters and conditions. Stress-strain data from this device could be used to

inform constitutive models which relate changes in mechanical properties with changes in biological constituents. Eventually, such data could prove invaluable for the design of patient-specific treatments and quantitative diagnoses which acknowledge microstructural differences and underlying mechanical deficiencies in soft tissue.

Appendix
CONTENTS

A1. BIAXIAL DEVICE PARTS LIST: PURCHASED PARTS

Motion Control

Company	Part Description	Quantity	Unit Price	Total Price
Advanced Micro Systems	Stepper Motor, High torque, 75ozin, Frame size 17, single shaft	4	$115.00	$460.00
	Max 420 Controllers	2	$1,419.00	$2,838.00
	USB for Controller SIN-11-USB	1	$99.00	$99.00
Thomson BSA	Linear screws X4: M17S4, M17S4-MTS 10x2M-2.0" Stroke	4	$506.35	$2,025.40
			Total	$5,422.40

Data Acquisition

Company	Part Description	Quantity	Unit Price	Total Price
Honeywell	MODEL 31, 50 gm, 60 to 160 deg. F. (15 to 70 deg.C) Temperature Compensation, Non-amplified (mv/v), Overload Stops, Submersible cable, 10 ft (3 meter) Long, Radial Electical Exit Orientation	2	$1,212.00	$2,424.00
	MODEL 34, 5lb, Temperature Compensation 60 to 160 deg. F. (15 to 70 deg.C)Temperature Compensation, Internal Amplifiers, Non-amplified (mv/v) Overload Stops, Electrical 2.00 TerminationTeflon cable, 5 ft (1.5 meter) Long Special Calibration 10 point final calibration Cable Exit Port Orientation Radial Electrical Exit Orientation Load Cells Special Load Cell Calibration Calibrate in Tension and Compression	2	$1,296.00	$2,592.00
National Instruments	NI 9237 4-Ch 50 kS/s per Channel, 24-Bit Bridge Analog Input Module	1	$1,214.00	$1,214.00
	cDAQ-9171, CompactDAQ Chassis (1 slot USB)	1	$252.00	$252.00
	RJ50 Cable for 9944, 9945, and 9949, 2m (qty 4)	1	$27.90	$27.90
	NI 9949 RJ-50 (female) to Screw Terminal Adaptor (Qty 4)	1	$172.80	$172.80
	NI 9942 4-Position Connector Kit	1	$8.10	$8.10
			Total	$4,266.80

Image Acquisition

Company	Part Description	Quantity	Unit Price	Total Price
Edmund Optics	AVT Manta G-419 1" NIR CMOS Camera	1	$2,065.50	$2,065.50
(10% university discount)	12V 12-Pin Regulated HIROSE Power Supply	1	$99.00	$99.00
	1/4 Mirror 75mmx75mm Enhanced Aluminum	1	$148.50	$148.50
	45 degree mounts: 1" Offset, 1" OD Mount, 45 Degree Mounting Adapter	2	$26.10	$52.20
	3.0" Medium Mirror Mount	1	$121.50	$121.50
Navitar Inc.	6.5X Zoom Body 1-6232	1	$917.00	$917.00
(10% university discount)	1X Short Tube Adapter 1-6245	1	$350.00	$350.00
	C-Mount Coupler:1-6010	1	$56.00	$56.00
	Right Angle Lens Attachment:1-62866	1	$491.00	$491.00
	0.75X Lens Attachment:1-60111	1	$170.00	$170.00
	Universal Mounting Clamp:1-6270	1	$137.00	$137.00
	150W Halogen Light Supply: 8-61172	1	$520.00	$520.00
	Fiberoptic Ring Light:1-61214	1	$473.00	$473.00
Newport Corporation	1D Linear Stage X3: TSX-1D, Dovetail Linear Stage, 1.0 inch travel, 1/4-20	3	$149.94	$449.82
	Rod Clamp: 340-RC	1	$69.94	$69.94
ThorLabs	Kinematic Base: 3" x 3" (75mm x 75mm)	1	$90.40	$90.40
	Mounting Post Base 2.48x0.4	1	$23.70	$23.70
	Mounting Post, 1/4"-20 taps	1	$38.00	$38.00
			Total	$6,272.56

A2. BIAXIAL DEVICE PARTS LIST: RAW MATERIALS AND MISC. PARTS

Custom Fabrication

Company	Part Description	Quantity	Unit Price	Total Price
Jameco	Weller WES51 Analog Soldering Station Power Unit Soldering Pencil Stand Sponge	1	$134.95	$134.95
	1 Pound Solder Roll Sn60 Pb40 0.031 Inch Diameter	1	$32.95	$32.95
	High Vacuum Manual Desolder Pump	1	$8.95	$8.95
	Hookup Wire 1 Conductor 26AWG Gray Stranded PVC 300 Volt UL1007/UL1569	1	$6.75	$6.75
	Solder Spool Stand	1	$12.95	$12.95
McMaster Carr	General Purpose Tap, Through Hole (Plug), 6-32 Thread Size	2	$4.65	$9.30
	General Purpose Tap, Through Hole (Plug), 8-32 Thread Size	2	$4.83	$9.66
	General Purpose Tap, Through Hole (Plug), 10-32 Thread Size	2	$4.96	$9.92
	Sliding Machine-Mount T-Handle Tap Wrench for Number 0 to 1/4" OR 1.6 mm to 6.3mm tap sizes	1	$17.92	$17.92
	Type 316 Stainless Steel Flat Head Slotted Machine Screw, 1/4"-20 Thread, 1/2 Length, pack of 25	1	$10.00	$10.00
	Zinc Plated Alloy Steel Socket Head Cap Screw, 1/4"-20 Thread, 3/8" Length, pack of 25	1	$6.47	$6.47
	Nonmarring Flat Point Socket Set Screw, Type 316 Stainless Steel, 6-32 Thread, 3/8"Long, pack of 10	3	$4.65	$13.95
	Type 316 Stainless Steel Head Cap Screw, 8-32 Thread, 1/2" Length, pack of 25	1	$3.23	$3.23
	Type 316 Stainless Steel Socket Head Cap Screw, 8-32 Thread, 5/8" Length, packs of 25	1	$3.55	$3.55
	Type 18-8 Stainless Steel Hex Nut with Tooth Washer, 8-32 Thread Size, 11/32" Nut Width, 11/64" Overall Height, packs of 100	1	$8.61	$8.61
	Slotted Disc Flexible Shaft Coupling, Set Screw Hub, 5/8" Overall Length	4	$10.54	$42.16
	Miniature 12L14 Drive Steel Shaft, 3/16" OD, 3" Length	8	$3.13	25.04
	Pan Head Thread-Forming Screw for Sheet Metal, Zinc-Plated Steel, M3 Thread, 4mm Length	1	$10.50	$10.50
	Black Oxide Inch Hex L Key Set, Standard, 11 Piece .050"-3/8", Vinyl Pouch	1	$7.00	$7.00
	Optically Clear Cast Acrylic Sheet, 5/16" Thick, 24" x 24"	1	$58.79	$58.79
	Glass-Filled Black Polycarbonate Sheet, 2" Thick, 12" Width x 12" Length	1	$463.81	$463.81
			Total	$896.46

Miscellaneous

Company	Part Description	Quantity	Unit Price	Total Price
Dell Computer	Optiplex 7020			
Electro Industries	DC power supply 303DM	1	$329.00	$329.00
			Total	$329.00

B1. LOAD CELL SPEC SHEET (5 lb. load cell, Honeywell)

Model 34

PERFORMANCE SPECIFICATIONS

Characteristic	Measure
Load ranges[6]	1000 g, 5 lb, 10 lb, 25 lb, 50 lb, 100 lb, 250 lb, 500 lb, 1000 lb
Linearity 1000 g to 250 lb	±0.15 % full scale
Linearity 500 lb to 1000 lb	±0.2 % full scale
Hysteresis 1000 g to 250 lb	±0.15 % full scale
Hysteresis 500 lb to 1000 lb	±0.2 % full scale
Non-repeatability 1000 g	±0.1 % full scale
Non-repeatability 5 lb to 1000 lb	±0.05 % full scale
Tolerance on output 1000 g	1.5 mV/V (nominal)
Tolerance on output 5 lb to 1000 lb	2 mV/V
Operation	Tension/compression[3]
Resolution	Infinite

ENVIRONMENTAL SPECIFICATIONS

Characteristic	Measure
Temperature, operating	-53 °C to 121 °C [-65 °F to 250 °F]
Temperature, compensated	15 °C to 71 °C [60 °F to 160 °F]
Storage temperature	-73 °C to 148 °C [-100 °F to 300 °F]
Temperature effect, zero	0.005 % full scale/°F
Temperature effect, span	0.005 % full scale/°F

ELECTRICAL SPECIFICATIONS

Characteristic	Measure
Strain gage type	Bonded foil
Excitation (calibration) 1 kg to 10 lb	5 Vdc
Excitation (calibration) 25 lb to 1000 lb	10 Vdc
Insulation resistance	5000 Mohm @ 50 Vdc
Bridge resistance	350 ohm
Electrical termination (std) 1000 g to 10 lb	Teflon cable (1524 mm [5 ft]) with balance board
Electrical termination (std) 25 lb to 1000 lb	Teflon cable (1524 mm [5 ft])

MECHANICAL SPECIFICATIONS

Characteristic	Measure
Maximum allowable load	150 % FS[1]
Weight	See table
Material	17-4 PH stainless steel
Deflection full scale	See table
Natural frequency	See table

RANGE CODES

Range codes	Range
AR	1000 g
AT	5 lb
AV	10 lb
BL	25 lb
BN	50 lb
BR	100 lb
CN	250 lb
CR	500 lb
CV	1000 lb

WIRING CODES

Cable	Unamplified
Red	(+) excitation
Black	(-) excitation
Green	(-) output
White	(+) output

DEFLECTIONS AND RINGING FREQUENCIES

Capacity (lb)	Deflection at full scale (in)	Ringing frequency (Hz)	Weight (g)
1000 g to 10 lb	0,03 mm [0.001 in]	1000 Hz	40 g [0.09 lb]
25 lb to 100 lb	0,03 mm [0.001 in]	3000 Hz	80 g [0.18 lb]
250 lb to 1000 lb	0,05 mm [0.0015 in]	5000 Hz	100 g [0.22 lb]

B2. LOAD CELL SPEC SHEET (cont'd, 5 lb. load cell, Honeywell)

Honeywell

Precision Miniature Load Cell

MOUNTING DIMENSIONS

Ranges	D mm [in]	H mm [in]	A mm [in]	B mm [in]	C mm [in]	F mm [in]	G mm [in]	T
1000 g, 5 lb, 10 lb	19,05 [0.75]	44,45 [1.75]	7,87 [0.31]	4,83 [0.19]	4,83 [0.46]	15,24 [0.60]	18,29 [0.72]	1/4-28 UNF
25 lb, 50 lb, 100 lb	25,4 [1.00]	44,45 [1.75]	12,7 [0.50]	6,35 [0.25]	4,83 [0.46]	13,21 [0.52]	18,29 [0.72]	1/4-28 UNF
250 lb, 500 lb, 1000 lb	25,4 [1.00]	50,8 [2.00]	12,7 [0.50]	6,35 [0.25]	4,83 [0.46]	19,05 [0.75]	19,05 [0.75]	1/4-28 UNF

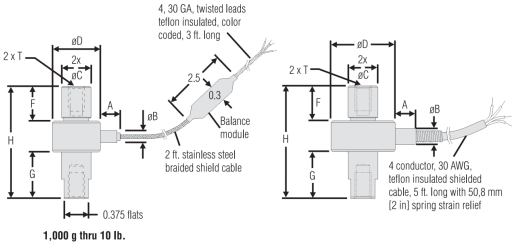

1,000 g thru 10 lb.

OPTION CODES

	Many range/option combinations are available in our quick-ship and fast-track manufacture programs. Please see http://sensing.honeywell.com/TMsensor-ship for updated listings.
Load range	1000 g, 5 lb, 10 lb, 25 lb, 50 lb, 100 lb, 250 lb, 500 lb, 1000 lb
Temperature compensation	1a. 60 °F to 160 °F 1b. 30 °F to 130 °F 1c. 0 °F to 185 °F 1d. -20 °F to 130 °F 1e. -20 °F to 200 °F 1j. 0 °C to 50 °C 1k. -20 °C to 85 °C 1m. -25 ° to 110 °C[7] 1f. 70 °F to 250 °F 1g. 70 °F to 325 °F[7] 1h. 70 °F to 400 °F[7] 1i. -65 °F to 250 °F[7]
Internal amplifiers	2u. Unamplified, mV/V output
Overload stops	4a. Overload stops
Electrical termination	6a. Bendix PTIH-10-6P - 6 pin (max. 250 °F)[5] 6d. Microtec DR-4S-4H 4 pin 6e. Integral cable: Teflon 6f. Integral cable: PVC 6g. Integral cable: Neoprene (max. 180 °F) 6h. Integral cable: Silicone 6i. Integral underwater cable (max. 180 °F) 6v. Phoenix connector on end of cable 15d. Connector on end of cable
Special calibration	9a. 10 point (5 up/5 down) 20 % increments @ 20 °C 9b. 20 point (10 up/10 down) 10 % increments @ 20 °C
Special calibration	30a. Compression only calibration, positive in compression 30b. Tension and compression calibration, positive in tension 30c. Compression only calibration, negative in compression
Shock and vibration	44a. Shock and vibration resistance
Interfaces[4]	53e. Signature calibration[7] 53t. TEDS IEEE 1451.4 module

C1. CAMERA SPEC SHEET (Manta G-419, Allied Vision)

Allied Vision

GiGE VISION

Manta

G-419

- CMOSIS CMV4000 sensor
- Power over Ethernet option
- Angled head and board level variants
- Video-iris lens control

Description

GigE camera with CMOSIS CMV4000 CMOS sensor, global shutter

Manta G-419B/G-419C is a machine vision camera that incorporates the high quality Type 1 (16 mm diagonal) CMOSIS CMV4000 CMOS sensor. At full resolution, this camera runs 28.6 frames per second. With a smaller region of interest, higher frame rates are possible. The Manta is one of Allied Vision's versatile GigE Vision cameras with a wide range of features. Particular highlights are the three look-up tables, sophisticated color correction capabilities, a robust metal housing, and many modular options. By default monochrome models ship with protection glass B 270 (ASG) and color models ship with an IRC Hoya C-5000 IR cut filter.

Options:

- Power over Ethernet (PoE)
- Various optical filter and lens mount options
- Angled head, board level variants, white medical housing

See the Modular Concept for lens mount, housing variants, optical filters, case design, and other modular options.

Specifications

Manta	**G-419**
Interface	IEEE 802.3 1000BASE-T, IEEE 802.3af (PoE) optional
Resolution	2048 (H) × 2048 (V)
Sensor	CMOSIS CMV4000
Sensor type	CMOS
Cell size	5.5 µm x 5.5 µm

C2. CAMERA SPEC SHEET (cont'd, Manta G-419, Allied Vision)

Allied Vision

Manta	G-419
Lens mount	C-Mount
Max frame rate at full resolution	28.6 fps
ADC	12 bit
Image buffer (RAM)	128 MByte
Output	
Bit depth	8-12 bit
Mono modes	Mono8, Mono12, Mono12Packed
Color modes YUV	YUV411Packed, YUV422Packed, YUV444Packed
Color modes RGB	RGB8Packed, BGR8Packed, RGBA8Packed, BGRA8Packed
Raw modes	BayerGB8, BayerGB12, BayerGB12Packed
General purpose inputs/outputs (GPIOs)	
Opto-isolated I/Os	2 inputs, 2 outputs
RS-232	1
Operating conditions/dimensions	
Operating temperature	+5 °C to +45 °C ambient (without condensation)
Power requirements (DC)	8 to 30 VDC; PoE
Power consumption (@12 V)	2.7 W @ 12 VDC; 3.1 W PoE
Mass	190 g; 200 g (PoE)
Body dimensions (L × W × H in mm)	86.4 × 44 × 29 (including connectors)
Regulations	CE, RoHS, REACH, WEEE, FCC, ICES

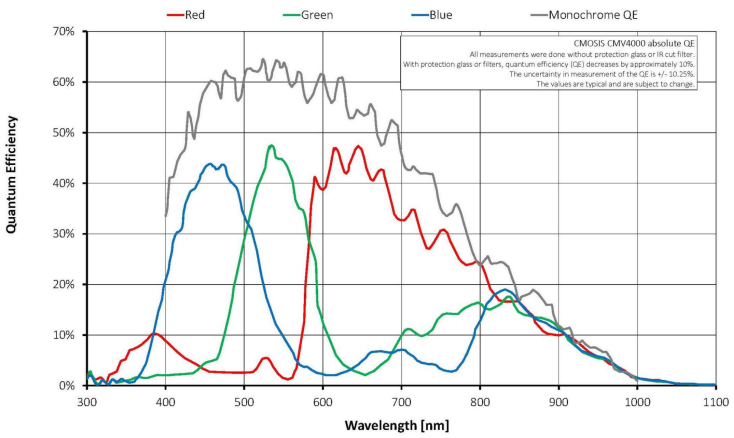

D1. GRIP DRAWINGS: BOTTOM CLAMP

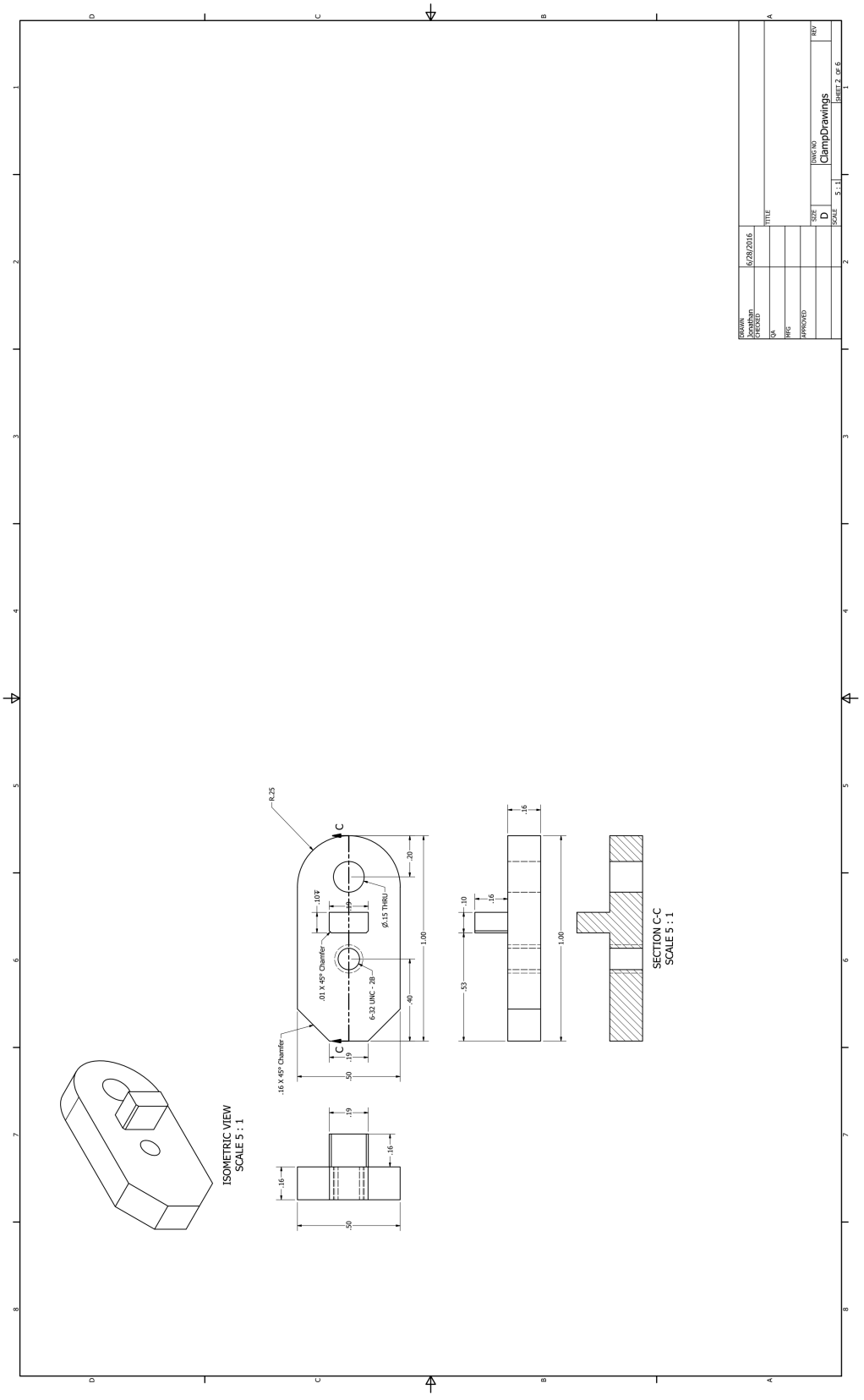

D2. GRIP DRAWINGS: TOP CLAMP

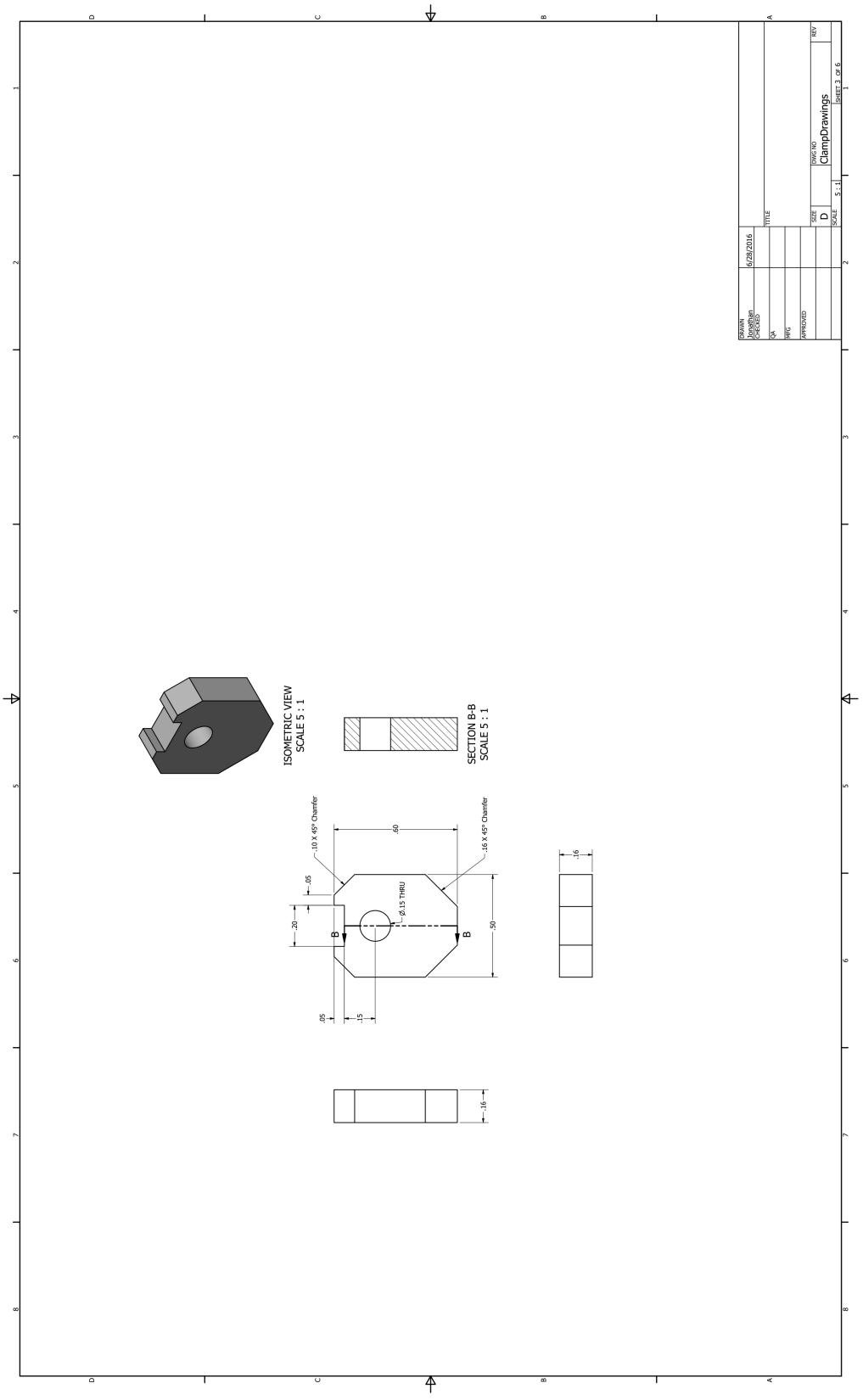

D3. GRIP DRAWINGS: CLAMP HOLDER

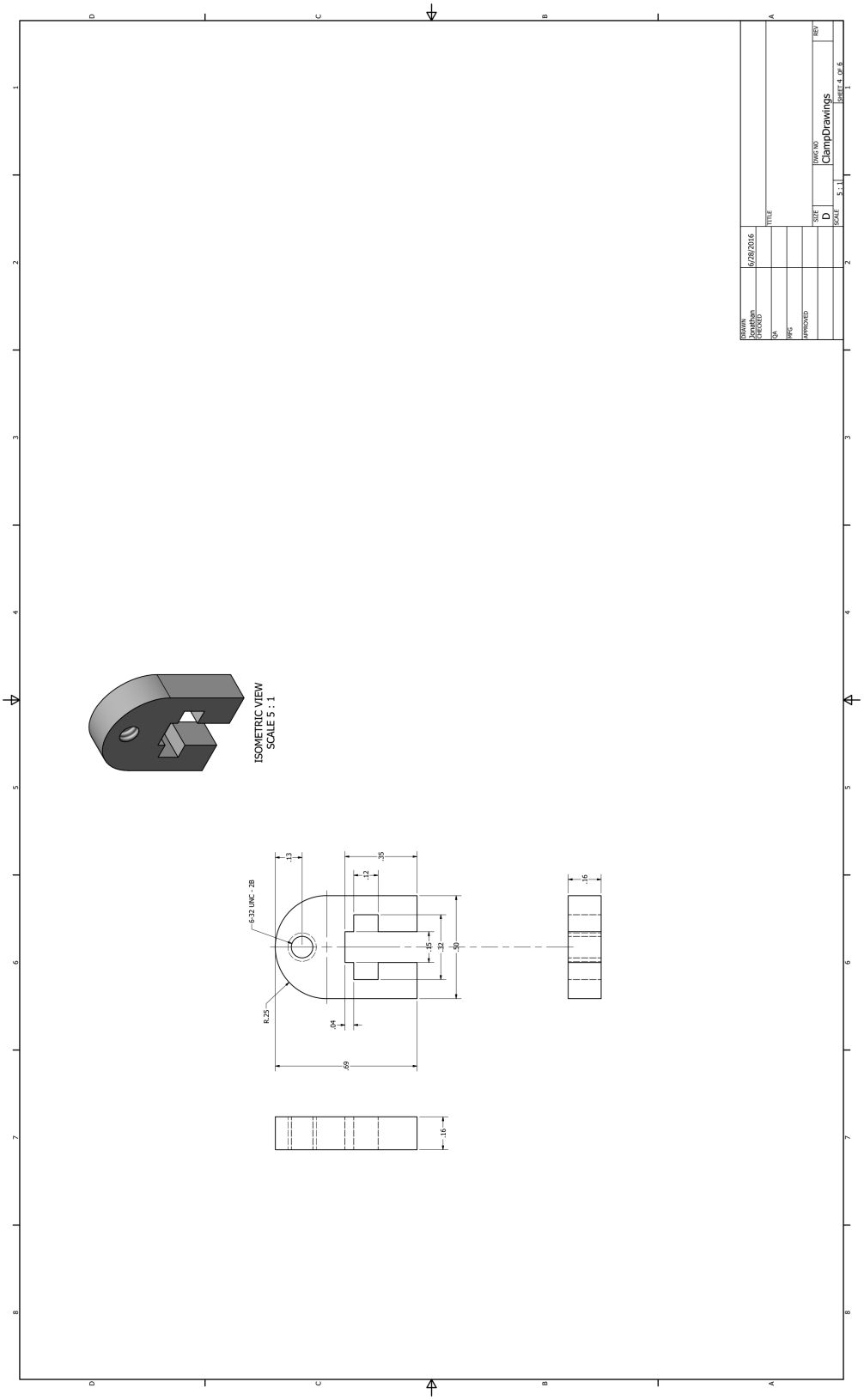

E1. ADAPTER DRAWINGS: LOAD CELL TO GRIP

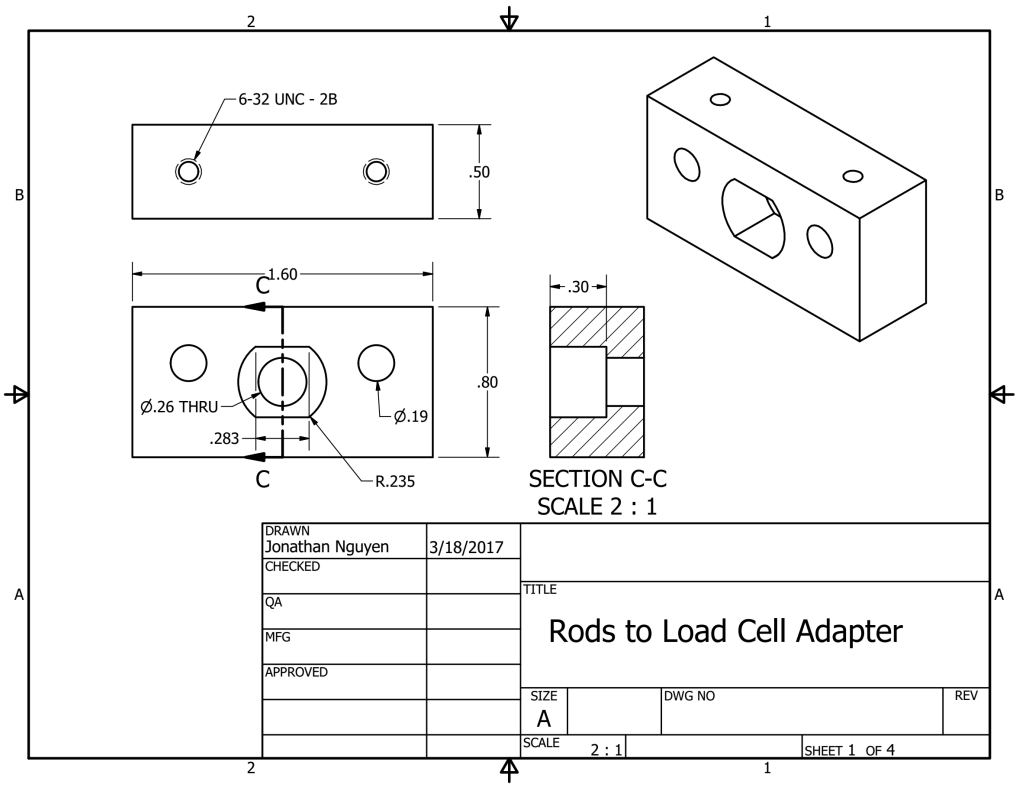

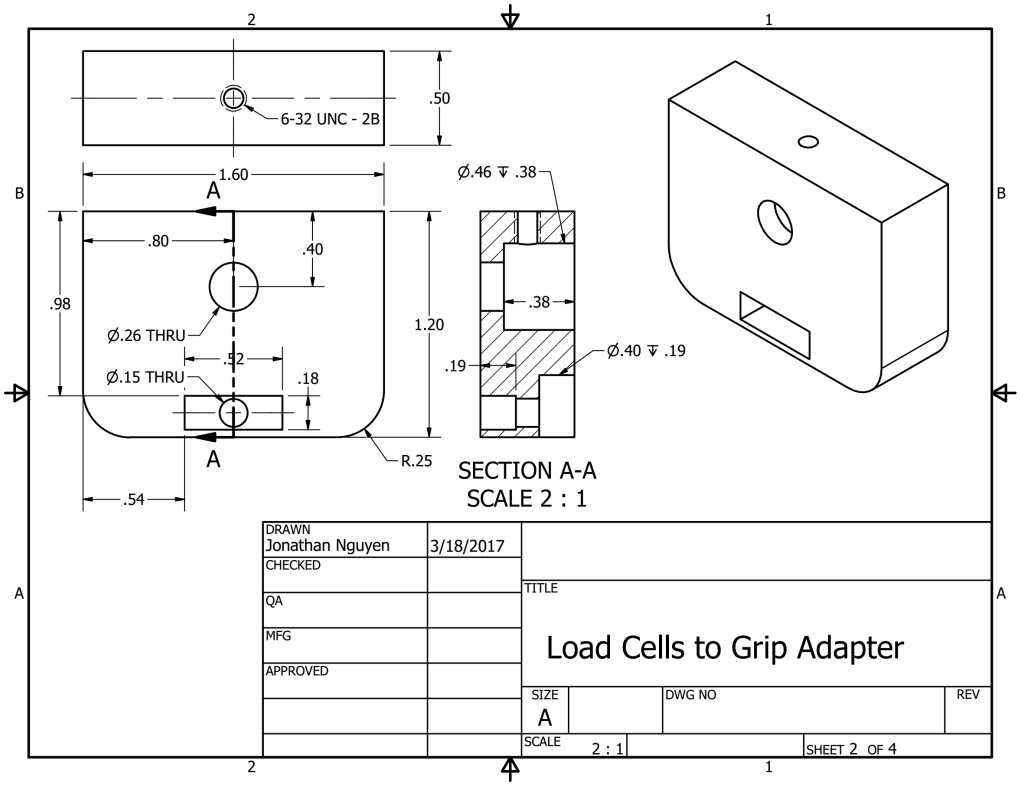

E2. ADAPTER DRAWINGS: RODS TO GRIP

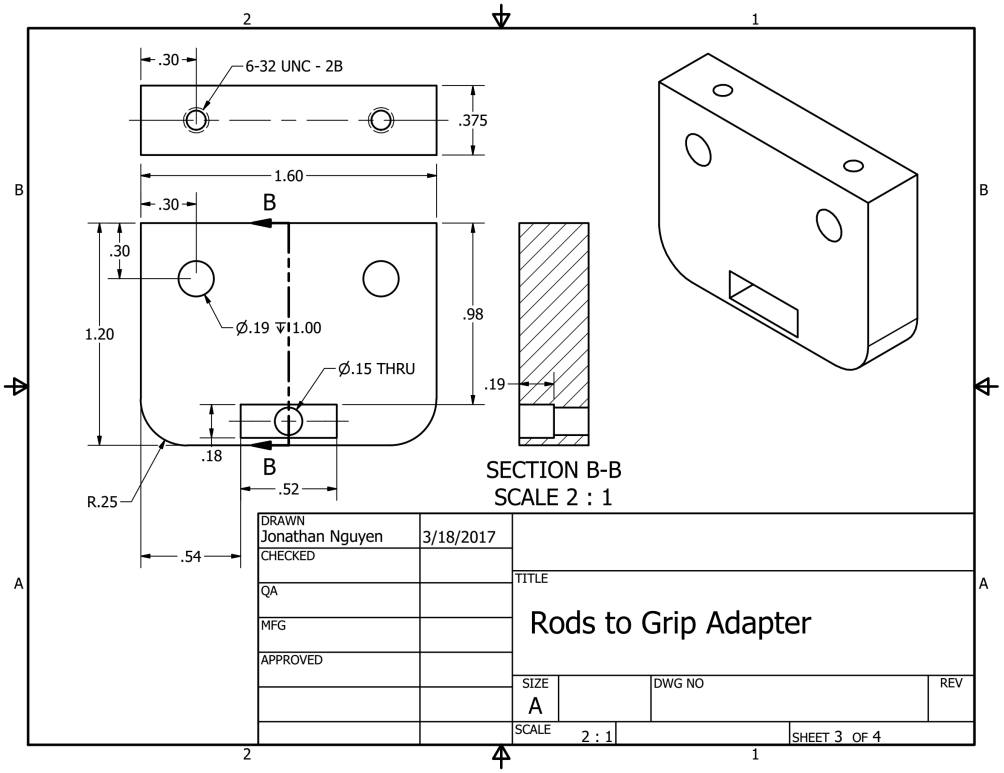

E3. ADAPTER DRAWINGS: LINEAR SCREW TO ROD

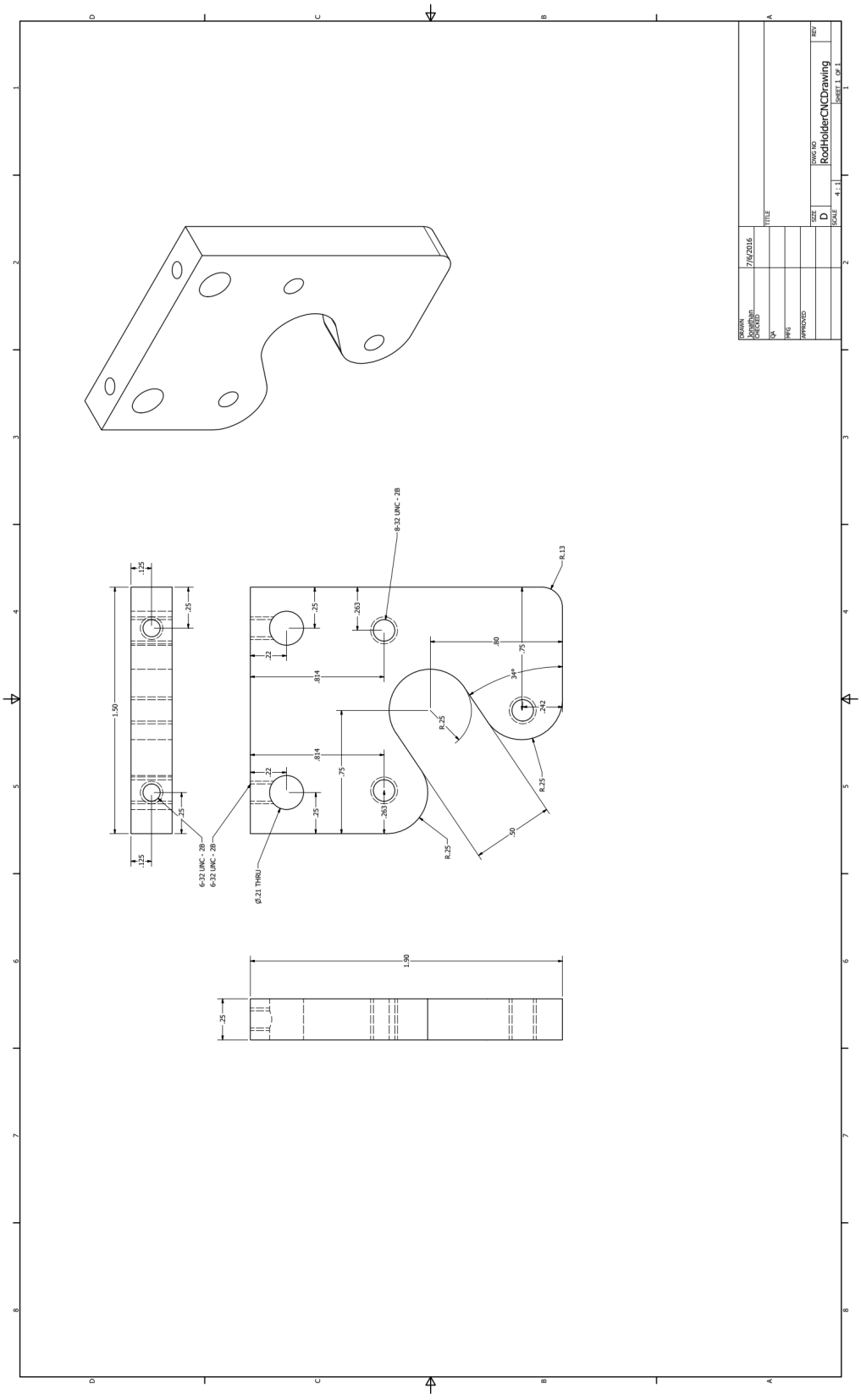

F. TANK DRAWING (for 12” tank)

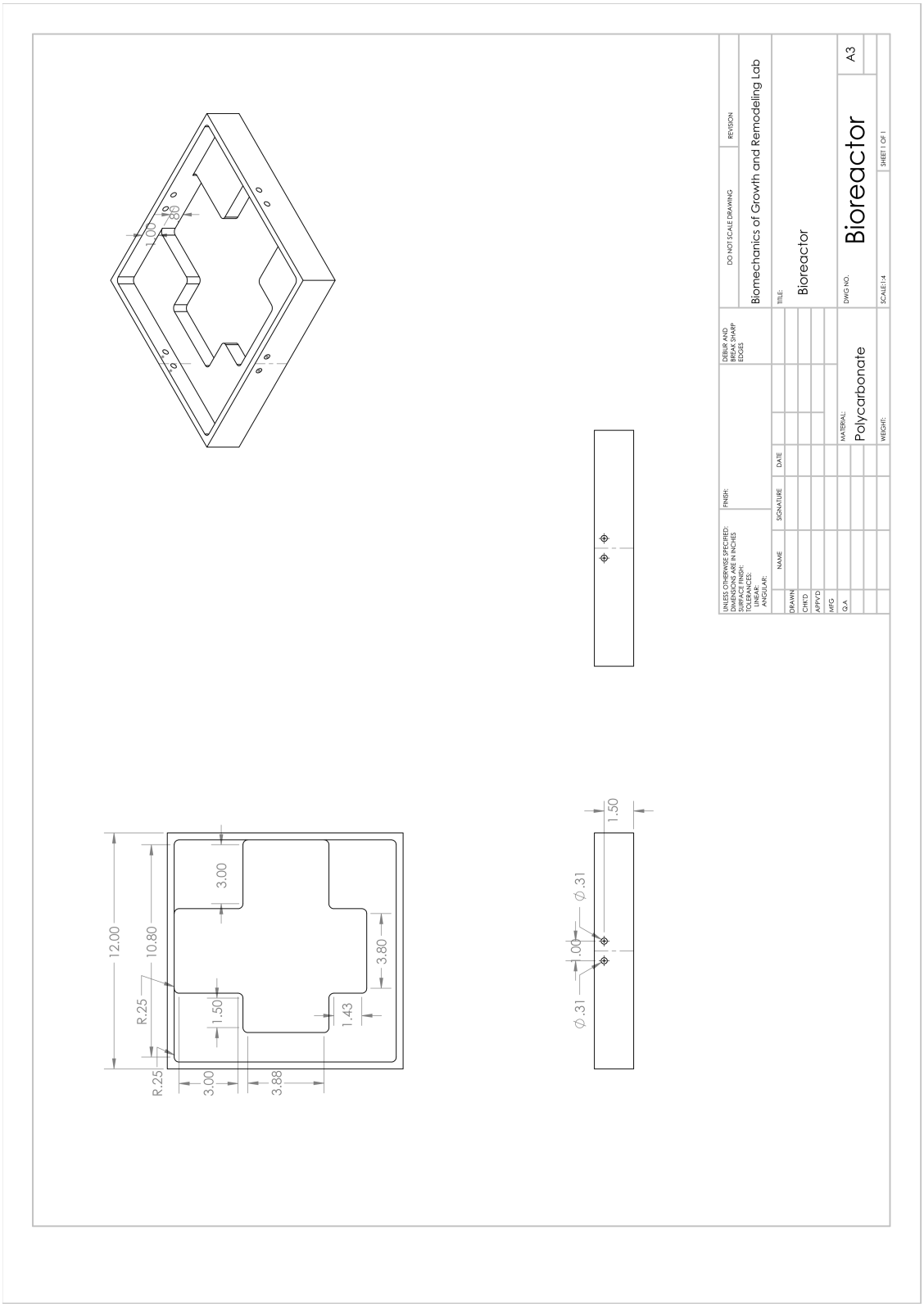

G. BASE DRAWING (for 12” tank)

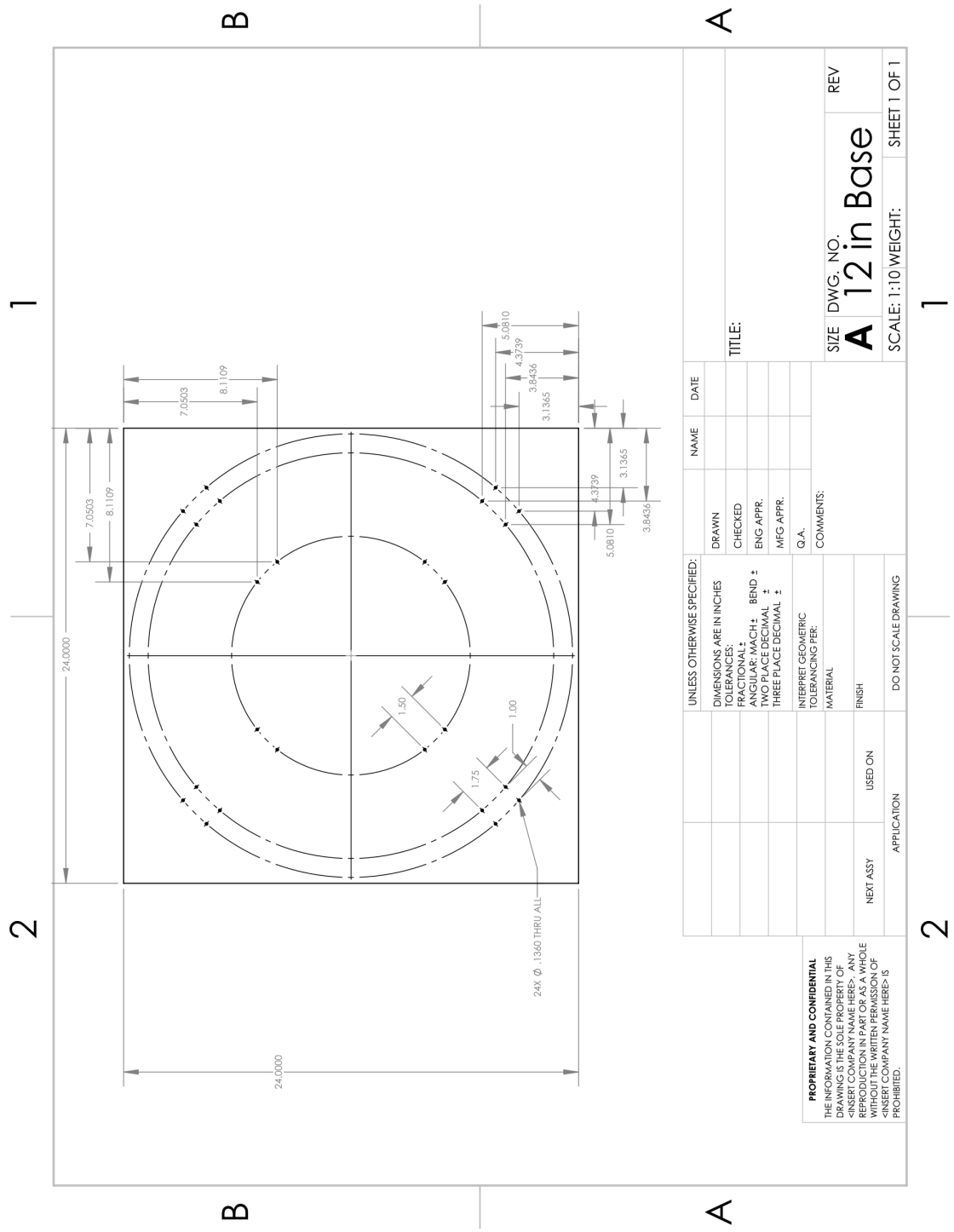

H1. ASSISTING DEVICES (to align grips)

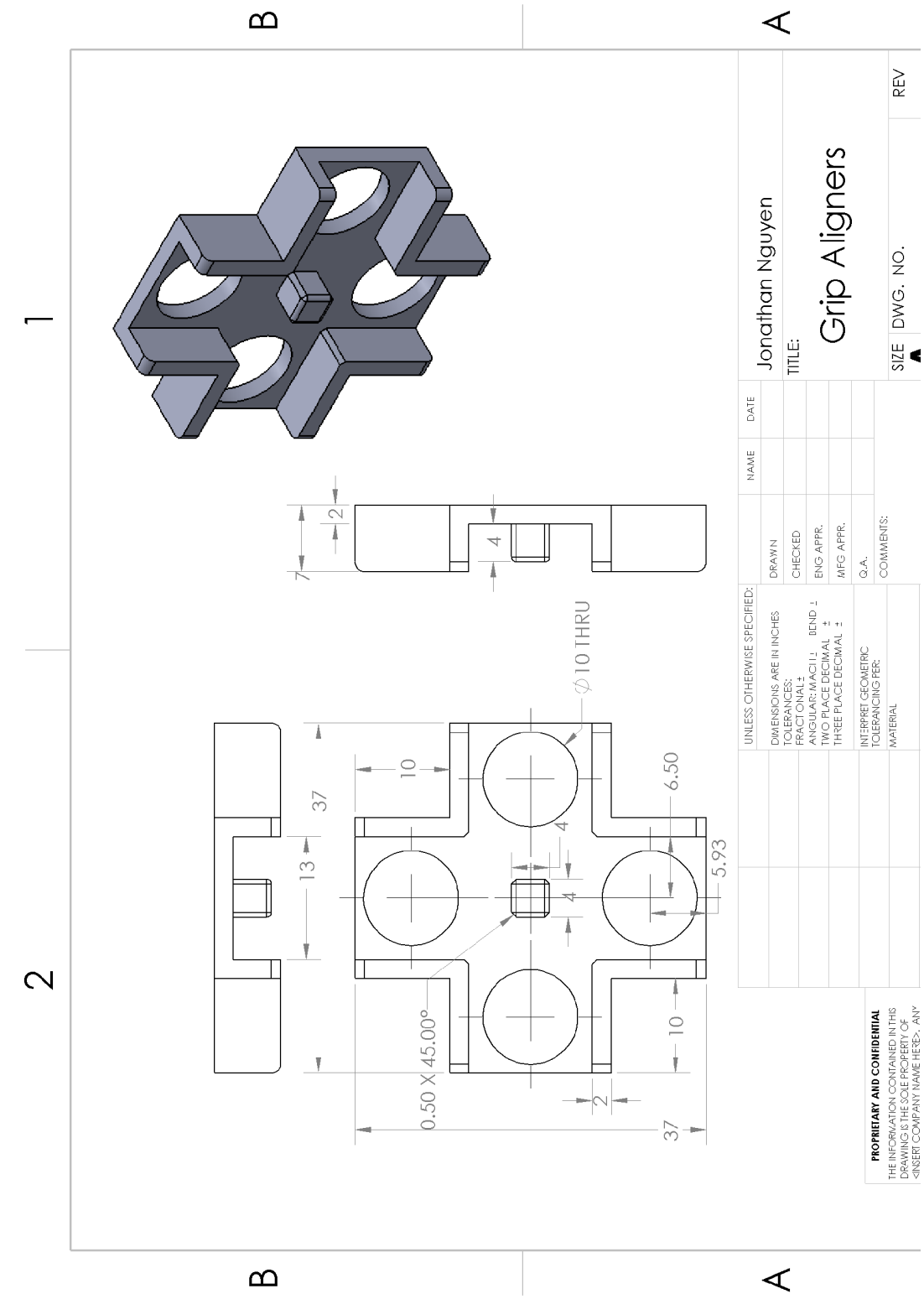

H2. ASSISTING DEVICES (for load cell calibration)

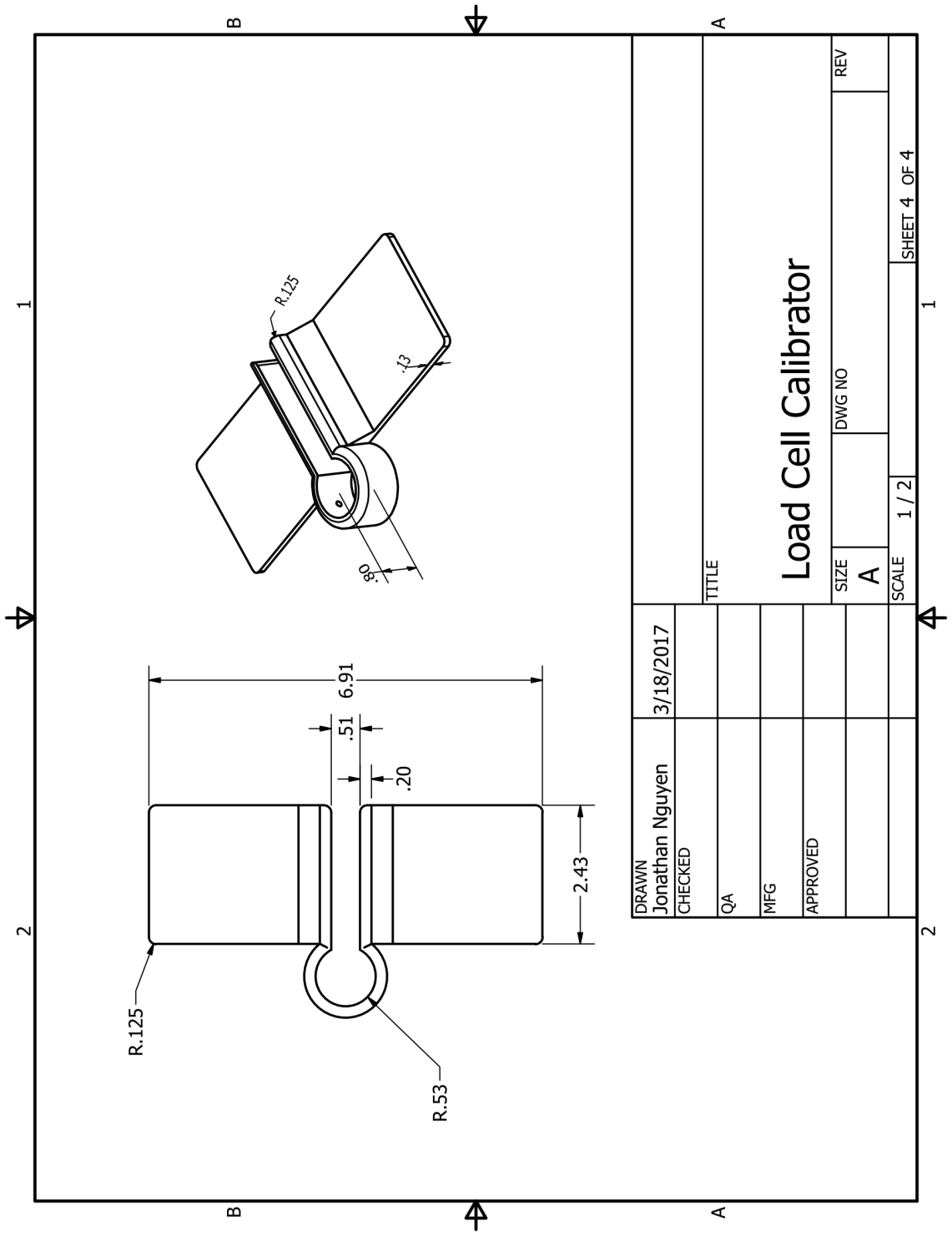

I. CAMERA MOUNTING PLATE (from David Simon, Yale)

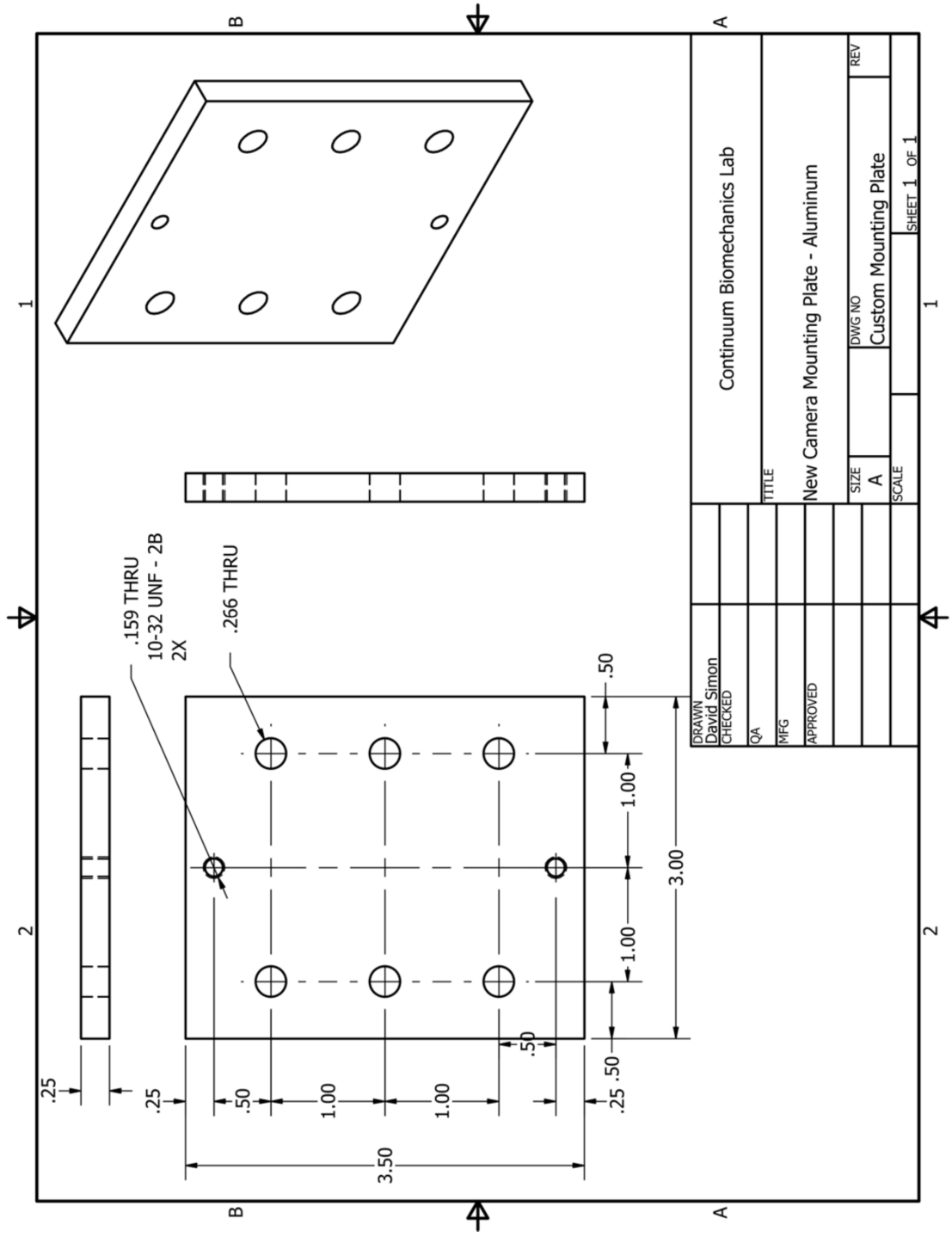

J. SKIN DISSECTION PROTOCOL

1. Lay down dissection pad at site. A scalpel, forceps, and dissection scissors are needed for skin dissections. Also lay down KimWipes, a disposable pipette, a small sheet of aluminum foil (about 4 in. x 4 in.), a small re-sealable plastic bag, and a petri dish containing HBSS.
2. Remove mouse to be dissected from freezer and place on dissection pad for thawing while still in bag. 1.5 to 2 hours of thawing should be sufficient. Remove mice from bag and unwrap from foil. During dissection, the mouse should be periodically hydrated with HBSS to prevent tissue sticking and drying.
3. A scalpel can be used to make an initial cut in the skin if needed. Abdominal skin is the easiest to cut a large sample from, but thoracic and hind leg skin may also be cut away for tests. Care must be taken to cut as superficially as possible to avoid internal damage. Dissection scissors should be used if possible to cut the skin flap for testing.
4. The final skin specimen should be at least 15 mm x 15 mm and square-shaped. Keep this sample hydrated with HBSS as well.
5. If not testing right away, place the skin sample on the sheet of foil and hydrate with HBSS. Then fold the foil over the skin sample and fold in each edge, ensuring the skin sample lays flat inside.
6. Place the skin sample in the plastic baggie and mark it with mouse information, type of sample taken, dissection date, and dissector. Rewrap mice in foil and place in bag. Make a note on the bag with date, dissection type, and dissector.
7. Place mice and skin sample in freezer.
8. Clean tools by squirting soap solution into beaker and bathing tools in the beaker. After cleaning, tools should be removed, dried, and placed back in the tools drawer.

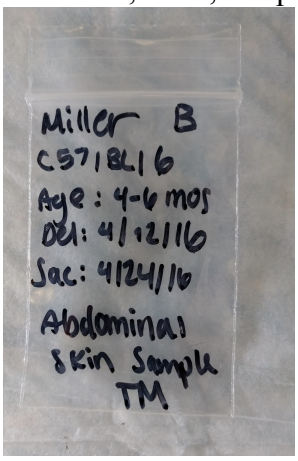

Example of how to note a bag for frozen tissue samples

K. MOUSE REPRODUCTIVE ORGAN DISSECTION PROTOCOL

(adopted from in-lab protocol)

Materials:

1) Diaper
2) Tools:
    a) Forceps
    b) Scissors
    c) Micro-Scissors
    d) Angled Tweezers
    e) Straight Tweezers
3) Aluminum Foil
4) Tape
5) Tex Wipes
6) Petri Dish
7) Syringe
8) HBSS Solution
9) Permanent Marker
10) Gloves
11) India ink

Set Up:

Everything from this point forward should be done with gloves on

1) Place diaper on worktop under microscope
2) Fill petri dish halfway with HBSS solution
3) Fill syringe with HBSS solution
4) Set aside Tex Wipe for tissue disposal
5) Place mouse on sheet of foil ventral side up, taping the front and back paws and tail to the foil
6) Place mouse+foil configuration under the microscope on top of the diaper
7) Turn microscope lights on and adjust microscope to appropriate magnification

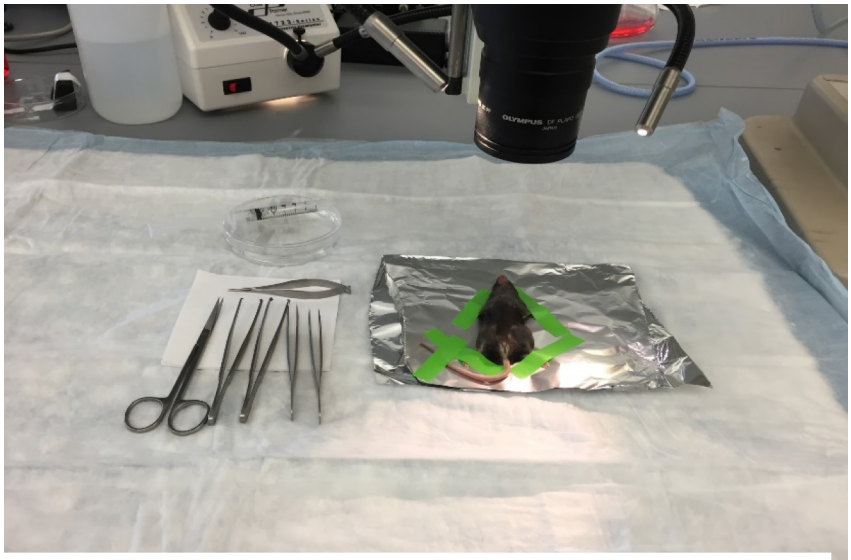

Figure 1: Set up prior to dissection

Methods:

1) Using tweezers and micro-scissors, lift skin and make incision at base of the abdomen.
   a) Be careful not to puncture intestines; you will have to tie off the punctured intestine with a suture and wash the cavity thoroughly with saline
2) Cut superiorly to just below rib cage, then cut laterally from the top of the original incision to the lateral most part of abdomen
3) Cut laterally from base of original incision to the lateral most part of abdomen
4) Carefully move the intestines out of cavity by lifting from below
   a) Be careful not to cut intestines
5) Under the microscope, remove superficial fat by pulling lightly on the fat with angled tweezer and cutting away excess with micro-scissors.
6) Place all removed tissue on designated Tex Wipe
7) Make sure that each uterine horn is visible.
8) Remove superficial fat and muscle so that pubic bone is visible

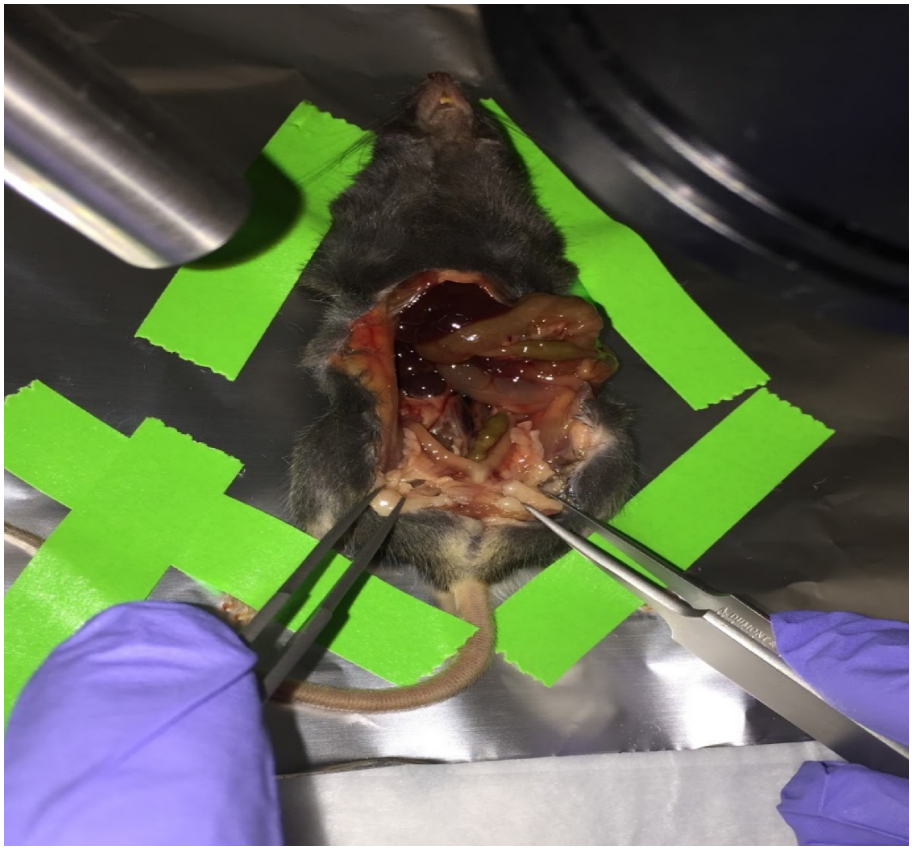

Figure 2: Uterine horns exposed and some excess fat removed

9) Place closed micro scissors between vagina and pubic bone (the pubic symphysis) and carefully separate the two
   a) Make sure that scissors are visible on inferior side of pubic bone
10) Cut pubic symphysis
   a) Look at Figure 4 for reference

11) Cut away at the protruding bone at least to the outer edges of the vagina to allow better access.

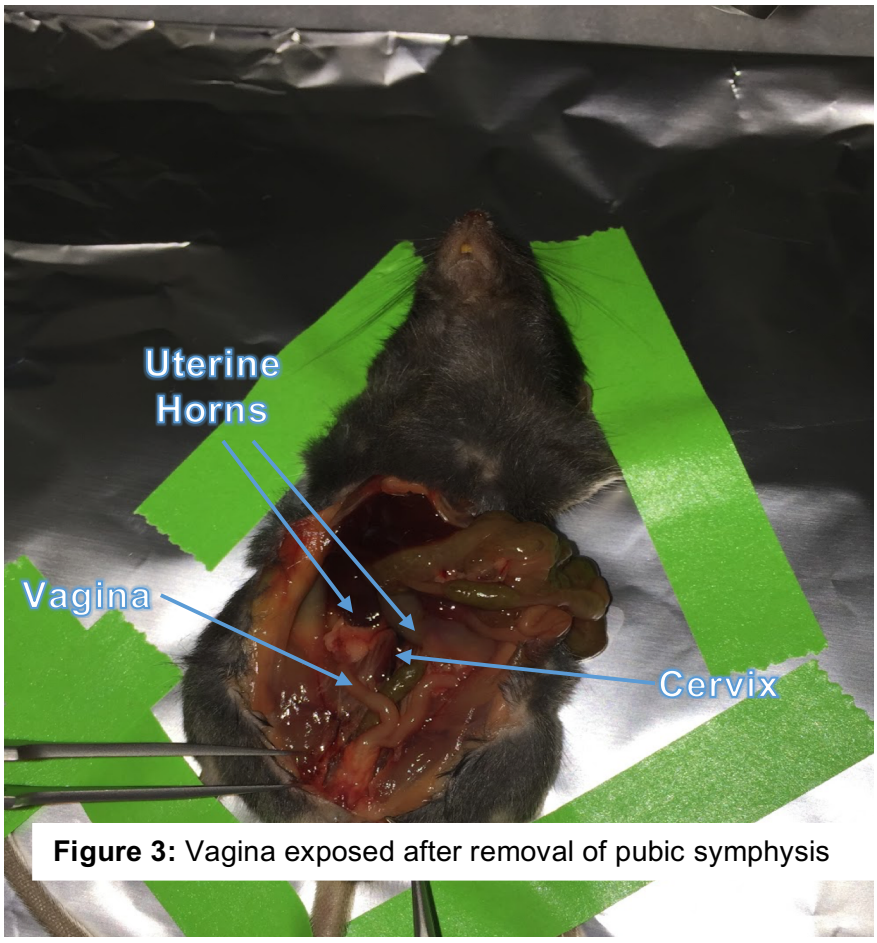

Figure 3: Vagina exposed after removal of pubic symphysis

12) Start removing the bladder and urethra from the ventral side of the vagina using tweezers and micro-scissors as a dissection method to separate the two.
    a) Hold bladder with forceps to create tension.
    b) Aim sharp part of forceps toward urethra in order to protect vagina.
13) Once the bladder is completely dissected away, cut base and remove from cavity.
14) Once entire reproductive system is visible get out india ink to mark 3mm dots.
15) Using the calipers measure a 3 mm piece of suture under the microscope
16) Using the 3mm piece of suture as a measuring tool, the india ink, and the angled tweezers, place dots on each uteri, spaced 3 mm apart, leaving a little room between the ovary and uterus.
    a) Place as many dots as necessary to reach cervix.
        1) Located where the uteri begin to bifurcate
17) Figure 4 below shows the path of the dots.
    a) Go from end of one uterus to center of cervix then use the center cervix dot to start dot path up other uterus.
    b) Finally use center cervix dot to start dot path down vagina to introitus.
18) Allow india ink to dry then begin separating repro tract from surrounding fat and tissue.

19) Using microscissors with the angled tweezers, separate the uterine horns and cervix from the surrounding connective tissue.
20) Carefully separate the cervix and vagina from the colon
21) Clean the vagina as close to the vaginal introitus (Figure 4) as possible
22) Using micro-scissors cut around the vaginal introitus
    a) Some hair and skin remaining around the external portion of the vagina is fine
23) Cut the uterine horns above the bifurcation from the cervix/vagina

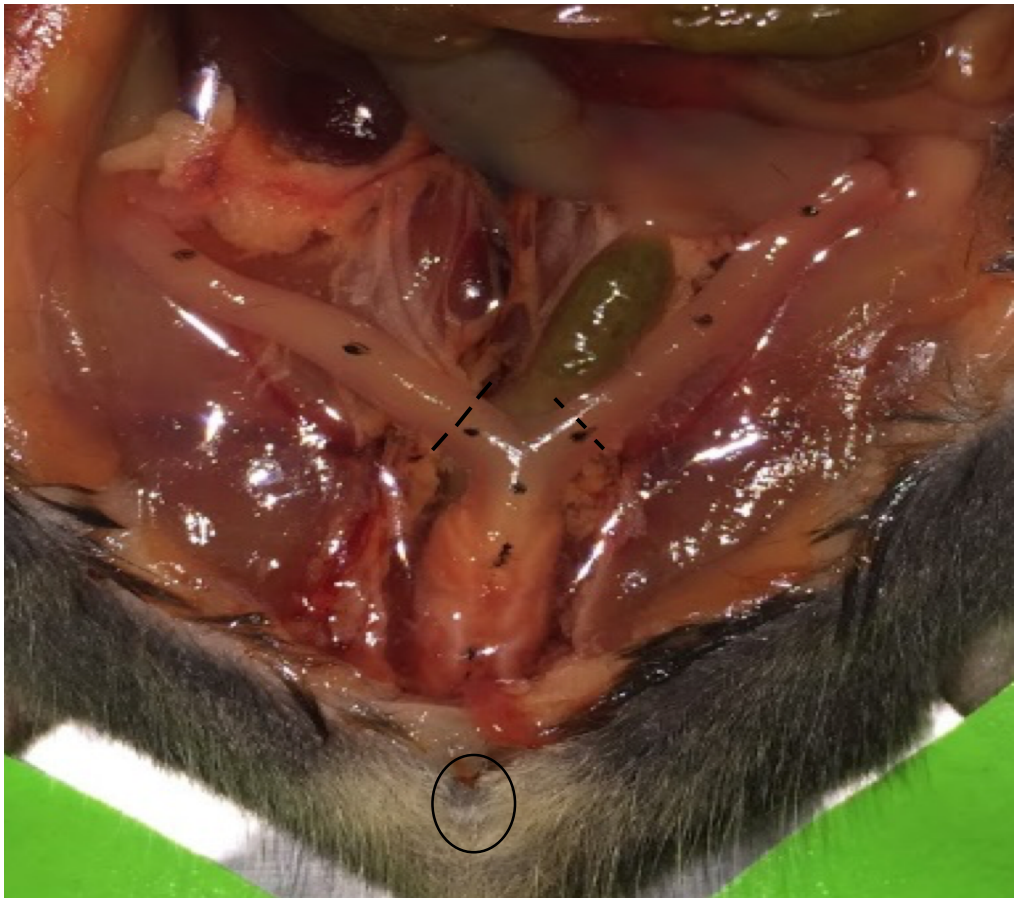

Figure 4: Location of dots and cuts to remove reproductive system

24) Place dissected tissue in petri dish with HBSS solution

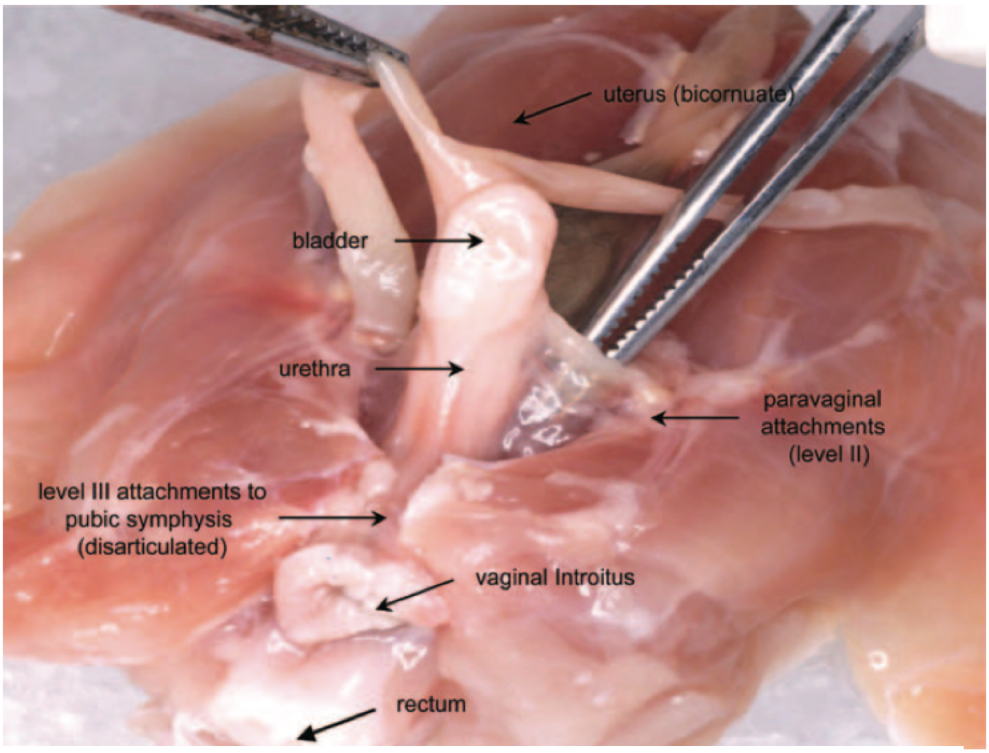

Figure 4: Pubic symphysis cut away with bladder and urethra still attached. Figure from Abramowitch et al. 2009.

Clean-up:

1) Fill large beaker with soap and warm water, place tools in bath and let sit for 5 minutes.
2) Place Tex Wipe over dissected mouse and fold aluminum foil over mouse and all removed tissue.
3) Place wrapped mouse in ziploc bag, label parts removed and date of dissection.
4) Place removed vagina in a screw top tube with HBSS
5) Freeze at

L1. GRIPPING PROTOCOL (sample preparation)

1. Set up dissection pad. The tools needed are forceps, scalpel, KimWipes, cotton swabs, a disposable pipette, and a petri dish of HBSS. If gripping mice skin, Nair is also needed.
2. Remove sample from freezer and let thaw in bag. For skin samples, this need not be longer than 30 minutes. For cryopreserved human tissue, wait time may be hours for thawing, although samples can safely be left at ambient temperature for up to nine hours (Rubod, 2007). Tissue can be checked periodically for thawing progress.
3. If not gripping mice skin, skip to step 8. Use the scalpel to gently shave off most of the hairs from the mice skin. Tape can be used to temporarily hold the skin if needed.

4. (Skin only) Flip skin over and use forceps to remove fascia and adipose tissue from beneath skin. It has a reddish tint. Mouse skin is gray-white. Keep skin hydrated during this process. It will bunch up and become significantly thinner.
5. (Skin only) Flip skin over again to hairy side. Apply a small amount of Nair to a cotton swab and apply to the skin, focusing on the remaining hair. Be sure to push the Nair all the way out to the edges of the skin. Wait for two or three minutes.
6. (Skin only) Use scalpel and forceps to gently push hair from the depilated skin. Wipe gently with a fresh cotton swab.
7. (Skin only) When all the hair is sufficiently removed, rinse the tissue thoroughly with HBSS. Repeat rinses are necessary while wiping with a cotton swab.
8. Orient the tissue so that known fiber alignment corresponds to the biaxial axes of loading. Use the cruciform stamping tool to cut the specimen shape with the tissue fibers aligned along the arms. Reserve the remaining tissue if needed for histology.
9.

L2. GRIPPING PROTOCOL (gripping samples)

1. Tissue should now be ready for gripping. Prepare the grip components (four bottom clamps, four top clamps, and 4 6-32 screws) and grip aligning device ahead of time. Four small sandpaper tabs, roughly 5 mm x 5 mm, and cyanoacrylate (Super Glue) are also needed. A toothpick and India ink are needed in addition to previously required tools. Place the bottom clamps into the grip aligner.
2. Place tissue on KimWipe and hydrate with HBSS.
3. Hold sandpaper tab with forceps and apply small dab of cyanoacrylate on the smooth side. Lift one arm of the tissue specimen and place sandpaper tab beneath it with the glue side up, approximately 1 mm into the arm. The sandpaper tabs are adhered to both the top and bottom of each arm. Apply a small amount of pressure to fix the tissue to the tab.
4. Repeat for the other three bottom tabs.
5. Apply a small drop of glue to each sandpaper tab and then immediately fold the tabs over the top of the cruciform arms. Then a small amount of pressure can be applied to fix the tabs. Take care to ensure tissue or sandpaper does not become stuck to the KimWipe. Care must also be taken to keep sandpaper away from the central region of the tissue specimen, and that each arm is about the same width and length.
6. After ensuring tissue is hydrated, use forceps to transfer tissue to bottom clamp and aligner complex. Each sandpaper tab should fit at the end of each bottom clamp. Try to not let them stick out of the grip.
7. Place each top clamp on the bottom clamp, with the notch of each top clamp aligning with the extension on each bottom clamp.
8. Screw down each top clamp tightly.
9. On the biaxial device, ensure all settings for motion are activated. Remove camera assembly from device.
10. Transfer the entire assembly, assisting device included, to the biaxial device. The device motors should be moved until the assembly can be slotted onto the grip adapters, with all four holes lining up. Keep the assisting device for now as it prevents unnecessary loading and torsion of the tissue specimen.

11. Screw down each grip to its adapter tightly. When securing to the load cell adapters, a small block can be used beneath the grip adapter to prevent introducing a lateral moment to the load cells.
12. Snap down the grip assisting device and slide out from biaxial device.
13. Using a toothpick, apply four small dots of India ink, forming a square, at each corner of the tissue specimen. Dots must contrast sharply to the tissue sample and be relatively small and circular. Alternatively, use a small pipette to hold a poppy seed. The seed can be planted into the tissue with a small burst of air.
14. Fill first level of tank with HBSS to ensure tissue hydration. Replace camera over tissue specimen. Tissue is now ready to test.

Left: Mice skin before preparation. Right: Mice skin gripped and ready for transfer

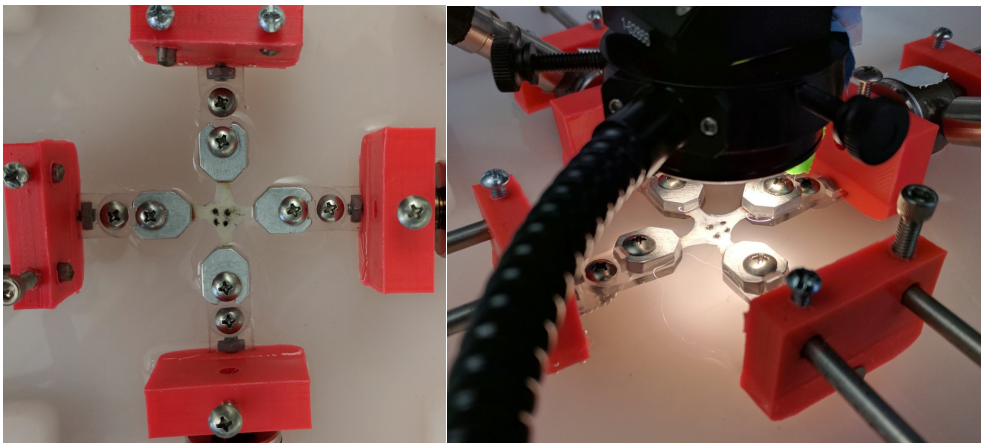

Left: Grips secured in biaxial device with sample. Right: Device with camera system on

M. LABVIEW PROTOCOL

1. Turn on motor controllers and fiber optic light.
2. Copy the template folder *PBD Template* and give it a name like TEST TYPE_DATE_INITIALS (example: Biaxial_033117_JN). Rename the Excel file in the folder to the same name.
3. Run *Initialize.vi* once. If motors controller communication is successfully established, a character, using '&' or 'ÿ', will appear in the command read out.
4. Run the main program *Mechanical_Test.vi.*
5. Input tissue information, height and width, as well as relevant testing parameters, including max and min strain, tolerance, and stretch rate.
6. Click the folder pathway dialogue box and select the template folder you just created. Click the OK button beneath the folder pathways to initialize the path information and subfolders for each image.
7. Click Initialize for the motor systems and then the OK button for initial, slew, and step size parameters. Ensure each textbox has the correct number (400, 3004, 3200). Motors can now be moved.
8. When tissue is unloaded, zero the load cells in the data acquisition panel.
9. Adjust light settings to illuminate tissue as well as possible. Move camera stage and focus to center tissue. Then adjust camera settings using the drop-down menu in the vision section. Only gain and exposure time needed be adjusted. Raising either will increase image brightness. Pay attention to the histogram, which shows luma distribution. There should be a large peak at the right end (bright background) and another peak towards the left end (tracking points).
10. Adjust the motors until tissue is in reference configuration.
11. Select Stop Image Capture and then save the first image. Then adjust the upper and lower thresholds until particles are isolated. The lower should always be below the upper. Anything between the upper and lower will be white, while anything outside will be black. Additionally, morphological operations and erosions can be changed to better isolate particles. This step must be accomplished through trial and error. Confirm when particles are isolated.
12. A window will pop up. Click and drag a rectangular mask encompassing the bottom left particle and then press enter. Repeat this for the next three particles. The order is: bottom left, bottom right, top right, top left. Afterward you must select the Excel file that was previous created.
13. Examine the tracking to make sure bounding boxes do not drift. If they do, you must start again. For standard 2D biaxial tests, you want the deformation gradient set to 2D mode. 1D mode is available for uniaxial tracking. If tracking is accurate, click the Set Origin button and then click and briefly hold the Set Reference Configuration button.
14. A deformation gradient should now be calculated. If bounding boxes appear too close together, the search region may be lowered. The search region helps the program relocate particles during a test. It may be raised if tracking appears inaccurate. This parameter is also arrived at through trial and error.
15. Select the desired testing protocol. Then, finally, click Start test. The testing protocol will now automatically run.

16. Open the Excel file in Notepad++ and copy all the data to an empty Excel sheet. Data will now be properly formatted and ready for additional processing.

N. MATLAB PROTOCOL

1. Run *UI.m,* which is the main function file. The window, detailed below, contains the tools needed to track a sequence of *.tif images.

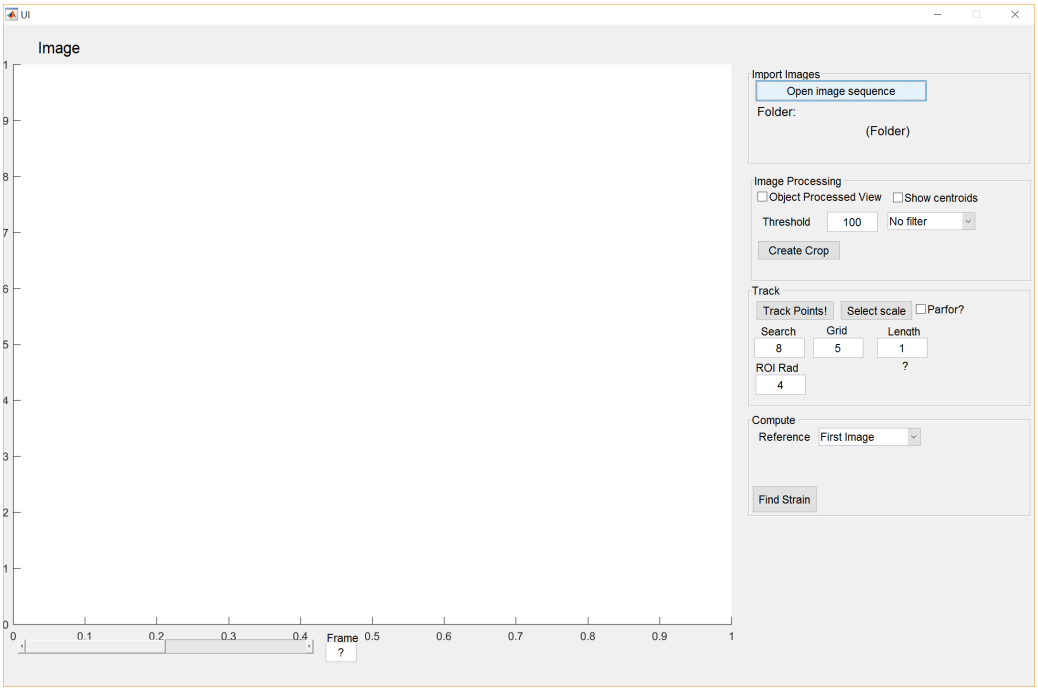

Main window seen upon running program for the first time

2. Click *Open Image Sequence* and select but do not open the folder that the images are stored in. Click OK to select that folder. The sequence is now loaded into the program.
3. The default tracking mode is 'blob tracking' which attempts to detect particles in the image. The *Object Processed View* toggle may be used to see the final thresholded image. *Show Centroids* refreshes and toggles an overlay that shows the center of each detected particle and the search circle for finding deformed particles from reference particles.

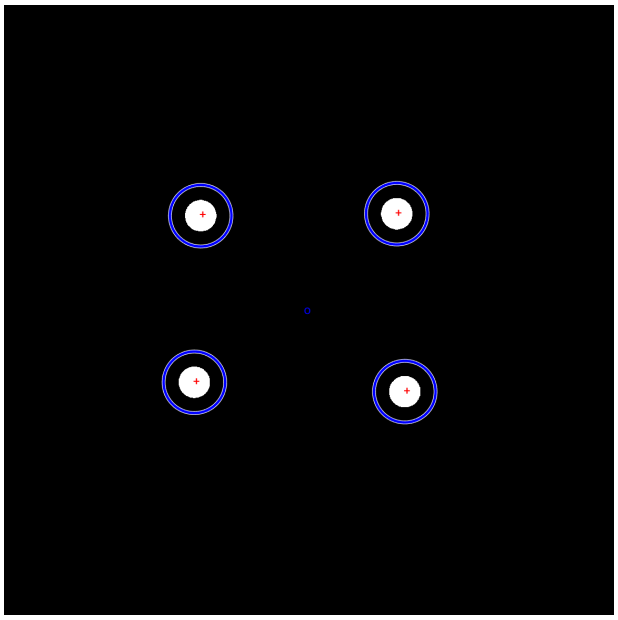

Processed object view with centroid and search radius

4. The current image can be changed by dragging the slider, clicking the arrows next to the slider, or typing in a specific image number at the bottom of the window.
5. The threshold textbox changes the binary threshold of the image. In the image, any luminance, which will be from 0 – 255, below that value will become black while anything above it becomes white. Keep in mind the image is inverted. An array of contrast and smoothing filters may also be applied in case thresholding is not sufficient.
6. *Create crop* allows the creation of a rectangular ROI which masks out the unwanted borders of the images. This may have to be done if particles are being detected outside the central region. Additionally, it sets an origin for the particles, although one is already assigned based on image size.
7. The Search (radius) textbox controls the max distance deformed particles can be from reference particles before they are interpreted as separate entities by the program. A larger search radius is necessary if deformation rate is fast. The perimeter of the visualized circle should overlay deformed particles.
8. *Select scale* allows the placement of a line that can convert the pixel displacement to a custom scale, such as micrometers. The known real-world length of the line drawn is entered into the length textbox.
9. It may be necessary to change tracking methods. This is accomplished internally due to some knowledge of MatLab required to complete these tracks. Four point tracking was chosen as the main because it mirrored the LabView interface. The method can be changed at line 347 in *UI.main*.
10. The Grid textbox determines the dimensions, or how many points per axis, of the grid of points that tracks full-field displacement. The ROI Rad textbox determines the size of the reference template image for each point. Search is again used to determine max search distance, but must be shrunk due to the smaller displacement of each individual point.

11. The full-field DIC tracking method uses a combination of the *corr2* MatLab function and RMS error of image subtraction, which is considerably slow to run.
12. If all settings are satisfactory, click *Track Points!* A loading window will pop up and provide information of the tracking progress.
13. After tracking is complete, if 'blob tracking' was used, tracking lines will appear to verify the accuracy of the track.
14. Computations can be performed based on the first image or the previous image as a reference image.
15. Finally, click the *Find Strain* button to plot the experimental strains and stresses.

O. DESCRIPTION OF MATLAB FUNCTIONS

Create_image_array:	reads an image into a MatLab matrix array
DIC_tracking:	Generates a grid on the region of analysis where each intersection point is a tracking marker for full-field displacement. Groups of 4 points are clustered to form local deformation gradients.
Draw_tracklines:	Draws lines to show tracking information for four-point tracking (Tinevez, 2011, MatLab Central)
Find_4pt_strain:	Calculates tissue deformation from either the first image or previous image for four-point tracking
Find_def_grad:	Sorts four particles to their respective quadrants and calculates deformation gradient
Find_def_grad_corr:	Calculates deformation gradient for non-particle-tracking methods
gaussSmooth:	Applies Gaussian smoothing, but may be effective only for color images. Part of Piotr's Image & Video toolbox(Dollar, 2008, MatLab Central)
Hungarianlinker:	Links found particles during tracking based on Hungarian algorithm to minimize Euclidean distance between particles. (Tinevez and Cao, 2011, MatLab Central)
Hybrid_im_corr_ser:	Single-thread 4-point correlation function to locate similar patterns in image texture compared to a reference image and report new point location. Better for low-spec computers and less buggy.
Hybrid4PtTrack:	4 point tracking that incorporates image correlation techniques instead of particle detection
Im_corr:	Parallel-thread correlation function for finding similar image patterns compared to a previous reference image
Im_corr_ser:	Single-thread image correlation function

Import_images:	Preprocesses filenames to open individual images, calls function to sort files into absolute numerical, rather than alphabetical, order
Munkres:	Actual Hungarian algorithm function called for Hungarianlinker (Tinevez, 2011, MatLab Central)
Nearestneighborlinker:	Uses nearest neighbor algorithm to link detected particles (Tinevez, 2011, MatLab Central)
Process_object:	Processes imported images to negative grayscale, thresholds images, masks images to remove non-central regions, and performs particle analysis on final image
Refresh_image:	For the UI, refreshes the image in the preview window with overlays and processing. Only called when image changed.
Simpletracker:	Overhead function for nearest neighbor and Hungarian algorithm tracking functions (Tinevez, 2011, MatLab Central)
Sort_nat:	Sorts files according to their natural order (File1, file2…file10, file11 instead of file1, file10, file11, file2…) (Schwarz, 2011, MatLab Central)
UI:	The main script that builds the user interface and calls the subfunctions of the program. UI references design of UI.fig file.

P. DESCRIPTION OF LABVIEW SUB-VIS

Step Resolution:	Changes the value of the step resolution for the duration of the VI
Initial Velocity:	Sets the initial, or ramping, velocity of the stepper motors
Slow Velocity:	Sets the slew, or constant, velocity of the stepper motors
Step Position:	Sets the step position of the stepper motors
Set Origin:	Sets the origin, or home position, of the stepper motors
Initialize:	Before the motors can be moved or motor properties can be set, the controllers must be placed in party mode, which allows the user to set properties and move multiple motors at once. This VI places the stepper motors in party mode
Linear Motion:	Moves the stepper motors a certain linear distance (in mm) set by the user
Data Acquisition:	Uses NI-DAQmx to read and create moving average of load voltage, converts to grams and Newtons
Marker Bounding:	Allows creation of image masks to select particles to track
Center of Mass Distance:	Tracks particle markers in real-time and calculates center of mass of each particle and where it has moved using nearest neighbor

Steps to MM:	Converts motor steps into millimeter displacements
Deformation Gradient:	Calculates deformation gradient of local strain from optical tracking based on reference configuration
Mechanical Test:	The main VI and user interface
Uniaxial:	Uniaxial testing protocol, uses independent motor code
Equibiaxial:	Equibiaxial testing protocol, uses independent motor code
Constant Stretch:	Constant stretch protocol, uses independent motor code

Q. LOAD CELL CALIBRATION

1. Weigh the following objects and record their weights: box & string, 1 200 gram weight and 4 500 gram weights. Determine the exact weights for every step of the calibration process.
   0 grams ~ 0 pounds
   200 grams ~ 0.5 pounds
   500 grams ~ 1 pound
   700 grams ~ 1.5 pounds
   1000 grams ~ 2 pounds
   1200 grams ~ 2.5 pounds
   1500 grams ~ 3 pounds
   1700 grams ~ 3.5 pounds
   2000 grams ~ 4 pounds
   2200 grams ~ 4.5 pounds

2. Open a blank VI in LabVIEW. In the block diagram, search for “DAQ Assistant” and place it into the block diagram. Follow the prompts that pop up on the screen:
   Acquire Signals
   Analog Input
   Bridge (V/V)
   cDAQmod1 (NI 9237)
   ai0 and ai1 (select both by holding shift and then clicking on ai0 and ai1)

3. Set the following values on the configuration tab of the channel settings for each channel selected in step one (should be ai0 and ai1).
   Signal Input Range
   Max: 25
   Min: -25
   Scaled Units: mV/V
   Bridge type: *Full*
   Vex (excitation voltage) source: *Internal*
   Vex Value: *5 V DC*
   Bridge Resistance: *500* Ω

4. Under “Bridge (V/V) Setup”, select the calibration tab and click “calibrate.” This will start the channel calibration wizard

5. Input your name
   Expiration date (need to decide how long these calibrations will be good for)
   After calibration expires, *do not apply the calibration and return an error*.
   Acquisition Attributes
   Number of samples to average: *25000*
   Sample rate (Hz): *25000*
   Additional Information
   Load Cell: *X or Y*
   Serial No: *X (1572180) or Y (1572181)*

6. Collect calibration measurement values. Tie string to box to place weights we have in lab (make sure to reweigh the weights after they are placed in the box) and box on the end of the load cell. Under the reference value, record the value for the weight of the weight itself and the string. Click “commit calibration value” and move onto the next weight. Allow five minutes between placing the weight at the end of the load cell and clicking “commit calibration value” so the uncalibrated voltage value can stabilize. Begin with no weight at the end of the load cell, and then increase the weight by the list in step 1 until you reach 2200 grams. While unloading the weights after reaching 2200 grams, allow 5 minutes for the load cell to equilibrate. Move back down the list in step one every time until you reach zero weight.

7. Open the excel file titled “Load Cell Calibration Template”. Copy and paste the load cell calibration data from the most recent calibration, and generate its chart and trend line. Input the weights and voltage values calculated and obtained throughout the calibration in the upper section of the sheet (you can fill this out as you go).

R. LOAD CELL CALIBRATION CHARTS

X-axis calibration			5 LB LOAD CELL
Load (g)	% full load	mV/V	Normalized mV/V
0	0.00	0.0074	0
78.97	3.48	0.0816	0.0742
98.98	4.36	0.1005	0.0931
109.01	4.81	0.1099	0.1025
279.04	12.30	0.2692	0.2618
579.07	25.53	0.5496	0.5422
779.14	34.35	0.7363	0.7289
1079.2	47.58	1.0157	1.0083
1279.27	56.41	1.2029	1.1955
1579.33	69.64	1.4821	1.4747
1779.4	78.46	1.6672	1.6598
2079.48	91.69	1.946	1.9386
1779.4	78.46	1.6671	1.6597
1579.33	69.64	1.481	1.4736
1279.27	56.41	1.2014	1.194
1079.2	47.58	1.0165	1.0091
779.14	34.35	0.7357	0.7283
578.07	25.49	0.5495	0.5421
279.04	12.30	0.2693	0.2619
109.01	4.81	0.1103	0.1029
98.98	4.36	0.1009	0.0935
78.97	3.48	0.0822	0.0748
0	0.00	0.0085	0.0011

Y-axis calibration			5 LB LOAD CELL
0	0.00	0.0159	0
78.97	3.48	0.0835	0.0676
98.98	4.36	0.1015	0.0856
109.01	4.81	0.1106	0.0947
279.04	12.30	0.2654	0.2495
579.07	25.53	0.5388	0.5229
779.14	34.35	0.7214	0.7055
1079.2	47.58	0.9959	0.98
1279.27	56.41	1.179	1.1631
1579.33	69.64	1.4523	1.4364
1779.4	78.46	1.6341	1.6182
2079.48	91.69	1.9055	1.8896
1779.4	78.46	1.6339	1.618
1579.33	69.64	1.4525	1.4366
1279.27	56.41	1.181	1.1651
1079.2	47.58	0.9993	0.9834
779.14	34.35	0.7267	0.7108
579.07	25.53	0.5446	0.5287
279.04	12.30	0.2718	0.2559
109.01	4.81	0.117	0.1011
98.98	4.36	0.1078	0.0919
78.97	3.48	0.0896	0.0737
0	0.00	0.0171	0.0012

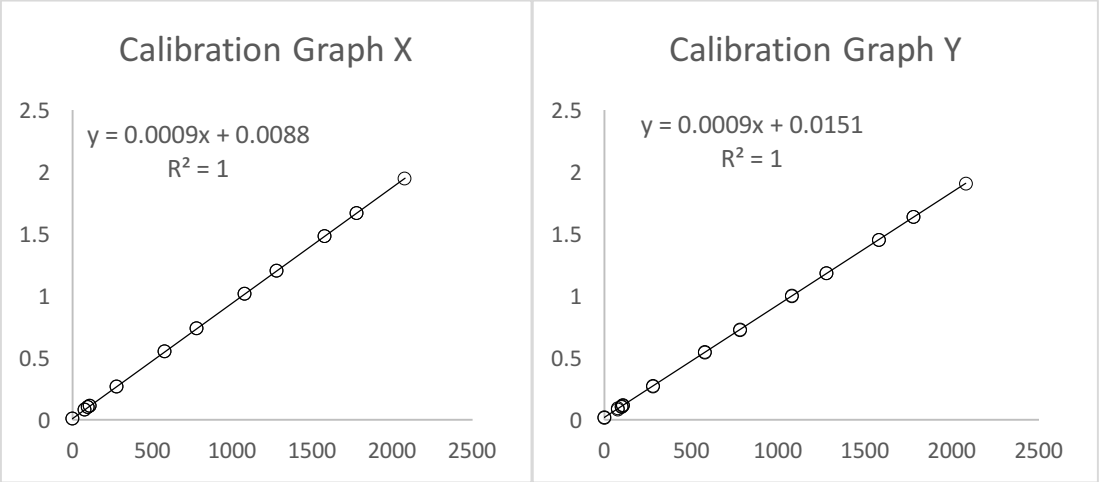

Y-axis: voltage ratio (mV/V); X-axis: load (g)

S. STATISTICAL TABLES FOR STRAIN VALIDATION

Paired t-Test: Reference and Tension

	Reference	*Tension*
Mean	659.4875	737.105
Variance	4221.793	4319.609367
Observations	4	4
Pearson Correlation	0.941167	
Hypothesized Mean Difference	0	
df	3	
t Stat	-6.92127	
P(T<=t) one-tail	0.003092	
t Critical one-tail	2.353363	
P(T<=t) two-tail	0.006183	
t Critical two-tail	3.182446	

Paired t-Test: Reference and Return to Reference

	Reference	*Return*
Mean	659.4875	658.9425
Variance	4221.793	4163.001758
Observations	4	4
Pearson Correlation	0.9683	
Hypothesized Mean Difference	0	
df	3	
t Stat	0.066832	
P(T<=t) one-tail	0.47546	
t Critical one-tail	2.353363	
P(T<=t) two-tail	0.95092	
t Critical two-tail	3.182446	

T. GRAPHS FROM MURINE PILOT STUDY

For load-displacement plots, colored dashed lines indicate data from Groves et al., while the solid black lines and markers indicate experimental loading and unloading curves

Load-Displacement Curves

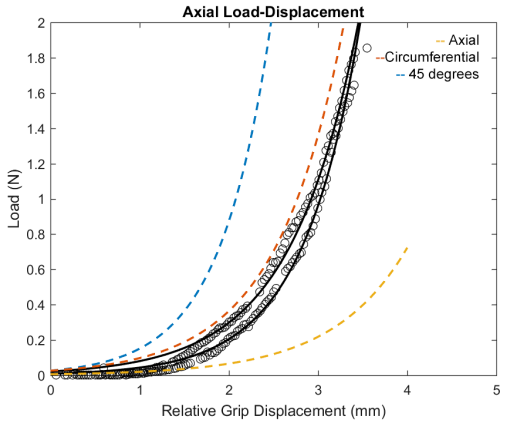

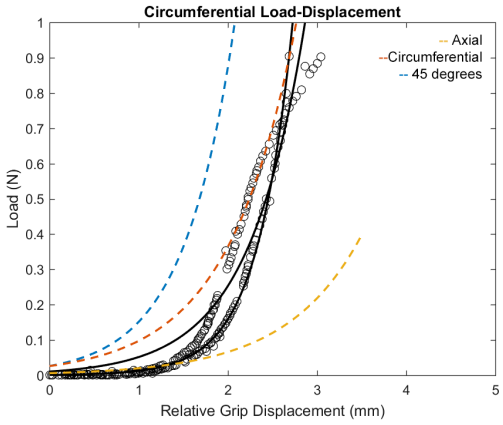

Sample 1

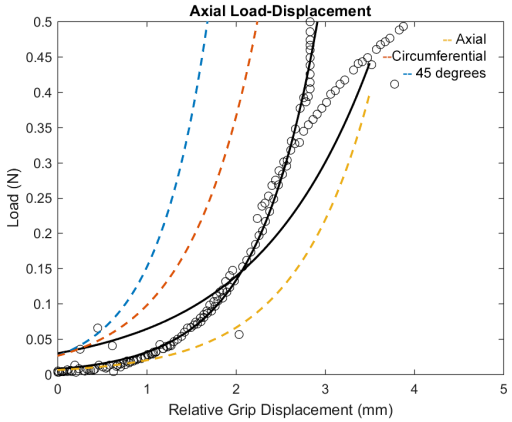

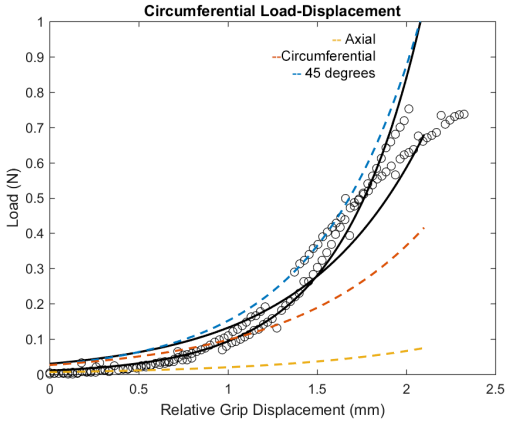

Sample 2

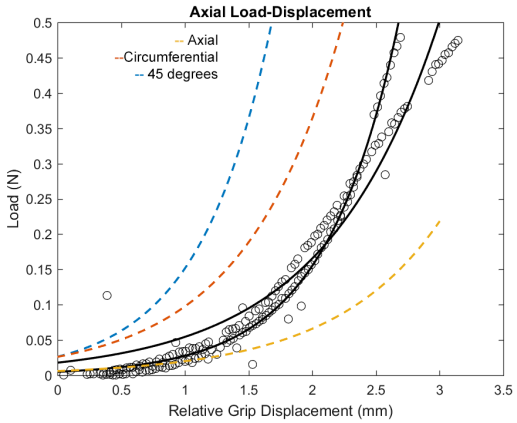

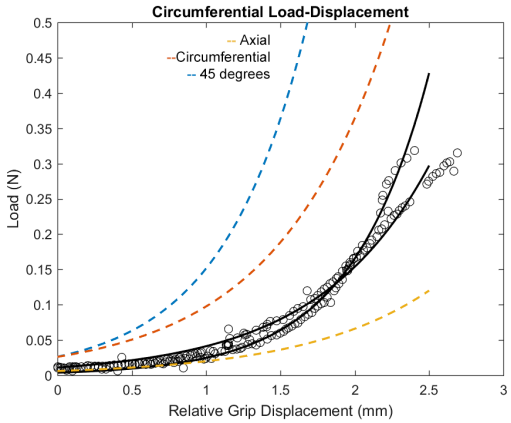

Sample 3

Stress-Strain Curves

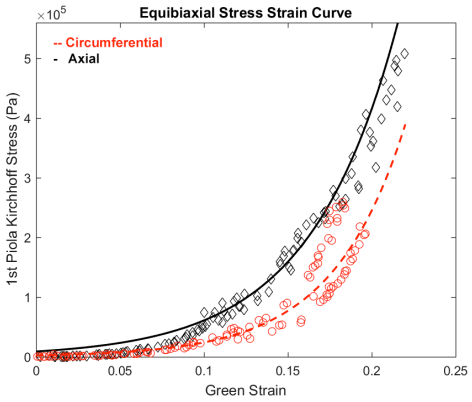

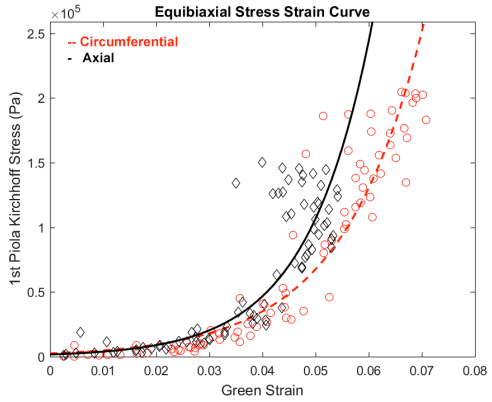

Sample 1 Sample 2

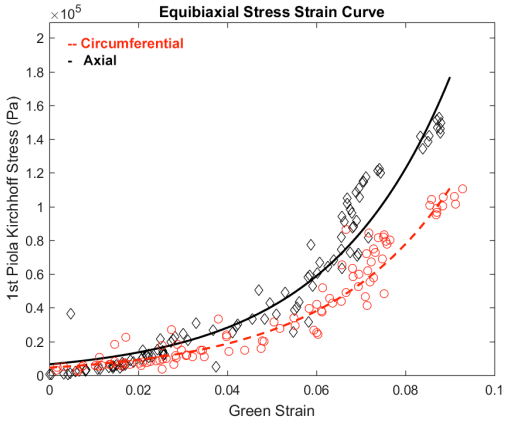

Sample 3

REFERENCES

Chapter 1

Avery, N.C., and A.J. Bailey. "Restraining Cross-Links Responsible for the Mechanical Properties of Collagen Fibers: Natural and Artificial." *Collagen.* Fratzl, Peter, ed. 2008. Boston, MA: Springer US. doi:10.1007/978-0-387-73906-9.

Baek, S., A. Valentín, and J. D. Humphrey. 2007. "Biochemomechanics of Cerebral Vasospasm and Its Resolution: II. Constitutive Relations and Model Simulations." *Annals of Biomedical Engineering* 35 (9): 1498. doi:10.1007/s10439-007-9322-x.

Bai, Yuqiang, Po-Feng Lee, Jay D. Humphrey, and Alvin T. Yeh. 2014. "Sequential Multimodal Microscopic Imaging and Biaxial Mechanical Testing of Living Multicomponent Tissue Constructs." *Annals of Biomedical Engineering* 42 (9): 1791–1805. doi:10.1007/s10439-014-1019-3.

Bass, E. C., F. A. Ashford, M. R. Segal, and J. C. Lotz. 2004. "Biaxial Testing of Human Annulus Fibrosus and Its Implications for a Constitutive Formulation." *Annals of Biomedical Engineering* 32 (9): 1231–42. doi:10.1114/B:ABME.0000039357.70905.94.

Bell, E. David, Rahul S. Kunjir, and Kenneth L. Monson. 2013. "Biaxial and Failure Properties of Passive Rat Middle Cerebral Arteries." *Journal of Biomechanics* 46 (1): 91–96. doi:10.1016/j.jbiomech.2012.10.015.

Caulk, Alexander W., Zhanna V. Nepiyushchikh, Ryan Shaw, J. Brandon Dixon, and Rudolph L. Gleason. 2015. "Quantification of the Passive and Active Biaxial Mechanical Behaviour and Microstructural Organization of Rat Thoracic Ducts." *Journal of The Royal Society Interface* 12 (108): 20150280. doi:10.1098/rsif.2015.0280.

Cooney, Gerard M., Spencer P. Lake, Dominic M. Thompson, Ryan M. Castile, Des C. Winter, and Ciaran K. Simms. 2016. "Uniaxial and Biaxial Tensile Stress–stretch Response of Human Linea Alba." *Journal of the Mechanical Behavior of Biomedical Materials* 63 (October): 134–40. doi:10.1016/j.jmbbm.2016.06.015.

Cooney, Gerard M., Kevin M. Moerman, Michael Takaza, Des C. Winter, and Ciaran K. Simms. 2015. "Uniaxial and Biaxial Mechanical Properties of Porcine Linea Alba." *Journal of the Mechanical Behavior of Biomedical Materials* 41 (January): 68–82. doi:10.1016/j.jmbbm.2014.09.026.

Eberth, J. F., L. Cardamone, and J. D. Humphrey. 2011. "Evolving Biaxial Mechanical Properties of Mouse Carotid Arteries in Hypertension." *Journal of Biomechanics* 44 (14): 2532–37. doi:10.1016/j.jbiomech.2011.07.018.

Ferruzzi, J., D. A. Vorp, and J. D. Humphrey. 2011. "On Constitutive Descriptors of the Biaxial Mechanical Behaviour of Human Abdominal Aorta and Aneurysms." *Journal of The Royal Society Interface* 8 (56): 435–50. doi:10.1098/rsif.2010.0299.

Flynn, Brendan P., Amit P. Bhole, Nima Saeidi, Melody Liles, Charles A. DiMarzio, and Jeffrey W. Ruberti. 2010. "Mechanical Strain Stabilizes Reconstituted Collagen Fibrils against Enzymatic Degradation by Mammalian Collagenase Matrix Metalloproteinase 8 (MMP-8)." *PLOS ONE* 5 (8): e12337. doi:10.1371/journal.pone.0012337.

Fratzl, Peter, ed. 2008. *Collagen*. Boston, MA: Springer US. doi:10.1007/978-0-387-73906-9.

Fung, Yuan-Cheng. 1993. *Biomechanics*. New York, NY: Springer New York. doi:10.1007/978-1-4757-2257-4.

Gleason, Rudolph L., Wendy W. Dye, Emily Wilson, and Jay D. Humphrey. 2008. “Quantification of the Mechanical Behavior of Carotid Arteries from Wild-Type, Dystrophin-Deficient, and Sarcoglycan-δ Knockout Mice.” *Journal of Biomechanics* 41 (15): 3213–18. doi:10.1016/j.jbiomech.2008.08.012.

Holzapfel, Gerhard A., and Thomas C. Gasser. 2001. “A Viscoelastic Model for Fiber-Reinforced Composites at Finite Strains: Continuum Basis, Computational Aspects and Applications.” *Computer Methods in Applied Mechanics and Engineering* 190 (34): 4379–4403. doi:10.1016/S0045-7825(00)00323-6.

Holzapfel, Gerhard A., Thomas C. Gasser, and Ray W. Ogden. 2000. “A New Constitutive Framework for Arterial Wall Mechanics and a Comparative Study of Material Models.” *Journal of Elasticity and the Physical Science of Solids* 61 (1–3): 1–48. doi:10.1023/A:1010835316564.

Hulmes, D.J.S. “Collagen Diversity, Synthesis and Assembly.” *Collagen.* Fratzl, Peter, ed. 2008. Boston, MA: Springer US. doi:10.1007/978-0-387-73906-9.

Humphrey, J. D. 2003. “Review Paper: Continuum Biomechanics of Soft Biological Tissues.” *Proceedings of the Royal Society of London A: Mathematical, Physical and Engineering Sciences* 459 (2029): 3–46. doi:10.1098/rspa.2002.1060.

Humphrey, J. D., and K. R. Rajagopal. 2002. “A Constrained Mixture Model for Growth and Remodeling of Soft Tissues.” *Mathematical Models and Methods in Applied Sciences* 12 (03): 407–30. doi:10.1142/S0218202502001714.

Humphrey, J. D., D.L. Vawter, and R.P. Vito. 1987. “Quantification of Strains in Biaxially Tested Soft Tissues.” *Journal of Biomechanics* 20 (1): 59–65.

Humphrey, Jay D., Eric R. Dufresne, and Martin A. Schwartz. 2014. “Mechanotransduction and Extracellular Matrix Homeostasis.” *Nature Reviews Molecular Cell Biology* 15 (12): 802–12. doi:10.1038/nrm3896.

Lanir, Y., and Y. C. Fung. 1974. “Two-Dimensional Mechanical Properties of Rabbit skin—I. Experimental System.” *Journal of Biomechanics* 7 (1): 29–34. doi:10.1016/0021-9290(74)90067-0.

Lapiere, Ch M., B. Nusgens, and G. E. Pierard. 1977. “Interaction Between Collagen Type I and Type III in Conditioning Bundles Organization.” *Connective Tissue Research* 5 (1): 21–29. doi:10.3109/03008207709152608.

Lee, Y. U., Y. Naito, H. Kurobe, C. K. Breuer, and J. D. Humphrey. 2013. “Biaxial Mechanical Properties of the Inferior Vena Cava in C57BL/6 and CB-17 SCID/Bg Mice.” *Journal of Biomechanics* 46 (13): 2277–82. doi:10.1016/j.jbiomech.2013.06.013.

Legerlotz, Kirsten, Jonas Dorn, Jens Richter, Martin Rausch, and Olivier Leupin. 2014. “Age-Dependent Regulation of Tendon Crimp Structure, Cell Length and Gap Width with Strain.” *Acta Biomaterialia* 10 (10): 4447–55. doi:10.1016/j.actbio.2014.05.029.

Mauri, Arabella, Steffen M. Zeisberger, Simon P. Hoerstrup, and Edoardo Mazza. 2013. “Analysis of the Uniaxial and Multiaxial Mechanical Response of a Tissue-Engineered Vascular Graft.” *Tissue Engineering Part A* 19 (5–6): 583–92. doi:10.1089/ten.tea.2012.0075.

Muñoz, M. J., J. A. Bea, J. F. Rodríguez, I. Ochoa, J. Grasa, A. Pérez del Palomar, P. Zaragoza, R. Osta, and M. Doblaré. 2008. “An Experimental Study of the Mouse Skin Behaviour: Damage and Inelastic Aspects.” Journal of Biomechanics 41 (1): 93–99. doi:10.1016/j.jbiomech.2007.07.013.

Nicholls, S. P., L. J. Gathereole, A. Keller, and J. S. Shah. 1983. “Crimping in Rat Tail Tendon Collagen: Morphology and Transverse Mechanical Anisotropy.” *International Journal of Biological Macromolecules* 5 (5): 283–88. doi:10.1016/0141-8130(83)90043-0.

O’Connell, Grace D., Heather L. Guerin, and Dawn M. Elliott. 2009. “Theoretical and Uniaxial Experimental Evaluation of Human Annulus Fibrosus Degeneration.” *Journal of Biomechanical Engineering* 131 (11): 111007-111007–7. doi:10.1115/1.3212104.

Rassoli, Aisa, Mohammad Shafigh, Amirsaeed Seddighi, Afsoun Seddighi, Hamidreza Daneshparvar, and Nasser Fatouraee. 2014. “Biaxial Mechanical Properties of Human Ureter under Tension.” *Urology Journal* 11 (3): 1678–86.

Sacks, Michael S. 2000. “Biaxial Mechanical Evaluation of Planar Biological Materials.” *Journal of Elasticity and the Physical Science of Solids* 61 (1–3): 199. doi:10.1023/A:1010917028671.

Sander, E. A., V. H. Barocas, and R. T. Tranquillo. 2011. “Initial Fiber Alignment Pattern Alters Extracellular Matrix Synthesis in Fibroblast-Populated Fibrin Gel Cruciforms and Correlates with Predicted Tension.” *Annals of Biomedical Engineering* 39 (2): 714–29. doi:10.1007/s10439-010-0192-2.

Screen, H. R. C., D. A. Lee, D. L. Bader, and J. C. Shelton. 2003. “Development of a Technique to Determine Strains in Tendons Using the Cell Nuclei.” *Biorheology* 40 (1–3): 361–68.

Sokolis, Dimitrios P., Despoina C. Petsepe, Stavroula A. Papadodima, and Stavros K. Kourkoulis. 2017. “Age- and Region-Related Changes in the Biomechanical Properties and Composition of the Human Ureter.” *Journal of Biomechanics* 51 (January): 57–64. doi:10.1016/j.jbiomech.2016.11.067.

Sommer, Gerhard, Peter Regitnig, Lukas Költringer, and Gerhard A. Holzapfel. 2010. “Biaxial Mechanical Properties of Intact and Layer-Dissected Human Carotid Arteries at Physiological and Supraphysiological Loadings.” *American Journal of Physiology - Heart and Circulatory Physiology* 298 (3): H898–912. doi:10.1152/ajpheart.00378.2009.

Sun, Wei, Michael S. Sacks, Tiffany L. Sellaro, William S. Slaughter, and Michael J. Scott. 2003. “Biaxial Mechanical Response of Bioprosthetic Heart Valve Biomaterials to High In-Plane Shear.” *Journal of Biomechanical Engineering* 125 (3): 372–80. doi:10.1115/1.1572518.

Szczesny, Spencer E., John M. Peloquin, Daniel H. Cortes, Jennifer A. Kadlowec, Louis J. Soslowsky, and Dawn M. Elliott. 2012. “Biaxial Tensile Testing and Constitutive Modeling of Human Supraspinatus Tendon.” *Journal of Biomechanical Engineering* 134 (2): 021004-021004-9. doi:10.1115/1.4005852.

Tong, Pin, and Yuang-Cheng Fung. 1976. “The Stress-Strain Relationship for the Skin.” *Journal of Biomechanics* 9 (10): 649–57. doi:10.1016/0021-9290(76)90107-X.

Waldman, Stephen D., and J. Michael Lee. 2002. “Boundary Conditions during Biaxial Testing of Planar Connective Tissues. Part 1: Dynamic Behavior.” *Journal of Materials Science: Materials in Medicine* 13 (10): 933–38. doi:10.1023/A:1019896210320.

Chapter 2

Azadani, Ali N., Sam Chitsaz, Alex Mannion, Aart Mookhoek, Andrew Wisneski, Julius M. Guccione, Michael D. Hope, Liang Ge, and Elaine E. Tseng. 2013. “Biomechanical Properties of Human Ascending Thoracic Aortic Aneurysms.” *The Annals of Thoracic Surgery* 96 (1): 50–58. doi:10.1016/j.athoracsur.2013.03.094.

Barone, William R., Andrew J. Feola, Pamela A. Moalli, and Steven D. Abramowitch. 2012. “The Effect of Pregnancy and Postpartum Recovery on the Viscoelastic Behavior of the Rat Cervix.” *Journal of Mechanics in Medicine & Biology* 12 (1): 1250009–1.

Becker, Winston R., and Raffaella De Vita. 2015. “Biaxial Mechanical Properties of Swine Uterosacral and Cardinal Ligaments.” *Biomechanics and Modeling in Mechanobiology* 14 (3): 549–60. doi:10.1007/s10237-014-0621-5.

Bell, B. J., E. Nauman, and S. L. Voytik-Harbin. 2012. “Multiscale Strain Analysis of Tissue Equivalents Using a Custom-Designed Biaxial Testing Device.” *Biophysical Journal* 102 (6): 1303–12. doi:10.1016/j.bpj.2012.02.007.

Caulk, Alexander W., Zhanna V. Nepiyushchikh, Ryan Shaw, J. Brandon Dixon, and Rudolph L. Gleason. 2015. “Quantification of the Passive and Active Biaxial Mechanical Behaviour and

Microstructural Organization of Rat Thoracic Ducts." *Journal of The Royal Society Interface* 12 (108): 20150280. doi:10.1098/rsif.2015.0280.

Connizzo, Brianne K., Joseph J. Sarver, Lin Han, and Louis J. Soslowsky. 2014. "In Situ Fibril Stretch and Sliding Is Location-Dependent in Mouse Supraspinatus Tendons." *Journal of Biomechanics* 47 (16): 3794–98. doi:10.1016/j.jbiomech.2014.10.029.

Fan, Rong, and Michael S. Sacks. 2014. "Simulation of Planar Soft Tissues Using a Structural Constitutive Model: Finite Element Implementation and Validation." *Journal of Biomechanics*, Functional Tissue Engineering, 47 (9): 2043–54. doi:10.1016/j.jbiomech.2014.03.014.

Gregory, Diane E., and Jack P. Callaghan. 2011. "A Comparison of Uniaxial and Biaxial Mechanical Properties of the Annulus Fibrosus: A Porcine Model." *Journal of Biomechanical Engineering* 133 (2): 024503-024503-5. doi:10.1115/1.4003327.

Holzapfel, Gerhard A., and Ray W. Ogden. 2009. "On Planar Biaxial Tests for Anisotropic Nonlinearly Elastic Solids. A Continuum Mechanical Framework." *Mathematics and Mechanics of Solids* 14 (5): 474–89. doi:10.1177/1081286507084411.

Hu, J.-J., G.-W. Chen, Y.-C. Liu, and S.-S. Hsu. 2014. "Influence of Specimen Geometry on the Estimation of the Planar Biaxial Mechanical Properties of Cruciform Specimens." *Experimental Mechanics* 54 (4): 615–31. doi:10.1007/s11340-013-9826-2.

Humphrey, J. D., D.L. Vawter, and R.P. Vito. 1987. "Quantification of Strains in Biaxially Tested Soft Tissues." *Journal of Biomechanics* 20 (1): 59–65.

Jacobs, Nathan T., Daniel H. Cortes, Edward J. Vresilovic, and Dawn M. Elliott. 2013. "Biaxial Tension of Fibrous Tissue: Using Finite Element Methods to Address Experimental Challenges Arising From Boundary Conditions and Anisotropy." *Journal of Biomechanical Engineering* 135 (2): 021004-021004-10. doi:10.1115/1.4023503.

Jimenez, M. L., T. D. Brown, and R. A. Brand. 1989. "The Effects of Grip Proximity on Perceived Local in Vitro Tendon Strain." *Journal of Biomechanics* 22 (8–9): 949–55.

Lally, C., A. J. Reid, and P. J. Prendergast. 2004. "Elastic Behavior of Porcine Coronary Artery Tissue Under Uniaxial and Equibiaxial Tension." *Annals of Biomedical Engineering* 32 (10): 1355–64. doi:10.1114/B:ABME.0000042224.23927.ce.

Lanir, Y., and Y. C. Fung. 1974. "Two-Dimensional Mechanical Properties of Rabbit skin—I. Experimental System." *Journal of Biomechanics* 7 (1): 29–34. doi:10.1016/0021-9290(74)90067-0.

Legerlotz, Kirsten, Jonas Dorn, Jens Richter, Martin Rausch, and Olivier Leupin. 2014. "Age-Dependent Regulation of Tendon Crimp Structure, Cell Length and Gap Width with Strain." *Acta Biomaterialia* 10 (10): 4447–55. doi:10.1016/j.actbio.2014.05.029.

Lin, Tony W. 2004. "Development and Utilization of a Transgenic Mouse Injury Model to Investigate the Role of Interleukin-4 and Interleukin-6 in Tendon Healing." *Dissertations Available from ProQuest*, January, 1–229.

Love, A. E. H. (Augustus Edward Hough). 1906. *A Treatise on the Mathematical Theory of Elasticity*. 2nd ed. Cambridge University Press. http://archive.org/details/atreatiseonmath01lovegoog.

Lyons, Mathew, Des C. Winter, and Ciaran K. Simms. 2014. "Mechanical Characterisation of Porcine Rectus Sheath under Uniaxial and Biaxial Tension." *Journal of Biomechanics* 47 (8): 1876–84. doi:10.1016/j.jbiomech.2014.03.009.

Manoogian, Sarah J., Jill A. Bisplinghoff, Andrew R. Kemper, and Stefan M. Duma. 2012. "Dynamic Material Properties of the Pregnant Human Uterus." *Journal of Biomechanics* 45 (9): 1724–27. doi:10.1016/j.jbiomech.2012.04.001.

Manoogian, Sarah J., Craig McNally, Joel D. Stitzel, and Stefan M. Duma. 2008. "Dynamic Biaxial Tissue Properties of Pregnant Porcine Uterine Tissue." *Stapp Car Crash Journal* 52 (November): 167–85.

Mondragon, Eli, Ph D. Kristin Myers, and M. S. Kyoko Yoshida. 2017. "Characterizing the Biomechanical and Biochemical Properties of Mouse Uterine Tissue." *Columbia Undergraduate Science Journal* 7 (2013).

Nolan, D. R., and J. P. McGarry. 2016. "On the Correct Interpretation of Measured Force and Calculation of Material Stress in Biaxial Tests." *Journal of the Mechanical Behavior of Biomedical Materials* 53 (January): 187–99. doi:10.1016/j.jmbbm.2015.08.019.

Omari, Eenas A., Tomy Varghese, Mark A. Kliewer, Josephine Harter, and Ellen M. Hartenbach. 2015. "Dynamic and Quasi-Static Mechanical Testing for Characterization of the Viscoelastic Properties of Human Uterine Tissue." *Journal of Biomechanics* 48 (10): 1730–36. doi:10.1016/j.jbiomech.2015.05.013.

Röhrnbauer, B., Y. Ozog, J. Egger, E. Werbrouck, J. Deprest, and E. Mazza. 2013. "Combined Biaxial and Uniaxial Mechanical Characterization of Prosthetic Meshes in a Rabbit Model." *Journal of Biomechanics* 46 (10): 1626–32. doi:10.1016/j.jbiomech.2013.04.015.

Rubod, Chrystèle, Malik Boukerrou, Mathias Brieu, Patrick Dubois, and Michel Cosson. 2007. "Biomechanical Properties of Vaginal Tissue. Part 1: New Experimental Protocol." *The Journal of Urology* 178 (1): 320–25. doi:10.1016/j.juro.2007.03.040.

Sacks, Michael S. 2000. "Biaxial Mechanical Evaluation of Planar Biological Materials." *Journal of Elasticity and the Physical Science of Solids* 61 (1–3): 199. doi:10.1023/A:1010917028671.

Sacks, Michael S., and C. J. Chuong. 1998. "Orthotropic Mechanical Properties of Chemically Treated Bovine Pericardium." *Annals of Biomedical Engineering* 26 (5): 892–902. doi:10.1114/1.135.

Sacks, Michael S., and Wei Sun. 2003. "Multiaxial Mechanical Behavior of Biological Materials." *Annual Review of Biomedical Engineering* 5 (1): 251–84.

Screen, H. R. C., D. A. Lee, D. L. Bader, and J. C. Shelton. 2003. "Development of a Technique to Determine Strains in Tendons Using the Cell Nuclei." *Biorheology* 40 (1–3): 361–68.

Shetye, Snehal S., Matthew M. Deault, and Christian M. Puttlitz. 2014. "Biaxial Response of Ovine Spinal Cord Dura Mater." *Journal of the Mechanical Behavior of Biomedical Materials* 34 (June): 146–53. doi:10.1016/j.jmbbm.2014.02.014.

Stäubli, H. U., L. Schatzmann, P. Brunner, L. Rincón, and L. P. Nolte. 1999. "Mechanical Tensile Properties of the Quadriceps Tendon and Patellar Ligament in Young Adults." *The American Journal of Sports Medicine* 27 (1): 27–34. doi:10.1177/03635465990270011301.

Sun, Wei, Michael S. Sacks, and Michael J. Scott. 2005. "Effects of Boundary Conditions on the Estimation of the Planar Biaxial Mechanical Properties of Soft Tissues." *Journal of Biomechanical Engineering* 127 (4): 709–15. doi:10.1115/1.1933931.

Szczesny, Spencer E., John M. Peloquin, Daniel H. Cortes, Jennifer A. Kadlowec, Louis J. Soslowsky, and Dawn M. Elliott. 2012. "Biaxial Tensile Testing and Constitutive Modeling of Human Supraspinatus Tendon." *Journal of Biomechanical Engineering* 134 (2): 021004-021004-9. doi:10.1115/1.4005852.

Waldman, S. D., M. S. Sacks, and J. M. Lee. 2002. "Boundary Conditions during Biaxial Testing of Planar Connective Tissues Part II Fiber Orientation." *Journal of Materials Science Letters* 21 (15): 1215–21. doi:10.1023/A:1016576603938.

Waldman, Stephen D., and J. Michael Lee. 2002. "Boundary Conditions during Biaxial Testing of Planar Connective Tissues. Part 1: Dynamic Behavior." *Journal of Materials Science: Materials in Medicine* 13 (10): 933–38. doi:10.1023/A:1019896210320.

Zhang, Will, Yuan Feng, Chung-Hao Lee, Kristen L. Billiar, and Michael S. Sacks. 2015. "A Generalized Method for the Analysis of Planar Biaxial Mechanical Data Using Tethered Testing Configurations." *Journal of Biomechanical Engineering* 137 (6): 064501-064501-13. doi:10.1115/1.4029266.

Zhao, X., Z. C. Berwick, J. F. Krieger, H. Chen, S. Chambers, and G. S. Kassab. 2014. "Novel Design of Cruciform Specimens for Planar Biaxial Testing of Soft Materials." *Experimental Mechanics* 54 (3): 343–56. doi:10.1007/s11340-013-9808-4.

Chapter 3

Armentano, Ricardo L., Daniel Bia Santana, Edmundo I. Cabrera Fischer, Sebastián Graf, Héctor Pérez Cámpos, Yanina Zócalo Germán, Maria del Carmen Saldías, and Inés Alvarez. 2006. "An in Vitro Study of Cryopreserved and Fresh Human Arteries: A Comparison with ePTFE Prostheses and Human Arteries Studied Non-Invasively in Vivo." *Cryobiology* 52 (1): 17–26. doi:10.1016/j.cryobiol.2005.09.001.

Avery, N.C., and A.J. Bailey. "Restraining Cross-Links Responsible for the Mechanical Properties of Colalgen Fibers: Natural and Artificial." *Collagen*. Fratzl, Peter, ed. 2008. Boston, MA: Springer US. doi:10.1007/978-0-387-73906-9.

Butler, David L., Edward S. Grood, Frank R. Noyes, Ronald F. Zernicke, and Kim Brackett. 1984. "Effects of Structure and Strain Measurement Technique on the Material Properties of Young Human Tendons and Fascia." *Journal of Biomechanics* 17 (8): 579–96. doi:10.1016/0021-9290(84)90090-3.

Clark, J. A., J. C. Y. Cheng, and K. S. Leung. 1996. "Mechanical Properties of Normal Skin and Hypertrophic Scars." *Burns* 22 (6): 443–446.

Del Prete, Z., S. Antoniucci, A. H. Hoffman, and P. Grigg. 2004. "Viscoelastic Properties of Skin in Mov-13 and Tsk Mice." *Journal of Biomechanics* 37 (10): 1491–97. doi:10.1016/j.jbiomech.2004.01.015.

Fratzl, Peter, ed. 2008. *Collagen*. Boston, MA: Springer US. doi:10.1007/978-0-387-73906-9.

Fung, Yuan-Cheng. 1993. *Biomechanics*. New York, NY: Springer New York. doi:10.1007/978-1-4757-2257-4.

Groves, Rachel B., Sion A. Coulman, James C. Birchall, and Sam L. Evans. 2013. "An Anisotropic, Hyperelastic Model for Skin: Experimental Measurements, Finite Element Modelling and Identification of Parameters for Human and Murine Skin." *Journal of the Mechanical Behavior of Biomedical Materials* 18 (February): 167–80. doi:10.1016/j.jmbbm.2012.10.021.

Holzapfel, G. A. 2000. "Biomechanics of Soft Tissue." In *Handbook of Material Behavior: Nonlinear Models and Properties*, edited by Jean Lamaitre. Academic Press.

Hulmes, D.J.S., "Collagen Diversity, Synthesis and Assembly." *Collagen*. Fratzl, Peter, ed. 2008. Boston, MA: Springer US. doi:10.1007/978-0-387-73906-9.

Humphrey, J. D., D.L. Vawter, and R.P. Vito. 1987. "Quantification of Strains in Biaxially Tested Soft Tissues." *Journal of Biomechanics* 20 (1): 59–65.

Karimi, Alireza, Mahdi Navidbakhsh, Maedeh Haghighatnama, and Afsaneh Motevalli Haghi. 2015. "Determination of the Axial and Circumferential Mechanical Properties of the Skin Tissue Using Experimental Testing and Constitutive Modeling." *Computer Methods in Biomechanics and Biomedical Engineering* 18 (16): 1768–74. doi:10.1080/10255842.2014.961441.

Karimi, Alireza, Seyyed Mohammadali Rahmati, and Mahdi Navidbakhsh. 2015. "Mechanical Characterization of the Rat and Mice Skin Tissues Using Histostructural and Uniaxial Data." *Bioengineered* 6 (3): 153–60. doi:10.1080/21655979.2015.1036202.

Lanir, Y., and Y. C. Fung. 1974. "Two-Dimensional Mechanical Properties of Rabbit skin—I. Experimental System." *Journal of Biomechanics* 7 (1): 29–34. doi:10.1016/0021-9290(74)90067-0.

Lee, Y. U., Y. Naito, H. Kurobe, C. K. Breuer, and J. D. Humphrey. 2013. "Biaxial Mechanical Properties of the Inferior Vena Cava in C57BL/6 and CB-17 SCID/Bg Mice." *Journal of Biomechanics* 46 (13): 2277–82. doi:10.1016/j.jbiomech.2013.06.013.

Martin, Paul. 1997. "Wound Healing--Aiming for Perfect Skin Regeneration." *Science* 276 (5309): 75–81. doi:10.1126/science.276.5309.75.

Mays, Peter K., Jill E. Bishop, and Geoffrey J. Laurent. 1988. "Age-Related Changes in the Proportion of Types I and III Collagen." *Mechanisms of Ageing and Development* 45 (3): 203–12. doi:10.1016/0047-6374(88)90002-4.

Moore, Keith L., Anne M. R. Agur, and Arthur Dalley. 2014. *Essential Clinical Anatomy*. 5th ed. Philadelphia: LWW.

Muñoz, M. J., J. A. Bea, J. F. Rodríguez, I. Ochoa, J. Grasa, A. Pérez del Palomar, P. Zaragoza, R. Osta, and M. Doblaré. 2008. "An Experimental Study of the Mouse Skin Behaviour: Damage and Inelastic Aspects." *Journal of Biomechanics* 41 (1): 93–99. doi:10.1016/j.jbiomech.2007.07.013.

Sacks, Michael S., and C. J. Chuong. 1998. "Orthotropic Mechanical Properties of Chemically Treated Bovine Pericardium." *Annals of Biomedical Engineering* 26 (5): 892–902. doi:10.1114/1.135.

Silver, Frederick H. 2006. *Mechanosensing and Mechanochemical Transduction in Extracellular Matrix*. New York, NY: Springer US. doi:10.1007/978-0-387-28176-6.

Silver, F.H., and W.J. Landis. "Viscoelasticity, Energy Storage and Transmission and Dissipation by Extracellular Matrices in Vertebrates." *Collagen*. Fratzl, Peter, ed. 2008. Boston, MA: Springer US. doi:10.1007/978-0-387-73906-9.

Tepole, Adrián Buganza, Michael Gart, Chad A. Purnell, Arun K. Gosain, and Ellen Kuhl. 2015. "Multi-View Stereo Analysis Reveals Anisotropy of Prestrain, Deformation, and Growth in Living Skin." *Biomechanics and Modeling in Mechanobiology* 14 (5): 1007–19. doi:10.1007/s10237-015-0650-8.

Vande Geest, Jonathan P., Michael S. Sacks, and David A. Vorp. 2006. "The Effects of Aneurysm on the Biaxial Mechanical Behavior of Human Abdominal Aorta." *Journal of Biomechanics* 39 (7): 1324–34. doi:10.1016/j.jbiomech.2005.03.003.

Veronda, D. R., and R. A. Westmann. 1970. "Mechanical Characterization of skin—Finite Deformations." *Journal of Biomechanics* 3 (1): 111–24. doi:10.1016/0021-9290(70)90055-2.

Waldman, Stephen D., and J. Michael Lee. 2002. "Boundary Conditions during Biaxial Testing of Planar Connective Tissues. Part 1: Dynamic Behavior." *Journal of Materials Science: Materials in Medicine* 13 (10): 933–38. doi:10.1023/A:1019896210320.

Chapter 4.1

Akins, Meredith L., Katherine Luby-Phelps, Ruud A. Bank, and Mala Mahendroo. 2011. "Cervical Softening During Pregnancy: Regulated Changes in Collagen Cross-Linking and Composition of Matricellular Proteins in the Mouse." *Biology of Reproduction* 84 (5): 1053–62. doi:10.1095/biolreprod.110.089599.

American College of Obstetricians and Gynecologists. 2014. "ACOG Practice Bulletin No.142: Cerclage for the Management of Cervical Insufficiency." *Obstetrics and Gynecology* 123 (2 Pt 1): 372–79. doi:10.1097/01.AOG.0000443276.68274.cc.

Aspden, Richard M. 1988. "Collagen Organisation in the Cervix and Its Relation to Mechanical Function." *Collagen and Related Research* 8 (2): 103–12. doi:10.1016/S0174-173X(88)80022-0.

Baah-Dwomoh, Adwoa, Jeffrey McGuire, Ting Tan, and Raffaella De Vita. 2016. "Mechanical Properties of Female Reproductive Organs and Supporting Connective Tissues: A Review of the Current State of Knowledge." *Applied Mechanics Reviews* 68 (6): 060801-060801-12. doi:10.1115/1.4034442.

Baek, S., A. Valentín, and J. D. Humphrey. 2007. "Biochemomechanics of Cerebral Vasospasm and Its Resolution: II. Constitutive Relations and Model Simulations." *Annals of Biomedical Engineering* 35 (9): 1498. doi:10.1007/s10439-007-9322-x.

Barone, William R., Andrew J. Feola, Pamela A. Moalli, and Steven D. Abramowitch. 2012. "The Effect of Pregnancy and Postpartum Recovery on the Viscoelastic Behavior of the Rat Cervix." *Journal of Mechanics in Medicine & Biology* 12 (1): 1250009–1.

Beck, Stacy, Daniel Wojdyla, Lale Say, Ana Pilar Betran, Mario Merialdi, Jennifer Harris Requejo, Craig Rubens, Ramkumar Menon, and Paul F. A. Van Look. 2010. "The Worldwide Incidence of Preterm Birth." *Bulletin of the World Health Organization* 88 (1): 31–38. doi:10.2471/BLT.08.062554.

Brosens, J. J., F. G. Barker, and N. M. deSouza. 1998. "Myometrial Zonal Differentiation and Uterine Junctional Zone Hyperplasia in the Non-Pregnant Uterus." *Human Reproduction Update* 4 (5): 496–502. doi:10.1093/humupd/4.5.496.

Brown, H. K., B. S. Stoll, S. V. Nicosia, J. V. Fiorica, P. S. Hambley, L. P. Clarke, and M. L. Silbiger. 1991. "Uterine Junctional Zone: Correlation between Histologic Findings and MR Imaging." *Radiology* 179 (2): 409–13. doi:10.1148/radiology.179.2.1707545.

Buhimschi, Irina A., Laure Dussably, Catalin S. Buhimschi, Asif Ahmed, and Carl P. Weiner. 2004. "Physical and Biomechanical Characteristics of Rat Cervical Ripening Are Not Consistent with Increased Collagenase Activity." *American Journal of Obstetrics and Gynecology* 191 (5): 1695–1704. doi:10.1016/j.ajog.2004.03.080.

Chard, T., and Jurgis Gediminas Grudzinskas. 1994. *The Uterus*. Cambridge University Press.

Conrad, John T., Wayne L. Johnson, William K. Kuhn, and Charles A. Hunter. 1966. "Passive Stretch Relationships in Human Uterine Muscle." *American Journal of Obstetrics & Gynecology* 96 (8): 1055–59. doi:10.1016/0002-9378(66)90513-8.

Csapo, A., T. Erdos, C. R. de Mattos, E. Gramss, and C. Moscowitz. 1965. "Stretch-Induced Uterine Growth, Protein Synthesis and Function." *Nature* 207 (5004): 1378–79. doi:10.1038/2071378a0.

deSouza, N M, I C Hawley, J E Schwieso, D J Gilderdale, and W P Soutter. 1994. "The Uterine Cervix on in Vitro and in Vivo MR Images: A Study of Zonal Anatomy and Vascularity Using an Enveloping Cervical Coil." *American Journal of Roentgenology* 163 (3): 607–12. doi:10.2214/ajr.163.3.8079853.

Ferruzzi, J., D. A. Vorp, and J. D. Humphrey. 2011. "On Constitutive Descriptors of the Biaxial Mechanical Behaviour of Human Abdominal Aorta and Aneurysms." *Journal of The Royal Society Interface* 8 (56): 435–50. doi:10.1098/rsif.2010.0299.

Gleason, Rudolph L., Wendy W. Dye, Emily Wilson, and Jay D. Humphrey. 2008. "Quantification of the Mechanical Behavior of Carotid Arteries from Wild-Type, Dystrophin-Deficient, and Sarcoglycan-δ Knockout Mice." *Journal of Biomechanics* 41 (15): 3213–18. doi:10.1016/j.jbiomech.2008.08.012.

Goldenberg, Robert L., Jennifer F. Culhane, Jay D. Iams, and Roberto Romero. 2008. "Epidemiology and Causes of Preterm Birth." *The Lancet* 371 (9606): 75–84. doi:10.1016/S0140-6736(08)60074-4.

Gonzalez, Juan M., Zhong Dong, Roberto Romero, and Guillermina Girardi. 2011. "Cervical Remodeling/Ripening at Term and Preterm Delivery: The Same Mechanism Initiated by Different Mediators and Different Effector Cells." *PLOS ONE* 6 (11): e26877. doi:10.1371/journal.pone.0026877.

Goranova, V., E. Vizza, S. Correr, R. Heyn, and P. M. Motta. 1996. "Collagen Fibrillar Skeleton in Pregnant Rabbit Endometrium at Term: A SEM Study after NaOH Maceration." *Archives of Histology and Cytology* 59 (2): 127–35.

Gupta, K. B., M. B. Ratcliffe, M. A. Fallert, L. H. Edmunds, and D. K. Bogen. 1994. "Changes in Passive Mechanical Stiffness of Myocardial Tissue with Aneurysm Formation." *Circulation* 89 (5): 2315–26. doi:10.1161/01.CIR.89.5.2315.

Harkness, Margaret L. R., and R. D. Harkness. 1954. "The Collagen Content of the Reproductive Tract of the Rat during Pregnancy and Lactation." *The Journal of Physiology* 123 (3): 492–500. doi:10.1113/jphysiol.1954.sp005066.

Holzapfel, Gerhard A., Thomas C. Gasser, and Ray W. Ogden. 2000. "A New Constitutive Framework for Arterial Wall Mechanics and a Comparative Study of Material Models." *Journal of Elasticity and the Physical Science of Solids* 61 (1–3): 1–48. doi:10.1023/A:1010835316564.

Humphrey, Jay D., Eric R. Dufresne, and Martin A. Schwartz. 2014. "Mechanotransduction and Extracellular Matrix Homeostasis." *Nature Reviews Molecular Cell Biology* 15 (12): 802–12. doi:10.1038/nrm3896.

Iams, Jay D. 2003. "Prediction and Early Detection of Preterm Labor." *Obstetrics and Gynecology* 101 (2): 402–12.

IWAHASHI, MASAAKI, and YASUTERU MURAGAKI. 2011. "Decreased Type III Collagen Expression in Human Uterine Cervix of Prolapse Uteri." *Experimental and Therapeutic Medicine* 2 (2): 271–74. doi:10.3892/etm.2011.204.

Iwahashi, Masaaki, Yasuteru Muragaki, Akira Ooshima, and Naohiko Umesaki. 2003. "Decreased Type I Collagen Expression in Human Uterine Cervix during Pregnancy." *The Journal of Clinical Endocrinology & Metabolism* 88 (5): 2231–35. doi:10.1210/jc.2002-021213.

Kokenyesi, Robert, Lucas C. Armstrong, Azin Agah, Raul Artal, and Paul Bornstein. 2004. "Thrombospondin 2 Deficiency in Pregnant Mice Results in Premature Softening of the Uterine Cervix." *Biology of Reproduction* 70 (2): 385–90. doi:10.1095/biolreprod.102.014704.

Lee, Y. U., Y. Naito, H. Kurobe, C. K. Breuer, and J. D. Humphrey. 2013. "Biaxial Mechanical Properties of the Inferior Vena Cava in C57BL/6 and CB-17 SCID/Bg Mice." *Journal of Biomechanics* 46 (13): 2277–82. doi:10.1016/j.jbiomech.2013.06.013.

Leppert, Phyllis C., Joseph M. Cerreta, and Ines Mandl. 1986. "Orientation of Elastic Fibers in the Human Cervix." *American Journal of Obstetrics & Gynecology* 155 (1): 219–24. doi:10.5555/uri:pii:0002937886901158.

Lindnér, P., A. Mattiasson, L. Persson, and B. Uvelius. 1988. "Reversibility of Detrusor Hypertrophy and Hyperplasia after Removal of Infravesical Outflow Obstruction in the Rat." *The Journal of Urology* 140 (3): 642–46.

Ludmir, J., and H. M. Sehdev. 2000. "Anatomy and Physiology of the Uterine Cervix." *Clinical Obstetrics and Gynecology* 43 (3): 433–39.

Mahmoud, Hussam, Amy Wagoner Johnson, Edward K. Chien, Michael J. Poellmann, and Barbara McFarlin. 2013. "System-Level Biomechanical Approach for the Evaluation of Term and Preterm Pregnancy Maintenance." *Journal of Biomechanical Engineering* 135 (2): 021009-021009-11. doi:10.1115/1.4023486.

Manoogian, Sarah J., Jill A. Bisplinghoff, Andrew R. Kemper, and Stefan M. Duma. 2012. "Dynamic Material Properties of the Pregnant Human Uterus." *Journal of Biomechanics* 45 (9): 1724–27. doi:10.1016/j.jbiomech.2012.04.001.

Marlow, Neil, Dieter Wolke, Melanie A. Bracewell, and Muthanna Samara. 2005. "Neurologic and Developmental Disability at Six Years of Age after Extremely Preterm Birth." *New England Journal of Medicine* 352 (1): 9–19. doi:10.1056/NEJMoa041367.

Metaxa-Mariatou, V., C. J. McGavigan, K. Robertson, C. Stewart, I. T. Cameron, and S. Campbell. 2002. "Elastin Distribution in the Myometrial and Vascular Smooth Muscle of the Human Uterus." *MHR: Basic Science of Reproductive Medicine* 8 (6): 559–65. doi:10.1093/molehr/8.6.559.

Mizrahi, J., Z. Karni, and W. Z. Polishuk. 1980. "Isotropy and Anisotropy of Uterine Muscle during Labor Contraction." *Journal of Biomechanics* 13 (3): 211–18. doi:10.1016/0021-9290(80)90364-4.

Mondragon, Eli, Ph D. Kristin Myers, and M. S. Kyoko Yoshida. 2017. "Characterizing the Biomechanical and Biochemical Properties of Mouse Uterine Tissue." *Columbia Undergraduate Science Journal* 7 (2013).

Moore, Keith L., Anne M. R. Agur, and Arthur Dalley. 2014. *Essential Clinical Anatomy*. 5th ed. Philadelphia: LWW.

Moster, Dag, Rolv Terje Lie, and Trond Markestad. 2008. "Long-Term Medical and Social Consequences of Preterm Birth." *New England Journal of Medicine* 359 (3): 262–73. doi:10.1056/NEJMoa0706475.

Myers, K. M., A. P. Paskaleva, M. House, and S. Socrate. 2008. "Mechanical and Biochemical Properties of Human Cervical Tissue." *Acta Biomaterialia* 4 (1): 104–16. doi:10.1016/j.actbio.2007.04.009.

Myers, Kristin M., Helen Feltovich, Edoardo Mazza, Joy Vink, Michael Bajka, Ronald J. Wapner, Timothy J. Hall, and Michael House. 2015. "The Mechanical Role of the Cervix in Pregnancy." *Journal of Biomechanics*, Reproductive Biomechanics, 48 (9): 1511–23. doi:10.1016/j.jbiomech.2015.02.065.

Omari, Eenas A., Tomy Varghese, Mark A. Kliewer, Josephine Harter, and Ellen M. Hartenbach. 2015. "Dynamic and Quasi-Static Mechanical Testing for Characterization of the Viscoelastic Properties of Human Uterine Tissue." *Journal of Biomechanics* 48 (10): 1730–36. doi:10.1016/j.jbiomech.2015.05.013.

Oxlund, Birgitte S., Gitte Ørtoft, Annemarie Brüel, Carl Christian Danielsen, Pinar Bor, Hans Oxlund, and Niels Uldbjerg. 2010. "Collagen Concentration and Biomechanical Properties of Samples from the Lower Uterine Cervix in Relation to Age and Parity in Non-Pregnant Women." *Reproductive Biology and Endocrinology* 8: 82. doi:10.1186/1477-7827-8-82.

Oxlund, Birgitte S., Gitte Ørtoft, Annemarie Brüel, Carl Christian Danielsen, Hans Oxlund, and Niels Uldbjerg. 2010. "Cervical Collagen and Biomechanical Strength in Non-Pregnant Women with a History of Cervical Insufficiency." *Reproductive Biology and Endocrinology* 8: 92. doi:10.1186/1477-7827-8-92.

Pearsall, G. W., and V. L. Roberts. 1978. "Passive Mechanical Properties of Uterine Muscle (Myometrium) Tested in Vitro." *Journal of Biomechanics* 11 (4): 167–71. doi:10.1016/0021-9290(78)90009-X.

Petersen, Lone K. 1991. "In Vitro Analysis of Muscular Contractile Ability and Passive Biomechanical Properties of Uterine Cervical Samples from Nonpregnant Women." *Obstetrics and Gynecology* 77 (5): 772–76.

Rechberger, Tomasz, and J. Frederick Woessner. 1993. "Collagenase, Its Inhibitors, and Decorin in the Lower Uterine Segment in Pregnant Women." *American Journal of Obstetrics and Gynecology* 168 (5): 1598–1603. doi:10.1016/S0002-9378(11)90804-7.

Riley, Simon C., Rosemary Leask, Tim Chard, Neville C. Wathen, Andrew A. Calder, and David C. Howe. 1999. "Secretion of Matrix Metalloproteinase-2, Matrix Metalloproteinase-9 and Tissue Inhibitor of Metalloproteinases into the Intrauterine Compartments during Early Pregnancy." *MHR: Basic Science of Reproductive Medicine* 5 (4): 376–81. doi:10.1093/molehr/5.4.376.

Rubod, Chrystèle, Malik Boukerrou, Mathias Brieu, Patrick Dubois, and Michel Cosson. 2007. "Biomechanical Properties of Vaginal Tissue. Part 1: New Experimental Protocol." *The Journal of Urology* 178 (1): 320–25. doi:10.1016/j.juro.2007.03.040.

Sacks, Michael S. 2000. "Biaxial Mechanical Evaluation of Planar Biological Materials." *Journal of Elasticity and the Physical Science of Solids* 61 (1–3): 199. doi:10.1023/A:1010917028671.

Schlembach, Dietmar, Lynette MacKay, Leili Shi, William L. Maner, Robert E. Garfield, and Holger Maul. 2009. "Cervical Ripening and Insufficiency: From Biochemical and Molecular Studies to in Vivo Clinical Examination." *European Journal of Obstetrics & Gynecology and Reproductive Biology*, Supplement: Reproductive Bioengineering 2008, 144, Supplement 1 (May): S70–76. doi:10.1016/j.ejogrb.2009.02.036.

Szczesny, Spencer E., John M. Peloquin, Daniel H. Cortes, Jennifer A. Kadlowec, Louis J. Soslowsky, and Dawn M. Elliott. 2012. "Biaxial Tensile Testing and Constitutive Modeling of Human Supraspinatus Tendon." *Journal of Biomechanical Engineering* 134 (2): 021004-021004-9. doi:10.1115/1.4005852.

Shynlova, Oksana, Anna Dorogin, Yunqing Li, and Stephen Lye. 2014. "Inhibition of Infection-Mediated Preterm Birth by Administration of Broad Spectrum Chemokine Inhibitor in Mice." *Journal of Cellular and Molecular Medicine* 18 (9): 1816–29. doi:10.1111/jcmm.12307.

Shynlova, Oksana, Ruth Kwong, and Stephen J. Lye. 2010. "Mechanical Stretch Regulates Hypertrophic Phenotype of the Myometrium during Pregnancy." *Reproduction* 139 (1): 247–53. doi:10.1530/REP-09-0260.

Shynlova, Oksana, Yu-Hui Lee, Khetsopon Srikhajon, and Stephen J Lye. 2013. "Physiologic Uterine Inflammation and Labor Onset: Integration of Endocrine and Mechanical Signals." *Reproductive Sciences* 20 (2): 154–67. doi:10.1177/1933719112446084.

Shynlova, Oksana, Jennifer A. Mitchell, Anne Tsampalieros, B. Lowell Langille, and Stephen J. Lye. 2004. "Progesterone and Gravidity Differentially Regulate Expression of Extracellular Matrix Components in the Pregnant Rat Myometrium." *Biology of Reproduction* 70 (4): 986–92. doi:10.1095/biolreprod.103.023648.

Shynlova, Oksana, Prudence Tsui, Anna Dorogin, and Stephen J. Lye. 2008. "Monocyte Chemoattractant Protein-1 (CCL-2) Integrates Mechanical and Endocrine Signals That Mediate Term and Preterm Labor." *The Journal of Immunology* 181 (2): 1470–79. doi:10.4049/jimmunol.181.2.1470.

Shynlova, Oksana, Prudence Tsui, Shabana Jaffer, and Stephen J. Lye. 2009. "Integration of Endocrine and Mechanical Signals in the Regulation of Myometrial Functions during Pregnancy and Labour." *European Journal of Obstetrics, Gynecology, and Reproductive Biology* 144 Suppl 1 (May): S2-10. doi:10.1016/j.ejogrb.2009.02.044.

Silver, Frederick H. 2006. *Mechanosensing and Mechanochemical Transduction in Extracellular Matrix*. New York, NY: Springer US. doi:10.1007/978-0-387-28176-6.

Sun, Wei, Michael S. Sacks, Tiffany L. Sellaro, William S. Slaughter, and Michael J. Scott. 2003. "Biaxial Mechanical Response of Bioprosthetic Heart Valve Biomaterials to High In-Plane Shear." *Journal of Biomechanical Engineering* 125 (3): 372–80. doi:10.1115/1.1572518.

Timmons, Brenda, Meredith Akins, and Mala Mahendroo. 2010. "Cervical Remodeling during Pregnancy and Parturition." *Trends in Endocrinology and Metabolism: TEM* 21 (6): 353–61. doi:10.1016/j.tem.2010.01.011.

Vande Geest, Jonathan P., Michael S. Sacks, and David A. Vorp. 2006. "The Effects of Aneurysm on the Biaxial Mechanical Behavior of Human Abdominal Aorta." *Journal of Biomechanics* 39 (7): 1324–34. doi:10.1016/j.jbiomech.2005.03.003.

Weiss, Stephan, Thomas Jaermann, Peter Schmid, Philipp Staempfli, Peter Boesiger, Peter Niederer, Rosmarie Caduff, and Michael Bajka. 2006. "Three-Dimensional Fiber Architecture of the Nonpregnant Human Uterus Determined Ex Vivo Using Magnetic Resonance Diffusion Tensor Imaging." *The Anatomical Record. Part A, Discoveries in Molecular, Cellular, and Evolutionary Biology* 288 (1): 84–90. doi:10.1002/ar.a.20274.

Willms, A. B., E. D. Brown, U. I. Kettritz, J. A. Kuller, and R. C. Semelka. 1995. "Anatomic Changes in the Pelvis after Uncomplicated Vaginal Delivery: Evaluation with Serial MR Imaging." *Radiology* 195 (1): 91–94. doi:10.1148/radiology.195.1.7892501.

Word, R. Ann, Xiang-Hong Li, Michael Hnat, and Kelley Carrick. 2007. "Dynamics of Cervical Remodeling during Pregnancy and Parturition: Mechanisms and Current Concepts." *Seminars in Reproductive Medicine* 25 (01): 069–079. doi:10.1055/s-2006-956777.

Wray, S. 1982. "The Role of Mechanical and Hormonal Stimuli on Uterine Involution in the Rat." *The Journal of Physiology* 328 (1): 1–9. doi:10.1113/jphysiol.1982.sp014249.

Yao, Wang, Yu Gan, Kristin M. Myers, Joy Y. Vink, Ronald J. Wapner, and Christine P. Hendon. 2016. "Collagen Fiber Orientation and Dispersion in the Upper Cervix of Non-Pregnant and Pregnant Women." *PLOS ONE* 11 (11): e0166709. doi:10.1371/journal.pone.0166709.

Yao, Wang, Kyoko Yoshida, Michael Fernandez, Joy Vink, Ronald J. Wapner, Cande V. Ananth, Michelle L. Oyen, and Kristin M. Myers. 2014. "Measuring the Compressive Viscoelastic Mechanical Properties of Human Cervical Tissue Using Indentation." *Journal of the Mechanical Behavior of Biomedical Materials* 34 (June): 18–26. doi:10.1016/j.jmbbm.2014.01.016.

Yoshida, Kyoko, Hongfeng Jiang, MiJung Kim, Joy Vink, Serge Cremers, David Paik, Ronald Wapner, Mala Mahendroo, and Kristin Myers. 2014. "Quantitative Evaluation of Collagen Crosslinks and Corresponding Tensile Mechanical Properties in Mouse Cervical Tissue during Normal Pregnancy." *PLoS ONE* 9 (11). doi:10.1371/journal.pone.0112391.

Yoshida, Kyoko, Claire Reeves, Joy Vink, Jan Kitajewski, Ronald Wapner, Hongfeng Jiang, Serge Cremers, and Kristin Myers. 2014. "Cervical Collagen Network Remodeling in Normal Pregnancy and Disrupted Parturition in Antxr2 Deficient Mice." *Journal of Biomechanical Engineering* 136 (2): 021017-021017-8. doi:10.1115/1.4026423.

Chapter 4.2

Abramowitch, Steven D., Andrew Feola, Zegbeh Jallah, and Pamela A. Moalli. 2009. "Tissue Mechanics, Animal Models, and Pelvic Organ Prolapse: A Review." *European Journal of Obstetrics & Gynecology and Reproductive Biology*, Supplement: Reproductive Bioengineering 2008, 144, Supplement 1 (May): S146–58. doi:10.1016/j.ejogrb.2009.02.022.

Alarab, May, Maria AT Bortolini, Harold Drutz, Stephen Lye, and Oksana Shynlova. 2010. "LOX Family Enzymes Expression in Vaginal Tissue of Premenopausal Women with Severe Pelvic Organ Prolapse." *International Urogynecology Journal* 21 (11): 1397–1404. doi:10.1007/s00192-010-1199-9.

Ashton-Miller, James A., Denise Howard, and John O. L. DeLancey. 2001. "The Functional Anatomy of the Female Pelvic Floor and Stress Continence Control System." *Scandinavian Journal of Urology and Nephrology. Supplementum*, no. 207: 1–125.

Baah-Dwomoh, Adwoa, Jeffrey McGuire, Ting Tan, and Raffaella De Vita. 2016. "Mechanical Properties of Female Reproductive Organs and Supporting Connective Tissues: A Review of the Current State of Knowledge." *Applied Mechanics Reviews* 68 (6): 060801-060801-12. doi:10.1115/1.4034442.

Badiou, Wassim, Guillaume Granier, Philippe-Jean Bousquet, Xavier Monrozies, Pierre Mares, and Renaud de Tayrac. 2008. "Comparative Histological Analysis of Anterior Vaginal Wall in Women with Pelvic Organ Prolapse or Control Subjects. A Pilot Study." *International Urogynecology Journal* 19 (5): 723–29. doi:10.1007/s00192-007-0516-4.

Barone, William R., Andrew J. Feola, Pamela A. Moalli, and Steven D. Abramowitch. 2012. "The Effect of Pregnancy and Postpartum Recovery on the Viscoelastic Behavior of the Rat Cervix." *Journal of Mechanics in Medicine & Biology* 12 (1): 1250009–1.

Becker, Winston R., and Raffaella De Vita. 2015. "Biaxial Mechanical Properties of Swine Uterosacral and Cardinal Ligaments." *Biomechanics and Modeling in Mechanobiology* 14 (3): 549–60. doi:10.1007/s10237-014-0621-5.

Bersi, M. R., M. J. Collins, E. Wilson, and J. D. Humphrey. 2012. "Disparate Changes in the Mechanical Properties of Murine Carotid Arteries and Aorta in Response to Chronic Infusion of Angiotensin-II." *International Journal of Advances in Engineering Sciences and Applied Mathematics* 4 (4): 228–40. doi:10.1007/s12572-012-0052-4.

Bortolini, Maria A. T., Oksana Shynlova, Harold P. Drutz, Manoel J. B. C. Girão, Rodrigo A. Castro, Stephen Lye, and May Alarab. 2011. "Expression of Bone Morphogenetic Protein-1 in Vaginal Tissue of Women with Severe Pelvic Organ Prolapse." *American Journal of Obstetrics and Gynecology* 204 (6): 544.e1-544.e8. doi:10.1016/j.ajog.2011.01.021.

Budatha, Madhusudhan, Shayzreen Roshanravan, Qian Zheng, Cecilia Weislander, Shelby L. Chapman, Elaine C. Davis, Barry Starcher, R. Ann Word, and Hiromi Yanagisawa. 2011. "Extracellular Matrix Proteases Contribute to Progression of Pelvic Organ Prolapse in Mice and Humans." *The Journal of Clinical Investigation* 121 (5): 2048–59. doi:10.1172/JCI45636.

Buller, Jerome L, Jason R Thompson, Geoffrey W Cundiff, Lianne Krueger Sullivan, Miguel A Schön Ybarra, and Alfred E Bent. 2001. "Uterosacral Ligament: Description of Anatomic Relationships to Optimize Surgical Safety." *Obstetrics & Gynecology* 97 (6): 873–79. doi:10.1016/S0029-7844(01)01346-1.

Bump, Richard C., Anders Mattiasson, Kari Bø, Linda P. Brubaker, John O. L. DeLancey, Peter Klarskov, Bob L. Shull, and Anthony R. B. Smith. 1996. "The Standardization of Terminology of Female Pelvic Organ Prolapse and Pelvic Floor Dysfunction." *American Journal of Obstetrics and Gynecology* 175 (1): 10–17. doi:10.1016/S0002-9378(96)70243-0.

Carley, M. E., and J. Schaffer. 2000. "Urinary Incontinence and Pelvic Organ Prolapse in Women with Marfan or Ehlers Danlos Syndrome." *American Journal of Obstetrics and Gynecology* 182 (5): 1021–23.

Chen, Bertha, Yan Wen, and Mary Lake Polan. 2004. "Elastolytic Activity in Women with Stress Urinary Incontinence and Pelvic Organ Prolapse." *Neurourology and Urodynamics* 23 (2): 119–26. doi:10.1002/nau.20012.

Chiaffarino, F, L Chatenoud, M Dindelli, M Meschia, A Buonaguidi, F Amicarelli, M Surace, E Bertola, E Di Cintio, and F. Parazzini. 1999. "Reproductive Factors, Family History, Occupation and Risk of Urogenital Prolapse." *European Journal of Obstetrics & Gynecology and Reproductive Biology* 82 (1): 63–67. doi:10.1016/S0301-2115(98)00175-4.

Collinet, Pierre, Franck Belot, Philippe Debodinance, Edouard Ha Duc, Jean-Philippe Lucot, and Michel Cosson. 2006. "Transvaginal Mesh Technique for Pelvic Organ Prolapse Repair: Mesh Exposure Management and Risk Factors." *International Urogynecology Journal* 17 (4): 315–20. doi:10.1007/s00192-005-0003-8.

Downing, Keith T., Mubashir Billah, Eva Raparia, Anup Shah, Moshe C. Silverstein, Amanda Ahmad, and Gregory S. Boutis. 2014a. "The Role of Mode of Delivery on Elastic Fiber Architecture and Vaginal Vault Elasticity: A Rodent Model Study." *Journal of the Mechanical Behavior of Biomedical Materials* 29 (January): 190–98. doi:10.1016/j.jmbbm.2013.08.025.

Drewes, Peter G., Hiromi Yanagisawa, Barry Starcher, Ian Hornstra, Katalin Csiszar, Spyridon I. Marinis, Patrick Keller, and R. Ann Word. 2007. "Pelvic Organ Prolapse in Fibulin-5 Knockout Mice: Pregnancy-Induced Changes in Elastic Fiber Homeostasis in Mouse Vagina." *The American Journal of Pathology* 170 (2): 578–89. doi:10.2353/ajpath.2007.060662.

Epstein, Lee B., Carol A. Graham, and Michael H. Heit. 2007. "Systemic and Vaginal Biomechanical Properties of Women with Normal Vaginal Support and Pelvic Organ Prolapse." *American Journal of Obstetrics and Gynecology* 197 (2): 165.e1-6. doi:10.1016/j.ajog.2007.03.040.

Ewies, Ayman A. A., Farook Al- Azzawi, and John Thompson. 2003. "Changes in Extracellular Matrix Proteins in the Cardinal Ligaments of Post- menopausal Women with or without Prolapse: A Computerized Immunohistomorphometric Analysis." *Human Reproduction* 18 (10): 2189–95. doi:10.1093/humrep/deg420.

Feola, Andrew, Masayuki Endo, and Jan Deprest. 2014. "Biomechanics of the Rat Vagina during Pregnancy and Postpartum: A 3-Dimensional Ultrasound Approach." *International Urogynecology Journal* 25 (7): 915–20. doi:10.1007/s00192-013-2313-6.

Feola, Andrew, Pamela Moalli, Marianna Alperin, Robbie Duerr, Robin E. Gandley, and Steven Abramowitch. 2011. "Impact of Pregnancy and Vaginal Delivery on the Passive and Active Mechanics of the Rat Vagina." *Annals of Biomedical Engineering* 39 (1): 549–58. doi:10.1007/s10439-010-0153-9.

Gabriel, Boris, Dominik Denschlag, Heike Göbel, Cordula Fittkow, Martin Werner, Gerald Gitsch, and Dirk Watermann. 2005. "Uterosacral Ligament in Postmenopausal Women with or without Pelvic Organ Prolapse." *International Urogynecology Journal* 16 (6): 475–79. doi:10.1007/s00192-005-1294-5.

Giri, Ayush, Katherine E. Hartmann, Jacklyn N. Hellwege, Digna R. Velez Edwards, and Todd L. Edwards. 2017. "Obesity and Pelvic Organ Prolapse: A Systematic Review and Meta-Analysis of Observational Studies." *American Journal of Obstetrics and Gynecology*. Accessed March 12. doi:10.1016/j.ajog.2017.01.039.

Goh, Judith T. W. 2003. "Biomechanical and Biochemical Assessments for Pelvic Organ Prolapse." *Current Opinion in Obstetrics & Gynecology* 15 (5): 391–94. doi:10.1097/01.gco.0000094700.87578.a9.

Gruber, Daniel D., William B. Warner, Eric D. Lombardini, Christopher M. Zahn, and Jerome L. Buller. 2011. "Anatomical and Histological Examination of the Porcine Vagina and Supportive Structures: In Search of an Ideal Model for Pelvic Floor Disorder Evaluation and Management." *Female Pelvic Medicine & Reconstructive Surgery* 17 (3): 110–14. doi:10.1097/SPV.0b013e318214b1a6.

Hendrix, Susan L., Amanda Clark, Ingrid Nygaard, Aaron Aragaki, Vanessa Barnabei, and Anne McTiernan. 2002. "Pelvic Organ Prolapse in the Women's Health Initiative: Gravity and Gravidity." *American Journal of Obstetrics and Gynecology* 186 (6): 1160–66. doi:10.1067/mob.2002.123819.

Jackson, S. R., N. C. Avery, J. F. Tarlton, S. D. Eckford, P. Abrams, and A. J. Bailey. 1996. "Changes in Metabolism of Collagen in Genitourinary Prolapse." *Lancet (London, England)* 347 (9016): 1658–61.

Karam, Jose A., Dolores V. Vazquez, Victor K. Lin, and Philippe E. Zimmern. 2007. "Elastin Expression and Elastic Fibre Width in the Anterior Vaginal Wall of Postmenopausal Women with and without Prolapse." *BJU International* 100 (2): 346–50. doi:10.1111/j.1464-410X.2007.06998.x.

Kim, Eun Jae, Namhyun Chung, Sung Hyo Park, Kyoung-Hee Lee, Suhng Wook Kim, Ji Young Kim, Sang Wook Bai, and Myung Jae Jeon. 2013. "Involvement of Oxidative Stress and Mitochondrial Apoptosis in the Pathogenesis of Pelvic Organ Prolapse." *The Journal of Urology* 189 (2): 588–94. doi:10.1016/j.juro.2012.09.041.

Knight, Katrina M., Pamela A. Moalli, Alexis Nolfi, Stacy Palcsey, William R. Barone, and Steven D. Abramowitch. 2016. "Impact of Parity on Ewe Vaginal Mechanical Properties Relative to the Nonhuman Primate and Rodent." *International Urogynecology Journal* 27 (8): 1255–63. doi:10.1007/s00192-016-2963-2.

Ko, C. Y., D. Lim, B. S. Namgung, H. D. Kim, H. S. Kim, D. G. Woo, and H. S. Kim. 2007. "MORPHOLOGICAL AND MECHANICAL CHARACTERISTICS DURING PREGNANCY AND LACTATION." *Journal of Biomechanics*, Program and Abstracts of the XXI Congress, International Society of Biomechanics, 40, Supplement 2: S368. doi:10.1016/S0021-9290(07)70363-9.

Lammers, Karin, Sabrina L. Lince, Marian A. Spath, Léon C. L. T. van Kempen, Jan C. M. Hendriks, Mark E. Vierhout, and Kirsten B. Kluivers. 2012. "Pelvic Organ Prolapse and Collagen-Associated Disorders." *International Urogynecology Journal* 23 (3): 313–19. doi:10.1007/s00192-011-1532-y.

Lang, J.h., L. Zhu, Z.j. Sun, and J. Chen. 2003. "Estrogen Levels and Estrogen Receptors in Patients with Stress Urinary Incontinence and Pelvic Organ Prolapse." *International Journal of Gynecology & Obstetrics* 80 (1): 35–39. doi:10.1016/S0020-7292(02)00232-1.

Laso-García, Inés M., Miguel A. Rodríguez-Cabello, Miguel A. Jiménez-Cidre, Andrea Orosa-Andrada, David Carracedo-Calvo, Luis López-Fando, and Francisco J. Burgos-Revilla. 2017. "Prospective Long-Term Results, Complications and Risk Factors in Pelvic Organ Prolapse Treatment with Vaginal Mesh." *European Journal of Obstetrics and Gynecology and Reproductive Biology* 211 (April): 62–67. doi:10.1016/j.ejogrb.2017.02.005.

Lei, Lingling, Yanfeng Song, and RiQi Chen. 2007. "Biomechanical Properties of Prolapsed Vaginal Tissue in Pre- and Postmenopausal Women." *International Urogynecology Journal* 18 (6): 603–7. doi:10.1007/s00192-006-0214-7.

Lin, Sheng-Yen, Yi-Torng Tee, Soo-Cheen Ng, Han Chang, PinPin Lin, and Gin-Den Chen. 2007. "Changes in the Extracellular Matrix in the Anterior Vagina of Women with or without Prolapse." *International Urogynecology Journal* 18 (1): 43–48. doi:10.1007/s00192-006-0090-1.

Mant, Jonathan, Rosemary Painter, and Martin Vessey. 1997. "Epidemiology of Genital Prolapse: Observations from the Oxford Family Planning Association Study." *BJOG: An International Journal of Obstetrics & Gynaecology* 104 (5): 579–85. doi:10.1111/j.1471-0528.1997.tb11536.x.

Margulies, Rebecca U., Christina Lewicky-Gaupp, Dee E. Fenner, Edward J. McGuire, J. Quentin Clemens, and John O. L. DeLancey. 2008. "Complications Requiring Reoperation Following Vaginal Mesh Kit Procedures for Prolapse." *American Journal of Obstetrics & Gynecology* 199 (6): 678.e1-678.e4. doi:10.1016/j.ajog.2008.07.049.

Martins, P., E. Peña, B. Calvo, M. Doblaré, T. Mascarenhas, R. Natal Jorge, and A. Ferreira. 2010. "Prediction of Nonlinear Elastic Behaviour of Vaginal Tissue: Experimental Results and Model Formulation." *Computer Methods in Biomechanics and Biomedical Engineering* 13 (3): 327–37. doi:10.1080/10255840903208197.

Miller, Kristin S., Brianne K. Connizzo, Elizabeth Feeney, and Louis J. Soslowsky. 2012. "Characterizing Local Collagen Fiber Re-Alignment and Crimp Behavior throughout Mechanical Testing in a Mature Mouse Supraspinatus Tendon Model." *Journal of Biomechanics* 45 (12): 2061–65. doi:10.1016/j.jbiomech.2012.06.006.

Moalli, Pamela A., Stuart H. Shand, Halina M. Zyczynski, Susan C. Gordy, and Leslie A. Meyn. 2005. "Remodeling of Vaginal Connective Tissue in Patients With Prolapse:" *Obstetrics & Gynecology* 106 (5, Part 1): 953–63. doi:10.1097/01.AOG.0000182584.15087.dd.

Moore, Keith L., Anne M. R. Agur, and Arthur Dalley. 2014. *Essential Clinical Anatomy*. 5th ed. Philadelphia: LWW.

Morris, V., Conway, C., and Miller, K., 2016, "Determining the Effect of Elastin Digestion on the Regional Biaxial Mechanical Properties of the Murine Cervix." Summer Biomechanics, Bioengineering, and Biotransport Conference (SB3C2016).

Nygaard, Ingrid, Catherine Bradley, and Debra Brandt. 2004. "Pelvic Organ Prolapse in Older Women: Prevalence and Risk Factors:" *Obstetrics & Gynecology* 104 (3): 489–97. doi:10.1097/01.AOG.0000136100.10818.d8.

Olsen, A. L., V. J. Smith, J. O. Bergstrom, J. C. Colling, and A. L. Clark. 1997. "Epidemiology of Surgically Managed Pelvic Organ Prolapse and Urinary Incontinence." *Obstetrics and Gynecology* 89 (4): 501–6. doi:10.1016/S0029-7844(97)00058-6.

Petros, Peter. 2007. *The Female Pelvic Floor*. 2nd ed. Berlin, Heidelberg: Springer Berlin Heidelberg. doi:10.1007/978-3-540-33664-8.

Rahn, David D., Matthew D. Ruff, Spencer A. Brown, Harry F. Tibbals, and R. Ann Word. 2008. "Biomechanical Properties of the Vaginal Wall: Effect of Pregnancy, Elastic Fiber Deficiency, and Pelvic Organ Prolapse." *American Journal of Obstetrics and Gynecology* 198 (5): 590.e1-590.e6. doi:10.1016/j.ajog.2008.02.022.

Robison, K., Bivona, D., and Miller, K., 2016, "Effect of Elastin Digestion on the Biaxial Mechanical Response of the Murine Vagina." Summer Biomechanics, Bioengineering and Biotransport Conference (SB3C2016).

Rubod, Chrystèle, Malik Boukerrou, Mathias Brieu, Patrick Dubois, and Michel Cosson. 2007. "Biomechanical Properties of Vaginal Tissue. Part 1: New Experimental Protocol." *The Journal of Urology* 178 (1): 320–25. doi:10.1016/j.juro.2007.03.040.

Ruiz-Zapata, Alejandra M., Manon H. Kerkhof, Samaneh Ghazanfari, Behrouz Zandieh-Doulabi, Reinout Stoop, Theo H. Smit, and Marco N. Helder. 2016. "Vaginal Fibroblastic Cells from Women with Pelvic Organ Prolapse Produce Matrices with Increased Stiffness and Collagen Content." *Scientific Reports* 6 (March): 22971. doi:10.1038/srep22971.

Salman, Mehmet Coskun, Ozgur Ozyuncu, Mustafa Fevzi Sargon, Turkan Kucukali, and Tekin Durukan. 2010. "Light and Electron Microscopic Evaluation of Cardinal Ligaments in Women with or without Uterine Prolapse." *International Urogynecology Journal* 21 (2): 235–39. doi:10.1007/s00192-009-1006-7.

Strauss, Carolin, Andreas Lienemann, Fritz Spelsberg, Maret Bauer, Walter Jonat, and Alexander Strauss. 2012. "Biomechanics of the Female Pelvic Floor: A Prospective Trail of the Alteration of Force–displacement-Vectors in Parous and Nulliparous Women." *Archives of Gynecology and Obstetrics* 285 (3): 741–47. doi:10.1007/s00404-011-2024-5.

Tan, Ting, Frances M. Davis, Daniel D. Gruber, Jason C. Massengill, John L. Robertson, and Raffaella De Vita. 2015. "Histo-Mechanical Properties of the Swine Cardinal and Uterosacral Ligaments." *Journal of the Mechanical Behavior of Biomedical Materials* 42 (February): 129–37. doi:10.1016/j.jmbbm.2014.11.018.

Udelsman, Brooks V., Ramak Khosravi, Kristin S. Miller, Ethan W. Dean, Matthew R. Bersi, Kevin Rocco, Tai Yi, Jay D. Humphrey, and Christopher K. Breuer. 2014. "Characterization of Evolving Biomechanical Properties of Tissue Engineered Vascular Grafts in the Arterial Circulation." *Journal of Biomechanics* 47 (9): 2070–79. doi:10.1016/j.jbiomech.2014.03.011.

Vande Geest, Jonathan P., Michael S. Sacks, and David A. Vorp. 2006. "The Effects of Aneurysm on the Biaxial Mechanical Behavior of Human Abdominal Aorta." *Journal of Biomechanics* 39 (7): 1324–34. doi:10.1016/j.jbiomech.2005.03.003.

Weber, Anne M., and Holly E. Richter. 2005. "Pelvic Organ Prolapse:" *Obstetrics & Gynecology* 106 (3): 615–34. doi:10.1097/01.AOG.0000175832.13266.bb.

Word, R. Ann, Sujatha Pathi, and Joseph I. Schaffer. 2009. "Pathophysiology of Pelvic Organ Prolapse." *Obstetrics and Gynecology Clinics of North America*, Female Pelvic Medicine and Reconstructive Surgery, 36 (3): 521–39. doi:10.1016/j.ogc.2009.09.001.

Zhou, Lu, Jung Han Lee, Yan Wen, Christos Constantinou, Murayama Yoshinobu, Sadao Omata, and Bertha Chen. 2012. "Biomechanical Properties and Associated Collagen Composition in Vaginal Tissue of Women with Pelvic Organ Prolapse." *The Journal of Urology* 188 (3): 875–80. doi:10.1016/j.juro.2012.05.017.

Zong, Wenjun, Suzan E. Stein, Barry Starcher, Leslie A. Meyn, and Pamela A. Moalli. 2010. "Alteration of Vaginal Elastin Metabolism in Women With Pelvic Organ Prolapse:" *Obstetrics & Gynecology* 115 (5): 953–61. doi:10.1097/AOG.0b013e3181da7946.

BIOGRAPHY

Jonathan Nguyen is from New Orleans, Louisiana, and enrolled in 2012 at Tulane University to study biomedical engineering. He attended as an undergraduate and graduate student pursuing the 5th year's Master's program. His work at Tulane has focused on the design and construction of a planar biaxial device for Dr. Kristin Miller's growth and remodeling lab. His research interests include the mechanical pathogenesis of preterm birth and pelvic organ prolapse.